

THE PH.D. THESIS ENTITLED

---

FUNDAMENTAL PROPERTIES OF SPATIALLY  
OSCILLATING LIQUID JETS: *A Numerical  
Approach*

---

SUBMITTED IN PARTIAL FULFILMENT OF REQUIREMENTS FOR THE DEGREE OF

*DOCTOR OF PHILOSOPHY*  
IN MECHANICAL ENGINEERING

BY

ASHISH S. AROTE  
REG. NO. D17ME002

AND

SUPERVISED BY

DR. J. BANERJEE  
PROFESSOR

DR. M. H. BADE  
ASSISTANT PROFESSOR

AT THE



Department of Mechanical Engineering  
Sardar Vallabhbhai National Institute of Technology  
Surat-395007, Gujarat, India

JUNE 2021



---

*Once more into the fray...  
Into the last good fight I'll ever know.  
Live and die on this day...  
Live and die on this day...*

— *The Grey*



*To my parents, wife Smita, son Saish, and,  
Shaswat Saincher and Ila Shastri*



# Acknowledgement

This thesis represents the journey from learning to print “*Hello World!*” on screen to iteratively solving the complex non-linear fluid flow equations. This thesis also represents my work done and time spent at *S V NIT, Surat* and especially in AFD lab. Every second of my life spent here working on my skills has been delightful and amazing. It is a great feeling when you are getting paid for doing the work that you love and more importantly it is that work which makes you happy. The present work is a result of efforts put in by many people to support my endeavours and goals.

Firstly, I would like thank my thesis supervisors, **Dr. Banerjee** and **Dr. Bade** for providing me with the freedom to implement my ideas. This freedom has allowed me to be creative and take risks (which fortunately paid off). I am grateful for the discussions that I had with both of them on both technical and non-technical aspects of academia. I would also like to thank my thesis committee involving **Dr. H. B. Mehta**, **Dr. A. K. Jana** and **Dr. V. L. Manekar** for providing the encouragement and suggestions during the crucial time of my research.

I would like to thank my colleagues **Mr. Sunny Saini**, **Mr. Nishant Shah**, **Mr. Chetan Anghan**, **Mr. Krishna Kumar** and **Mr. Sanjay Patel** for providing great camaraderie in the lab. I would also like to thank my past colleagues **Mr. Rujal Patel** and **Mr. Kathan Khalasi** for working with me and having interesting discussions on the CFD solvers. I would also like to thank **Mr. Bhaskar Chakraborty** for sharing his views and technical details on the flow solvers and algebraic multiphase flow algorithms.

I would like to thank my friend, mentor and inspiration (also my senior!) **Dr. Shaswat Saincher** for taking out time from his work and teaching me the basics of coding, CFD and academic pathways. We had intense discussions on various aspects (even on ghosts and their lifecycle!) of life that have made me a better person. He has constantly helped and supported my family in difficult times. I cannot forget the chocolates, coffee and hot-dogs that you prepared and most importantly the time spent on the classic wooden table in your room. I would also like to thank **Dr. Ila Shastri** for everything she did for my family. I have never met a better human being than her. I am thankful for the great food you made for us (you are a great cook!), the advice you gave and most importantly for caring about us.

I would like to thank my wife **Smita** for supporting me during the ups and downs of my life. I would also like to thank her for listening my inanity and frustrations when I had a bad day in the office. I also thank her for sacrificing her career for my ambitions and helping me out during crucial decisions. I want to thank my son **Saish** for bringing peace and happiness in my life.

I would also like to thank my in-laws **Amit**, **Jyoti**, **Aai**, **Anna** and **Shivansh** for providing an excellent support system that allowed me to carry out my work smoothly.

*Ashish Arote*



## Abstract

Understanding a liquid jet and the influence of surrounding fluid on it has been a classical problem in fluid mechanics. An oscillating jet is a spatially perturbed jet that is practically produced using a *fluidic oscillator*. The efficacy of oscillating jets in industrial applications involving mixing and dispersion is well established, yet, the fundamental aspects such as its instability, coherent structures in the flow and its behaviour when used in tandem is still obscure. This understanding is significant for the effectual development of control strategies for oscillating jets in view of their diverse industrial applications. Therefore, the present study is directed towards analysing the flow fields with the purpose of resolving the underlying flow physics of oscillating jets. The numerical results reported here are obtained by solving *Navier-Stokes* equations coupled with the *Volume of Fluid* (VOF) equation to track the gas-liquid interface.

An improved algebraic VOF method named *Smoothly Adapting Interfacial scheme based on Hybridization* (SAISH) is introduced in the present work. This scheme demonstrates lower mass loss and provides accurate results by being computationally efficient as compared to other compressive VOF schemes. Moreover, the accuracy of the method is retained at complex flow fields and stringent *Courant* number conditions.

Initially, cause for the occurrence of instability in the oscillating jet is investigated. It is demonstrated that the vortical structures aligned with the jet peaks provide the pressure difference causing instability in oscillating jets. Moreover, the effect of flow properties such as surface tension, viscosity, gravity and inlet velocity profiles on jet stability is analysed. It is reported that properties such as surface tension and viscosity dampen the oscillations whereas, a flat inlet velocity profile augments the oscillation amplitude. On the other hand, oscillating jet breakup mechanisms are also explored, which demonstrate that, apart from *Kelvin-Helmholtz* (KH) and *Rayleigh-Taylor* (RT) instabilities, capillary (*Rayleigh-Plateau*) instability also contributes to the jet breakup. Furthermore, the formation and evolution of the vortical structures around the jet are investigated to understand the entrainment characteristics. The coherent structures in the flow for *Reynolds numbers* (Re) 4500 and 500 are identified using *Q-criterion*. It is demonstrated that for oscillating jets, the spreading and entrainment increases with an increase in Re. These jet characteristics are greatly influenced by the head vortices, which transform into pair of hairpin vortices which further undergo leapfrogging. These jet front dynamics is found to be damped when viscous forces are dominant. The numerical results also suggest the existence of sideways hairpin vortices that expel the fluid by forming a channel and are significantly subdued at low Re. A peculiar merging of span-wise *Kelvin-Helmholtz* (KH) rollers at low Re is also reported in the present study. Furthermore, the dominant flow structures are identified and analysed using *proper orthogonal decomposition* (POD) and *dynamic mode decomposition* (DMD). The results demonstrate the dominance of coherent structures at the downstream for higher Re, with vortices in the near field at the jet peaks also contributing to the flow field dynamics. In addition, the synchronous and asynchronous oscillating jets in tandem are also analysed to understand their development, instability and interaction between the coherent structures. Moreover, an effect of nozzle spacing on the behaviour of these oscillating jets in tandem configuration is also reported here. It is demonstrated that the near-field dynamics of these jets is not affected by the nozzle spacing whereas, at the downstream, the merging region is significantly influenced by the nozzle spacing. Furthermore, reducing the nozzle spacing leads to destabilization of these jets, which increase the oscillation amplitude and entrainment of surrounding fluid downstream.



# Contents

## Acknowledgement

## Abstract

<b>List of Figures</b>	i
------------------------	---

<b>List of Tables</b>	vii
-----------------------	-----

<b>1 Introduction</b>	1
1.1 Stability of Planar Liquid Jets . . . . .	2
1.2 Coherent Structures in Planar Liquid Jets . . . . .	3
1.3 Planar Liquid Jets in Tandem . . . . .	4
1.4 Motivation and Objectives . . . . .	5
1.5 Overview . . . . .	6
<b>2 Numerical Methodology</b>	7
2.1 Governing Equations . . . . .	7
2.2 Volume of Fluid Method . . . . .	8
2.2.1 Geometric VOF Method . . . . .	8
2.2.2 Algebraic VOF Method . . . . .	15
2.3 Surface Tension Modelling . . . . .	26
2.4 Solution Methodology . . . . .	30
2.5 Discretization of Spatial and Temporal Terms . . . . .	33
<b>3 Stability of an Oscillating Jet</b>	37
3.1 Development of an Oscillating Liquid Jet . . . . .	42
3.2 Effect of Reynolds Number . . . . .	47
3.3 Effect of Weber number . . . . .	48
3.4 Effect of Froude number . . . . .	50
3.5 Effect of Inlet-Velocity Profile . . . . .	51
3.6 Closure . . . . .	52
<b>4 Coherent Structures in an Oscillating Jet</b>	55
4.1 Head Vortex Structures . . . . .	59
4.2 Span-wise Vortex Structures . . . . .	64
4.3 Stream-wise Vortex Structures . . . . .	66
4.4 Proper Orthogonal Decomposition (POD) . . . . .	69
4.5 Dynamic Mode Decomposition (DMD) . . . . .	73
4.6 Closure . . . . .	77

<b>5 Oscillating Liquid Jets in Tandem</b>	<b>79</b>
5.1 Synchronous Tandem Jets . . . . .	81
5.1.1 Development of Synchronous Jets . . . . .	81
5.1.2 Stability of Synchronous Jets . . . . .	82
5.1.3 Interaction of Coherent Structures in Synchronous Jets . . . . .	84
5.2 Asynchronous Tandem Jets . . . . .	87
5.2.1 Development of Asynchronous Jets . . . . .	87
5.2.2 Stability of Asynchronous Jets . . . . .	88
5.2.3 Interaction of Coherent Structures in Asynchronous Jets . . . . .	91
5.3 Closure . . . . .	93
<b>6 Contributions and Recommendations</b>	<b>95</b>
6.1 Contribution to the Existing Literature . . . . .	95
6.2 Recommendations . . . . .	96
<b>Associated Publications</b>	<b>97</b>
<b>Appendices</b>	<b>99</b>
<b>A Algorithm for Estimating Dominant Coherent Modes</b>	<b>99</b>
<b>B Phase Averaging of Velocity Field</b>	<b>101</b>
<b>Bibliography</b>	

# List of Figures

1.1	Working principle of fluidic oscillator <sup>1</sup>	1
2.1	9-cell stencil for interface normals.	9
2.2	Reconstruction (PLIC) test for the uniform and non-uniform grid of $30 \times 30$ resolution in a square domain of size 2.	11
2.3	Sample calculation of east face flux for Case I.	12
2.4	Advection test results are presented for unit square domain with grid of $128^2$ and the having time stepping of $\Delta t=0.0078125$ for single vortex and deformation test while $\Delta t = 0.00625$ and $\Delta t = 0.0025$ for superman flow and droplet flow, respectively.	13
2.5	Dam break problem setup	14
2.6	Dam break results for non-dimensional time 0, 1, 2, 3 and 4	14
2.7	Fluid front positions with time compared with <sup>76</sup> Raessi and Pitsch	14
2.8	The results for RT instability are presented at non-dimensional time of 2, 4, 6 and 8.	15
2.9	Cell nomenclature based on the flow direction.	15
2.10	NVD for SAISH demonstrating HR and BD regions.	18
2.11	Iso-surfaces for 0.5 volume fraction for the single vortex test using a) <i>CUIBS</i> and b) <i>FBICS</i> c) <i>M-CICSAM</i> and d) <i>SAISH</i> at $Co = 0.6$ (white iso-surface denotes initial state). The sectional view on the right contains contours 0.25, 0.5 and 0.75.	19
2.12	Mass error( $\epsilon$ ) at a) $Co = 0.35$ b) $Co = 0.6$ and c) $Co = 0.9$ for single vortex test.	20
2.13	Iso-surfaces for 0.5 volume fraction for the deformation test using a) <i>CUIBS</i> and b) <i>FBICS</i> c) <i>M-CICSAM</i> and d) <i>SAISH</i> at $Co = 0.6$ (white iso-surface denotes initial state). The sectional view on the right contains contours 0.25, 0.5 and 0.75.	22
2.14	Mass error( $\epsilon$ ) at a) $Co = 0.35$ b) $Co = 0.6$ and c) $Co = 0.9$ for deformation test.	22
2.15	Free surface evolution of the first breaking dam test case based on Martin et al. <sup>90</sup> .	24
2.16	Comparison between SAISH and experimental measurements <sup>90</sup> of a) liquid front and b) liquid column height with respect to time.	25
2.17	Free surface evolution of the second breaking dam test case based on Araki et al. <sup>91</sup> .	25
2.18	Comparison between SAISH and Araki et al.'s measurements <sup>91</sup> of liquid height in $m$ at a) $x = 0.25m$ and b) $x = 0.75m$ with respect to time in seconds.	26

2.19	The surface plot for static droplet case where no mollification is applied and the density ratio is maintained at 10 (using $\kappa$ formulation by <sup>94</sup> Brackbill et al.). . . . .	27
2.20	Comparison of CSF-HF method with other mollification strategies for the pressure variation along a horizontal line passing through the centre of domain. . . . .	28
2.21	Surface profile for pressure variation in static bubble test case using HF method. . . . .	28
2.22	Rising bubble at time 0.2, 0.35 and 0.5 with $\sigma = 728 \text{ dyne/cm}$ . The results of HF-CSF (black) method and traditional CSF (red) method are compared from current study with <sup>96</sup> Francoise et al. (Internal figures with axes). . . . .	30
2.23	Fork and join method of parallelization. . . . .	31
2.24	Load calculation of subroutines at increasing number of processors. . . . .	32
2.25	Speedup for OpenMP code. . . . .	32
2.26	Cell nomenclature for TVD scheme . . . . .	33
2.27	Comparison of advection schemes for a single shock problem. . . . .	34
2.28	Comparison of advection schemes for a complex one-dimensional discontinuity	34
3.1	Computational domain and boundary conditions for the spatially oscillating jet instability. . . . .	38
3.2	Grid resolution study for the three different grids with refinement ratio of 1.3 in both directions at $y^*=10$ and $t^*=70$ . . . . .	39
3.3	Richardson extrapolation of $ w_z $ at grid size tending to zero. . . . .	40
3.4	Comparison of the oscillation amplitude with experiments <sup>12</sup> for <i>S01</i> simulation. . . . .	41
3.5	Jet development with <i>S01</i> configuration. . . . .	41
3.6	Comparison of the oscillation amplitude with experiments <sup>12</sup> for <i>S02</i> simulation. . . . .	42
3.7	Jet development with <i>S02</i> configuration. . . . .	42
3.8	Deflection of the jet ( $\theta_{jet}$ ) measured at $y^* = 170$ (dashed red) and $y^* = 150$ (solid green) with data retrieved at $\Delta t = 1$ (a) and snapshot of developing jet and its disintegration (b). . . . .	43
3.9	Vorticity and streamlines (solid lines) in the jet (dashed lines) at $t^* = 13$ , 27, 37 and 50 (from left). . . . .	43
3.10	R.H.S. of Equation 3.6 with jet(dashed lines) at $t^* = 60$ . . . . .	44
3.11	R.H.S. of ETE 3.6 at time $t^* = 38$ (a), $t^* = 40$ (b), $t^* = 42$ (c) and $t^* = 44$ (d). . . . .	45
3.12	Contours for $\nabla \cdot I$ and lamb vectors( $I$ ) (green arrows with 0.5 scaling) around a peak in the jet(dashed lines) with vortex force lines (black solid curves). . . . .	46
3.13	Non-dimensional axial velocity ( $v^*$ ) (red markers) and jet thickness (black markers) ( $2h_0$ ) at $x^* = 40$ and $t^* = 60$ where the jet descends into the negative $y^*$ direction of the domain. Solid and dotted lines denote the best fit curves for the respective markers. . . . .	46
3.14	Fluid polygons showing jet interface disintegration mechanism by <i>Kelvin-Helmholtz</i> instability (a) and <i>Rayleigh-Taylor</i> instability (b). . . . .	47
3.15	Effect of Reynolds number ( $Re$ ) on the growth rate ( $A_e/A_0$ ) of the initial perturbation( $A_0$ ) (a) and jet development (b) at $t^* = 68$ . . . . .	48

3.16	Mean Enstrophy ( $\langle   w  _2^2 \rangle$ ) of the jet at $y^* = 150$ with increasing $Re$ . . . . .	48
3.17	Mean transverse vortex force felt by the jet at the leading edge at $y^* = 150$ with increasing $Re$ . . . . .	48
3.18	Effect of Weber number ( $We$ ) on the growth rate ( $A_e/A_0$ ) of the initial perturbation( $A_0$ ) (a) and jet development (b) at $t^* = 74$ . . . . .	49
3.19	Effect of Weber number on the jet thickness in negative $y^*$ direction (a) and jet axial velocity (b). . . . .	49
3.20	Effect of Froude ( $Fr$ ) number on jet deflection traced along the half jet width (a) and its topology using volume fractions (b). . . . .	50
3.21	Fluid polygons displaying the mechanism of primary capillary breakup in an oscillating jet at $t^* = 68$ (a), $t^* = 70$ (b), $t^* = 74$ (c) and $t^* = 80$ (d). . . . .	51
3.22	Effect of inlet velocity profile on jet deflection traced along the half jet width (a) and its topology using volume fractions (b). . . . .	52
3.23	Axial velocity profiles as jet propagates in negative $y^*$ direction. . . . .	52
4.1	Computational domain and boundary conditions for the oscillating jet. . . . .	56
4.2	Effect of grid refinement on a) absolute vorticity ( $\omega_z^*$ ) and b) axial velocity ( $v^*$ ) during $t^* = 10.95$ at $y^* = 40$ and $z^* = 40$ along $x^*$ . . . . .	57
4.3	Jet deflection for three grid levels at $t^* = 11$ with jet iso-surfaces coloured with yellow, red and blue represent Fine, Medium and Coarse mesh resolutions. . . . .	57
4.4	Comparison of present simulations with <sup>12</sup> Asare et al. and linear stability theory. . . . .	58
4.5	Developing oscillating planar liquid jet and its downstream disintegration at $t^* = 27.23$ (volume rendered). . . . .	59
4.6	The development of head vortices shown by iso-surfaces of a) volume fraction ( $\phi = 0.5$ at $Re = 4500$ ) and vortex structures ( $Q = 0.05$ ) for b) $Re = 4500$ and c) $Re = 500$ with contours denoting magnitude of stream-wise velocity $v^*$ . . . . .	60
4.7	Comparison between the enstrophy values of THV and BHV for the jet at $Re = 4500$ and $Re = 500$ along $x-axis$ . . . . .	61
4.8	Schematic of the hairpin vortex formation at the jet front over the plane perpendicular to the stream-wise direction. . . . .	61
4.9	Q-criterion iso-surfaces ( $Q = 0.05$ ) of the head vortices forming hairpin vortices at a) $Re = 4500$ and its damping at b) $Re = 500$ (red arrows denote velocity vectors scaled by factor of 0.5). . . . .	62
4.10	The velocity profile along $x - axis$ placed at $y^* = 45$ and $z^* = 40$ a) and velocity magnitude of the fluid expelling from hairpin vortices at jet front along $z - axis$ at $x^* = 40$ and $y^* = 45$ b). . . . .	62
4.11	Q-criterion iso-surfaces ( $Q = 0.05$ ) for a) $Re = 4500$ and b) $Re = 500$ at $t^* = 18.74, 22.23$ and $27.23$ . . . . .	63
4.12	Comparison of time-averaged stream-wise entrainment between $Re = 4500$ and $500$ . . . . .	64
4.13	Formation and merging of KH rollers behind the jet front ( $Re = 4500$ ) shown by a) schematic and the numerical results for KH rollers b) forming at $t^* = 16.32$ and their c) merging at $t^* = 18.2$ for $Q = 0.05$ (white) sliced by z-normal plane ( $z^* = 38$ ) with deflected jet (blue). . . . .	65

4.14 The magnitude of span-wise stretching, stream-wise tilting and normal tilting of KH roller and vortex at jet deflection along $y - axis$ (segment A-B in Fig. 4.13(b)) at $t^* = 16.32$ for a) $Re = 4500$ and b) $Re = 500$ ( $j$ being a repeating index). . . . .	65
4.15 Span-wise vortices interacting at $Re = 500$ shown by $Q = 0.05$ (white) and jet (blue) iso-surfaces captured at $t^* = 18.2$ . . . . .	66
4.16 Formation of hairpin vortices shown by a) schematic and the numerical results for b) $Re = 4500$ with red arrows denoting velocity vectors and c) $Re = 500$ for $Q = 0.05$ . . . . .	67
4.17 The velocity profile along $x - axis$ obtained inside three hairpin vortices at the sides (with 1 being near the inlet (Fig. 4.16(b))) for a) $Re = 4500$ and b) $Re = 500$ . . . . .	68
4.18 Stream-wise vortex bursting phenomenon at $Re = 4500$ . . . . .	68
4.19 Kinetic energy content of POD modes for a) $Re = 4500$ and b) $Re = 500$ . .	70
4.20 Velocity vector contours for eigenfunctions of first five dominant POD modes for a) $Re = 4500$ and b) $Re = 500$ over $xy - plane$ . . . . .	71
4.21 Velocity vector contours for eigenfunctions of first five dominant POD modes for a) $Re = 4500$ and b) $Re = 500$ in $yz - plane$ . . . . .	72
4.22 Variation of first five POD coefficients with time for a) $Re = 4500$ and b) $Re = 500$ . . . . .	73
4.23 Ritz values ( $\lambda_i$ ) in complex plane for a) $Re = 4500$ and b) $Re = 500$ . . .	74
4.24 Velocity vector contours for eigenfunctions of first five dominant DMD modes for a) $Re = 4500$ and b) $Re = 500$ in $xy - plane$ . . . . .	75
4.25 Velocity vector contours for eigenfunctions of first five dominant DMD modes for a) $Re = 4500$ and b) $Re = 500$ in $yz - plane$ . . . . .	76
5.1 Computational domain and boundary conditions for a) synchronous and b) asynchronous oscillating jets. . . . .	80
5.2 Development of tandem oscillating jets for nozzle spacing a) $N_1 = 19h_0$ , b) $N_2 = 14h_0$ and c) $N_3 = 9h_0$ . . . . .	81
5.3 Velocity profiles along a segment A-B (Fig. 5.2) placed between the upward plumes of the two jets. . . . .	82
5.4 Phase averaged <sup>64</sup> velocity profiles of tandem oscillating jets in the stream-wise direction for nozzle spacing a) $N_1 = 19h_0$ , b) $N_2 = 14h_0$ and c) $N_3 = 9h_0$ at $z^* = 40$ . . . . .	83
5.5 Comparison between growth of oscillation amplitudes ( $A_e/A_0$ ) associated with tandem oscillating jets at different nozzle spacing. . . . .	84
5.6 Comparison of the enstrophy values ( $\omega_z^2$ ) at a typical oscillation peak ( $y^* = 93.5$ ) at different nozzle spacings. . . . .	84
5.7 Oscillating tandem jets (blue) having nozzle spacing $9h_0$ with their a) fundamental vortical structures ( $Q = 0.05$ ) and b) enlarged view of the interaction zone (vortical structures in white) depicting the velocity vectors (red) at $t^* = 18.25$ . . . . .	85
5.8 Enstrophy values along a segment A-B (Fig. 5.7(b)) placed between the interacting vortices. . . . .	85
5.9 Formation of hairpin vortices due to the interaction of THV and BHV in $9h_0$ nozzle spacing configuration at $t^* = 20.25$ . . . . .	85

5.10 Comparison of a) vortex interaction point and b) normalized time averaged mass entrainment for different nozzle spacing. . . . .	86
5.11 Development of <i>asynchronous</i> tandem oscillating jets for nozzle spacing a) $N_1 = 19h_0$ , b) $N_2 = 14h_0$ and c) $N_3 = 9h_0$ . . . . .	87
5.13 Comparison between growth of oscillation amplitudes ( $A_e/A_0$ ) associated with <i>synchronous</i> tandem oscillating jets at different nozzle spacing. . . . .	88
5.12 Phase averaged <sup>129</sup> velocity profiles of <i>asynchronous</i> tandem oscillating jets in the stream-wise direction for nozzle spacing a) $N_1 = 19h_0$ , b) $N_2 = 14h_0$ and c) $N_3 = 9h_0$ at $z^* = 40$ . . . . .	89
5.14 Enstrophy values for <i>asynchronous</i> tandem oscillating jets along $x - axis$ with $z^* = 40$ at $y^* = 95$ , $y^* = 45$ and $y^* = 25$ (from left) for nozzle spacing a) $N_1 = 19h_0$ , b) $N_2 = 14h_0$ and c) $N_3 = 9h_0$ . . . . .	90
5.15 Asynchronous oscillating tandem jets (blue) having nozzle spacing $9h_0$ with their vortical structures ( $Q = 0.05$ ) (white) sliced at $z^* = 40$ and an enlarged view of the interaction zone depicting the velocity vectors (red) scaled by factor of 0.5. . . . .	91
5.16 Asynchronous oscillating tandem jets (blue) for nozzle spacing $9h_0$ with the velocity vectors (red) scaled by factor of 0.5 depicting the staggering of jet fronts. . . . .	92
5.17 Development of vortical structures ( $Q = 0.05$ ) in asynchronous jets with nozzle spacing of $9h_0$ . . . . .	92
5.18 Comparison of normalized time averaged stream-wise mass entrainment in asynchronous jets for different nozzle spacing. . . . .	93



# List of Tables

2.1	Fluid interface configurations for a single cell . . . . .	10
2.2	Average $L_1$ error and computational time( $CT$ ) for single vortex test for various methods at different Courant values. . . . .	20
2.3	Convergence rate based on $L_1$ error for the single vortex test at $Co = 0.6$ . . . . .	21
2.4	Average $L_1$ error and computational time( $CT$ ) for deformation test for various methods at different Courant values. . . . .	23
2.5	Convergence rate based on $L_1$ error for the deformation test at $Co = 0.6$ . . . . .	23
2.6	The comparisons of the maximum spurious velocity ( $m/s$ ) is performed after time first and $50^{th}$ cycle respectively (The convolution method used here is $K_6$ ). . . . .	29
3.1	Physical Properties and Non-Dimensional Parameters. . . . .	38
3.2	Nozzle configuration and inlet parameters used by <sup>12</sup> Asare. . . . .	40
3.3	The non-dimensional parameters used for the simulations $S01$ and $S02$ . . . . .	41
4.1	Inlet parameters and flow conditions used for the present study . . . . .	56
4.2	Nozzle configuration and inlet parameters used by <sup>12</sup> Asare et al. . . . .	58



---

# CHAPTER 1

---

## INTRODUCTION

The sinusoidal perturbations at an inlet of the liquid jet induce oscillations in it, and the amplitude of these oscillations grow downstream to cause instability in the jet. Such spatially oscillating jets (sweeping jets) in practical applications are produced using a *fluidic oscillator*, as shown in Fig. 1.1. The fluid emerging out of the feedback channels inside the *fluidic oscillator* deflect the incoming fluid and produces the oscillation pattern in the jet. These deflections are periodic and utilize the *Coanda effect* to form the oscillating jet through a nozzle<sup>1</sup>.

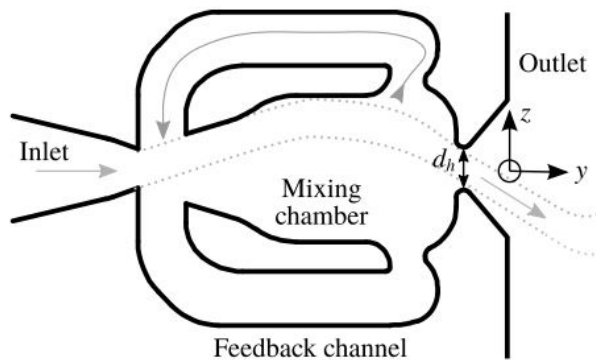


Figure 1.1: Working principle of fluidic oscillator<sup>1</sup>

An ability of a *fluidic oscillator* to produce spatially oscillating jets without making use of any moving parts has made it popular within industrial applications. In a typical combustion process, it is crucial to achieve proper atomization of fuel and its mixing with the surrounding air. These characteristics are essential for better combustion efficiency and to have lower emission. The usage of an oscillating jet can achieve this as it provides better atomization and spread as compared to a steady jet<sup>2</sup>. Moreover, the electronic integrated circuits can be provided with an efficient cooling mechanism if these jets are used instead of the traditional straight jets, which produce hotspots because of their uneven thermal distribution<sup>3,4</sup>. Another important application of these jets is found in active flow control technologies, where flow over a surface is controlled with the help of sweeping jets. To achieve this flow control, grooves are made on a surface in which the *fluidic oscillators* are placed, and their fluid logic controls the separation and reattachment of the boundary layer as needed<sup>5</sup>. The oscillating jets have also proven their efficacy in flow measurements<sup>6,7</sup> and the mixing or separation of chemical components<sup>8</sup>.

An information regarding the stability of any liquid jet and how its surrounding fluid affects it is vital in designing an industrial application. Moreover, in certain applications it is also important to know how effectively the jet entrains a surrounding gas and how mixing of the two fluids occur in specific applications. If multiple jets are to be used for a particular purpose, it is also essential to gather information regarding their interactions. These fundamental questions are needed to be investigated to understand the jet behaviour and concurrently improve the performance of an application in which it is being used.

The numerical simulations provide important insights into the liquid jet behaviour. Thus, the important length scale in analysing oscillating jets is the nozzle width as it is the smallest dimension in the domain. Moreover, the time-scaling for such flows depend on the jet velocity and nozzle width. Furthermore, the non-dimensional numbers such as *Reynolds number* ( $Re$ ), *Weber number* ( $We$ ) and *Froude number* ( $Fr$ ) become important as they provide the comparison between the inertia forces (that dominate jet flows) and other forces such as surface tension and gravity.

## 1.1 Stability of Planar Liquid Jets

An initial study about the instability in liquid sheets evolving in the quiescent surrounding was conducted by<sup>9</sup> Squire and<sup>10</sup> Hagerty. They demonstrated the existence of two modes of instabilities named varicose and sinuous, where the latter is the most unstable if  $We \gg 1$ . As linear theory was considered by both the studies, sheet thickness was assumed to be uniform, and thus, it was difficult to explain the sheet breakup phenomenon. Therefore,<sup>11</sup> Clarke performed a second-order analysis of instability to understand the stability of jet and demonstrated that the wave growth is a combination of both sinuous mode and dilatational first harmonic, which makes it non-linear and asymmetric. Until then, the temporal analysis for the instability was followed that assumes the disturbance in a jet to grow with time everywhere in domain but, these disturbances in practice also grow spatially. This issue was tackled by<sup>12</sup> Asare and<sup>13</sup> Li in their study and demonstrated that if the liquid velocity is high, then Gaster's co-relation can relate the spatial and temporal growth rates of the disturbances in a jet.<sup>12</sup> Asare also demonstrated that at the larger forcing amplitudes, the growth of disturbances becomes non-linear and exhibit sharp sawtooth-shaped liquid interface. On the other hand,<sup>13</sup> Li showed that viscosity stabilizes the sinuous perturbations if  $We \gg 1$ . An interesting study was performed by<sup>14</sup> Schmid and Henningson where the falling liquid sheet is subjected to an air cushion on one side while the other being exposed to the surrounding. Thus, they reported that the perturbations in such a liquid sheet cause pressure fluctuations in the air cushion that is coupled with the sheet perturbations and initiate another disturbance.

Studies investigating jet stability also concentrated on understanding the development of a liquid sheet subjected to a co-flowing gas stream.<sup>13</sup> Li demonstrated that as the liquid sheet is subjected to an unequal co-flowing gas stream, an increase in these gas velocities will increment the degree of sinuous instabilities such that the viscosity acts as a stabilizing force. Besides, if the liquid sheet is disturbed and the gas velocity is incremented gradually, it was demonstrated by<sup>15</sup> Tammisola et al. that these disturbances stabilize at first and then become unstable as the gas velocity surpasses the liquid velocity. This behaviour changes if this shear flow is confined.<sup>16</sup> Rees and Juniper showed that the destabilizing effect of such confinement would augment in the presence of surface tension. Moreover, the effects of velocity profiles on jet instability were studied by<sup>17</sup> Rao and Ramamurthi,

and<sup>18</sup> Soderberg and Alfredsson demonstrated that the linear, parabolic and symmetric velocity profiles would stabilize the disturbances in a liquid sheet more as compared to a uniform profile.

Due to an improvement in computational capabilities, the studies based on numerical simulations have increased over the past few decades.<sup>19</sup> Lopez et al. carried out the spatial numerical simulations for the liquid jet accompanied by a high-speed co-flowing gas using the VOF method. They demonstrated that the strain and pressure fields formed due to the vortex structures in a gas lead to liquid sheet oscillations.<sup>20</sup> Lozano et al. supported this by performing the temporal simulations based on the *vortex dynamics method* and demonstrated that *Kelvin-Helmholtz* (KH) instability is responsible for an unstable jet. Corrugations on the liquid sheet that eventually cause the KH instability are generated by turbulence in the liquid sheet.<sup>21</sup> Desjardins and Pitsch performed temporal simulations over the liquid sheet in the quiescent air using the level-set-based solver and showed that the grid size should be based on the cell Weber number to capture accurate droplet formation.<sup>22</sup> Klein and<sup>23</sup> Scardovelli and Zaleski showed the importance of two-dimensional simulations where they stated that such simulations could depict the evolution of jet accurately in the near field, but still, at the downstream where jet breaks-up, the three-dimensional flow features become more important. Recently,<sup>24</sup> Schmidt et al. performed simulations for the spatially oscillating jet by neglecting gravity to understand the breakup mechanism of these jets. These simulations were based on a PLIC-VOF solver with adaptive mesh refinement and demonstrated that the breakup of a liquid interface occurs due to the combined effects of the KH and RT instabilities.

## 1.2 Coherent Structures in Planar Liquid Jets

A turbulent fluid mass that has a phase correlated vorticity over the extent of its entire structure is known as a coherent structure<sup>25</sup>. These vortical structures provide the momentum and mass exchange across the shear layer. Complex flow field can be characterized into relatively much simpler coherent structures. Such flow structures often provide essential information about the physical behaviour of the flow field. Such fundamental studies can also provide meaningful insights into the complicated flow field produced by the jets subjected to spatial or temporal perturbations.

The phenomenon of *axis switching* dominates flow dynamics of steady planar liquid jets. The numerical study performed by<sup>26</sup> Grinstein et al. showed that such switching of the jet axis is due to nozzle corners which provide sharp curvatures and cause a self-induced deformation. These axis switching vortex ring structures also go through the *leapfrogging* process, where the leading vortex ring spreads out and remains intact, whereas the ring that penetrates it is destroyed to form the stream-wise braid structures<sup>27</sup>. Moreover,<sup>27</sup> Grinstein et al. also showed that the stream-wise vortices are produced due to the stretching of the braid region between two adjacent vortex rings. A detailed study about the formation of stream-wise and the arc vortices in the vicinity of an individual vortex ring is performed by<sup>28</sup> Wang et al.. The fluid expulsion and insertion from the corners of a vortex ring can result in the formation of hairpin vortices, improving the entrainment of surrounding fluid<sup>29,26</sup>. Although there exists such strong dynamics at the jet corners,<sup>30</sup> Hart et al. demonstrated that the rate of entrainment can increase at the flattened edges as compared to the jet corners at a certain distance to the downstream of nozzle.<sup>31,32</sup> Tsuchiya et al. and<sup>33</sup> Quinn have shown that such fundamental interac-

tions and the turbulent stream-wise intensity are strongly related with the parameters such as aspect ratio and *Reynolds number* ( $Re$ ) of the liquid jet. Such dependence of the developing jet over *Reynolds number* ( $Re$ ) was investigated by<sup>34</sup> Suresh et al., and their study demonstrated that within the shear layer, the formation of large scale structures results in the vortex merging and pairing at larger downstream distances, which leads to more fluid entrainment. This shear layer also leads to the KH instability caused by the disturbed fluid interface and finally leads to the primary breakup of the liquid jet<sup>35</sup>.

The entrainment characteristics and flow field change substantially when a jet is perturbed temporally (unsteady pulsating jet)<sup>36, 37</sup>. Simmons et al. demonstrated that the pulsating jet provides greater entrainment as compared to the steady jet. Supporting this study,<sup>38</sup> Galea et al. also found higher entrainment rates in the pulsating jet and described the existence of periodic head vortices. These periodic head vortices coalesce downstream, providing larger spread and entrainment in these perturbed jets<sup>39, 40</sup>. Similar coalescence of head vortices was reported by<sup>41</sup> Hsiao et al. in their work, where they demonstrated that the stream-wise jet spread occurs in a stepwise manner and is dominated by the evolution of local coherent structures.

Another group of unsteady perturbed jets is the spatially oscillating jets (unsteady sweeping jets). Such jets are formed using the *fluidic oscillators* that make use of the *Coanda effect* for producing oscillations<sup>42</sup>.<sup>12</sup> Asare et al. and<sup>43</sup> Tammisola et al. experimentally studied the instability involved in oscillating jets and concluded that the instability grows exponentially with time. As the oscillating jet develops, the turbulent kinetic energy is dissipated more in the near-field, and the growth of oscillation amplitude saturates<sup>44, 42</sup>. Ostermann et al. reported that the shear layer is stretched and squeezed during the jet oscillations. This is accompanied by downstream convection of head vortices that also produce a local recirculation. Such head vortices result from asymmetric upward jet plumes that cause KH disturbances on an interface behind the leading vortex ring<sup>45</sup>. Schmidt et al.<sup>24</sup> reported about the interaction between stream-wise and crosswise vorticity on the surface of these oscillating jets, which results in instability that leads to a primary breakup.

### 1.3 Planar Liquid Jets in Tandem

A system with multiple jets emanating from the closely spaced nozzles demonstrates an interesting flow field that can achieve the rapid and complete mixing with the surrounding fluid. Such tandem jets find numerous technological applications that involve the mixing and entrainment of fluids. Practical usage of this tandem jet system is associated with boiler burners, waste disposal plumes, fuel injection system, take-off and landing devices in an aeroplane, propulsion and noise control equipments in aerospace vehicles, ejectors, heating ventilation and air conditioning (HVAC) systems etc.

The earlier studies about the fundamental flow field of tandem jets were carried out by<sup>46</sup> Miller and Comings and<sup>47, 48</sup> Tanaka. They identified three fundamental flow regimes in the tandem jet flow: *converging*, *merging* and *combined* flow regions. Moreover, the fluid recirculation occurs between the two jets, resulting in a formation of low pressure region between the two jets. This causes the two jets to converge towards the centreline and eventually merge to form a combined flow. While examining the development of dual jets<sup>49, 50</sup> Lin and Sheu demonstrated that the entrainment and spread of these jets is better than a single jet configuration. These earlier studies were based on *un-ventilated*

nozzles which do not allow the surrounding fluid to enter between the two jets. Thus,<sup>51</sup> Masters performed his studies of tandem jets over the *ventilated* (free standing) nozzles and showed that except merging region, the velocity profiles of the jets are self-similar. The experiments performed to understand the flow features till this point were based on intrusive measurements and, therefore had a certain degree of error associated with them. Hence,<sup>52</sup> Nasr and Lai performed their study using *Laser Doppler Anemometry* (LDA) and determined that if this jet configuration is excited at a frequency similar to the vortex shedding frequency, then the jet merging improves. Furthermore, this merging of the jets is linearly dependent on the nozzle spacing such that an increase in the spacing will lead to an increase in the stream-wise merging point distance<sup>53, 54</sup>. The general characteristics of the flow in dual-jet changes if both jets have unequal inlet velocities. Therefore, if the velocity ratio between the two jets decreases, then the interaction between them is weak, leading to an increase in the merging distance<sup>55, 56, 57</sup>. Lai and Nasr studied the ability of different turbulence models to capture turbulence characteristics of tandem-jet whereas,<sup>58, 59</sup> Wang et al. studied the turbulent mixing in these jets. Therefore, it was demonstrated that interaction between these jets and surrounding fluid is greatest at the periphery due to large velocity gradients. The flow field of tandem jets in a cross-flow was also investigated in the previous studies<sup>60, 61, 62, 63</sup>. In the cross-flow, the leading jet is distorted more than the trailing jet as it is sheltered by the leading jet.

The tandem jet configuration was also explored in the previous studies where the jets are spatially oscillating (sweeping jet).<sup>64</sup> Wen et al. studied two sweeping jets impinging on the wall. They demonstrated that at low Re the flow of tandem jets can be treated similar to isolated jets but with wall vortices interacting with them. At higher Re, these jets are more distorted and do not remain in phase with each other. Furthermore,<sup>65</sup> Tomac and Gregory studied the internal flow field of fluidic oscillators that are producing synchronous oscillating jets. Moreover,<sup>66</sup> Tomac also studied the atomization capabilities of synchronous and asynchronous tandem oscillating jets.

## 1.4 Motivation and Objectives

The earlier discussion on the analysis of liquid jets demonstrated the paucity of understanding about the behaviour of oscillating jets. The literature that investigates the fundamental flow fields of these jets is surprisingly rare. Therefore, although the efficacy of oscillating jets in industrial applications is well proven, the understanding of its fundamental flow field and the effect of the flow properties on it is still obscure. Thus, the aim of the present study is to find answers for the following fundamental questions about the oscillating jet which are not answered by the previous literature,

1. The oscillating jets demonstrate an increase in the perturbation amplitude as they descend into the domain. As reported by<sup>12</sup> Asare et al. the amplitude grows exponentially with the fall distance. However, the fundamental flow field that is responsible for this unstable behaviour remained unclear.
2. The coherent structures in a typical liquid jets such as head vortices, hairpin vortices are discussed in great detail in the literature. However, formation and evolution of the coherent structures that influence the entrainment of surrounding fluids in the oscillating jet is not discussed in the literature. Therefore, the understanding of these vortical structures in an oscillating jet remains unclear.

3. The previous literature exhaustively reports the merging process in liquid jets in tandem and their behaviour after the completion of this process. Conversely, the merging and development process for the oscillating jets in tandem is dissimilar to the typical steady jets. Therefore, information on effect of individual stability, entrainment and merging processes for tandem oscillating jets is obscure.

The investigation of the above research gaps is vital in understanding the basic flow structures and mechanisms that govern its flow field. This information can lead to effective equipment and process designs that will provide better performance characteristics for a given process.

The present study investigates these fundamental questions using a numerical approach. Thus, the initial objective of this study was to develop an in-house multi-phase flow solver and benchmark it with the canonical test cases from the literature. This in-house code, when tested for its accuracy was made parallel to utilize a shared memory-based architecture. This high fidelity solver is used to validate the oscillating liquid sheet experiments by<sup>12</sup> Asare et al. and investigate the stability of these jets. Furthermore, this study is extended to understand the formation and evolution of vortical structures around an oscillating jet. The final objective of the present study is to perform the numerical simulations on the oscillating jets in tandem to understand their interactions and flow development around them.

## 1.5 Overview

The present study is on numerical simulations of oscillating jets, and the results discuss the stability, coherent structures and the interaction of these jets when used in tandem. The structure of this report is as follows. *Chapter 2* provides the details about the in-house code and the solution methodology of the governing equations. Instability associated with oscillating jet and the effect of flow properties on it is discussed in *Chapter 3*. The development of the vortical structures around an oscillating jet and the effect of viscosity on them is discussed in *Chapter 4*. *Chapter 5* demonstrates the results for the interaction of oscillating jets when placed side-by-side and the effect of nozzle spacing on it. Finally, the contributions of the present study are summarised in *Chapter 6*.

---

# CHAPTER 2

---

## NUMERICAL METHODOLOGY

The present numerical methodology adopts one fluid approach where every fluid shares a single set of governing equations<sup>67</sup>. These fluid phases are distinguished based on the individual volume fraction ( $\phi$ ), which is evaluated and tracked throughout the computational domain. These fluid phases in the present study are assumed to be incompressible and treated as a continuum assuming that an interface separating two fluids is sharp. Moreover, the long-range forces between fluid molecules are not considered whereas, an effect such as the surface tension caused due to the intermolecular forces is retained.

### 2.1 Governing Equations

The simulations are based on the Navier-Stokes equations which in their non-dimensional form are expressed as,

$$\iint_{CS} u_j^*.d\vec{A} = 0 \quad (2.1)$$

$$\begin{aligned} \iiint_{C\forall} \frac{\partial u_i^*}{\partial t^*} d\forall + \iint_{CS} (u_i^* u_j^*) . d\vec{A} &= -\frac{1}{\rho^*} \iiint_{C\forall} \frac{\partial p^*}{\partial x_i^*} d\forall + \frac{1}{\rho^* Re} \iint_{CS} (\mu^* \vec{\nabla}^* u_i^*) . d\vec{A} \\ &\quad + \frac{1}{\rho^*} \iiint_{C\forall} F_{STi}^* d\forall - \frac{1}{Fr^2} \iiint_{C\forall} d\forall \end{aligned} \quad (2.2)$$

where the non-dimensional entities are denoted through superscript \*. Here,  $u_i$  and  $u_j$  denote the components of velocity vector with subscripts  $i = 1, 2, 3$  and  $j = 1, 2, 3$  being the non-repeating and repeating indices, respectively. Whereas  $\rho^*$ ,  $\mu^*$  and  $p^*$  represent the density, viscosity and pressure within a computational cell with control surface ( $CS$ ) area as  $d\vec{A}$  and cell volume within a control volume ( $C\forall$ ) as  $d\forall$ . Furthermore,  $Re = \rho_l U h_0 / \mu_l$  and  $Fr = U / \sqrt{gh_0}$  represent the Reynolds number and Froude number, respectively.  $F_{ST}$ , which is the third term on the right-hand side of Equation 2.2 denotes the surface tension force acting at the fluid interface, while the last term represents the gravitational force which can only exist when  $i = 2$ . The mixture properties required at the interface cells are obtained through interpolation using cell volume fraction ( $\phi$ ) as

$$\begin{aligned}\rho^* &= \phi + (1 - \phi)\rho_g/\rho_l \\ \mu^* &= \phi + (1 - \phi)\mu_g/\mu_l\end{aligned}\quad (2.3)$$

such that, the terms with subscript  $l$  and  $g$  indicate properties of liquid and gas phase respectively. The scaling used for the Equation 2.1 and 2.2 is as follows,

$$\begin{aligned}x_i^* &= \frac{x}{h_0}; t^* = \frac{t}{h_0/U}; p^* = \frac{p}{\rho_l U^2}; \\ v_i^* &= \frac{v_i}{U}; \rho^* = \frac{\rho}{\rho_l}; \mu^* = \frac{\mu}{\mu_l}; \phi = \frac{\nabla_{phase}}{\nabla_{cell}}\end{aligned}$$

where the terms  $h_0$  and  $U$  serve as the half nozzle width and scaling velocity(unity for the present study) respectively.

## 2.2 Volume of Fluid Method

An interface between an oscillating liquid jet and the surrounding gas is tracked using the *Volume of Fluid* (VOF) method. The VOF methodology is adopted in the present work over the other methods such as *level-set* and *smooth particle hydrodynamics* due to its better mass, momentum and kinetic-energy conservation property <sup>68</sup>. The volume fraction ( $\phi$ ) of a particular fluid is advected based on the velocity field across the computational cell. An interface between the two fluids in an *Eulerian* grid is tracked using the VOF method<sup>69</sup>, which is an advection equation for the volume fraction ( $\phi$ ) and is given as,

$$\iiint_{CV} \frac{\partial \phi}{\partial t} d\nabla + \iint_{CS} (\vec{V} \phi) \cdot d\vec{A} = 0 \quad (2.4)$$

where the volume fraction ( $\phi$ ) has a value 1 if a cell lies inside the liquid region and 0 if it lies in gas. The two-dimensional results demonstrated in the present study are obtained by using the geometric form of the VOF method, which uses *piecewise linear interface calculations* (PLIC) reconstruction to depict an interface. On the other hand, the three-dimensional results obtained in the present study are based on the algebraic form of the VOF method that uses a novel compressive VOF scheme called *smoothly adapting interfacial scheme based on hybridization* (SAISH).

### 2.2.1 Geometric VOF Method

The geometric VOF method consists of an interface reconstruction (PLIC) step followed by an advection step which in the present study is carried out using an operator split method. The details of these steps are as follows,

#### I. Interface reconstruction:

Reconstruction of the fluid interface in the current study is based on the <sup>70</sup> Rudman algorithm, which is the case-wise PLIC method. In this algorithm following steps are taken to reconstruct an interface,

- i. Calculate the interface normals based on the volume fraction data from a *9-cell* stencil. Here, the <sup>71</sup> Parker and Young's method for the interface normal calculations is used. Fig. 2.1 shows a *9-cell* stencil in which the interface normals for central ( $i,j$ ) cell are evaluated by taking the average of normals at four corner cells (blue).

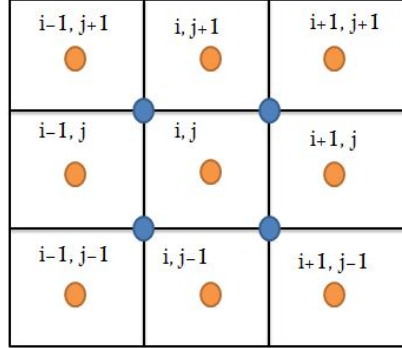


Figure 2.1: 9-cell stencil for interface normals.

Now, if we take the normal component in *x-direction* at upper-right corner of cell ( $i,j$ ) i.e.  $n_{x_{i+1/2,j+1/2}}$  for an uniform grid we have,

$$n_{x_{i+\frac{1}{2},j+\frac{1}{2}}} = \frac{1}{2\Delta x} [\phi_{i+1,j+1} + \phi_{i+1,j} - \phi_{i,j+1} - \phi_{i,j}]$$

Similarly, the normal component in *y-direction* can be written as,

$$n_{y_{i+\frac{1}{2},j+\frac{1}{2}}} = \frac{1}{2\Delta y} [\phi_{i+1,j+1} + \phi_{i,j+1} - \phi_{i+1,j} - \phi_{i,j}]$$

The same procedure can be followed for the other three corners of the central cell and the interface normals can be evaluated as,

$$n_{x_{i,j}} = \frac{n_{x_{i+\frac{1}{2},j+\frac{1}{2}}} + n_{x_{i+\frac{1}{2},j-\frac{1}{2}}} + n_{x_{i-\frac{1}{2},j-\frac{1}{2}}} + n_{x_{i-\frac{1}{2},j+\frac{1}{2}}}}{4}$$

$$n_{y_{i,j}} = \frac{n_{y_{i+\frac{1}{2},j+\frac{1}{2}}} + n_{y_{i+\frac{1}{2},j-\frac{1}{2}}} + n_{y_{i-\frac{1}{2},j-\frac{1}{2}}} + n_{y_{i-\frac{1}{2},j+\frac{1}{2}}}}{4}$$

- ii. Evaluate angle made by the fluid interface with the horizontal using interface normals.

$$\beta = \tan^{-1} \left( -\frac{n_{x_{i,j}}}{n_{y_{i,j}}} \right) \text{ where } -\pi \leq \beta \leq \pi$$

If the grid used is non-uniform then we need to define the angle as,

$$\alpha = \tan^{-1} \left( \frac{\Delta x_i}{\Delta y_i} \tan \beta \right) \text{ where } 0 \leq \alpha \leq \frac{\pi}{2}$$

- iii. Next step is to identify the fluid interface configuration. There are 16 possible interface configurations as shown in Table 2.1.

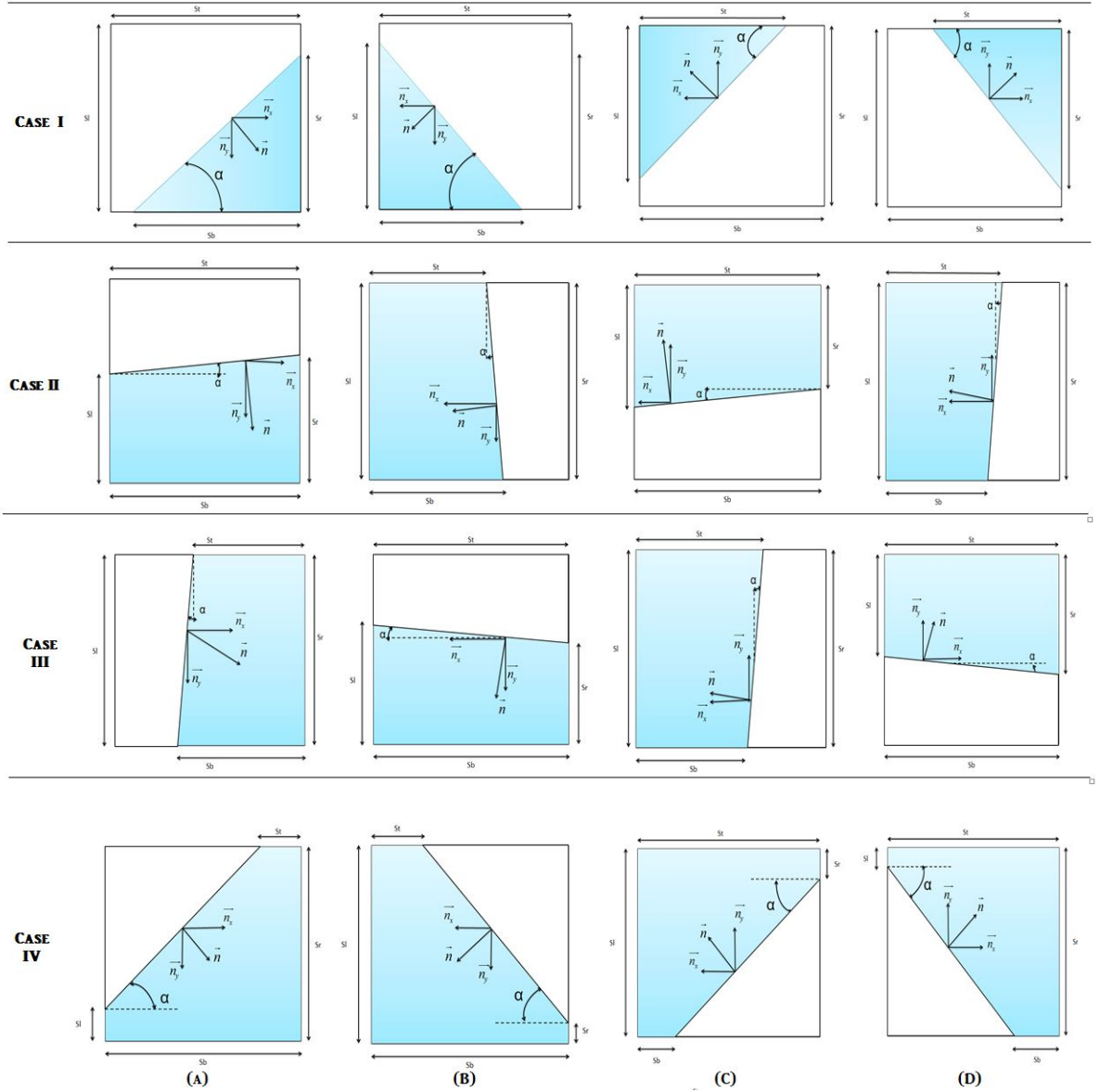


Table 2.1: Fluid interface configurations for a single cell

An appropriate fluid configuration can be selected for a cell using<sup>70</sup> Rudman algorithm as shown below (The sub-cases can be identified by finding the quadrant of an interface normal.),

```

if  $\alpha < \pi/4$ 
    if  $\phi \leq 0.5 \tan\alpha$ 
        Case I
    else if  $\phi \leq 1.0 - 0.5 \tan\alpha$ 
        Case II
    else
        Case IV
else
    if  $\phi \leq 0.5 \cot\alpha$ 
        Case I
    else if  $\phi \leq 1.0 - 0.5 \cot\alpha$ 
        Case III
    else
        Case IV
    
```

- iv. Once the fluid configuration is estimated, the side fractions are calculated geometrically, and the coordinates of intersection points are obtained. The detailed

geometrical relations for these cases can be found in the work of<sup>70</sup> Rudman and<sup>72</sup> Saincher and Banerjee.

The reconstruction tests were performed for known shapes and results of the same are shown here in Fig. 2.2.

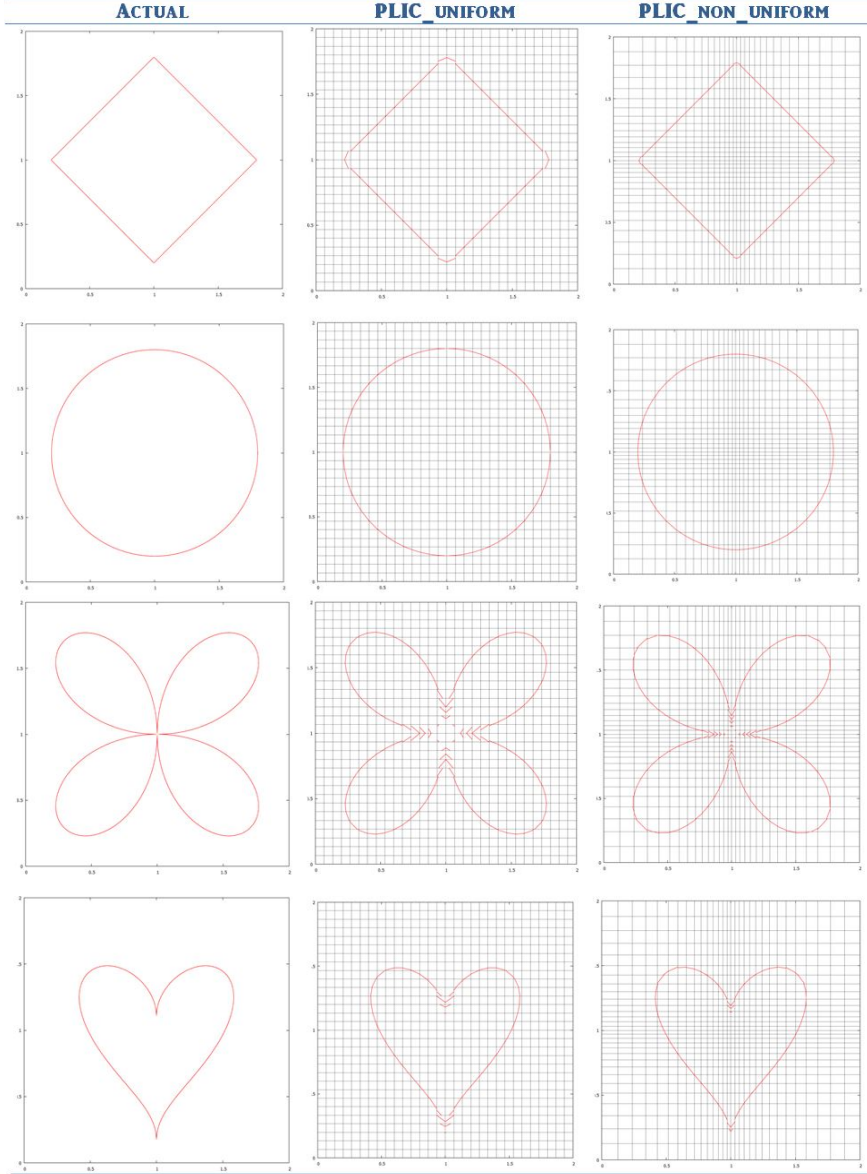


Figure 2.2: Reconstruction (PLIC) test for the uniform and non-uniform grid of  $30 \times 30$  resolution in a square domain of size 2.

## II. Advection:

Equation 2.4 is solved using *Strang splitting*, or generically known as *operator splitting*<sup>73</sup>. Thus, the coordinate splitting provides an opportunity to treat individual equations formed after splitting by customized schemes and gives second-order tem-

poral accuracy. Hence, after operator splitting, the resulting equations are,

$$\begin{aligned} \frac{\partial \phi}{\partial t} \Big|_{n \rightarrow *} + \nabla_x \cdot (u\phi) &= \phi^* \nabla_x \cdot u \\ \frac{\partial \phi}{\partial t} \Big|_{* \rightarrow n+1} + \nabla_y \cdot (v\phi^*) &= \phi^* \nabla_y \cdot v \end{aligned} \quad (2.5)$$

Therefore in Equation 2.5, the *x-sweep* is solved implicitly, whereas the *y-sweep* is solved explicitly. Thus, finite volume based discretized form of these equations can be written as,

$$\begin{aligned} \phi_p^* &= \phi_p^n + \frac{(u_w\phi_w - u_e\phi_e)}{\Delta x \Delta y} \Delta t \Delta y + \phi_p^* \Delta t \Delta y \frac{u_e - u_w}{\Delta x \Delta y} \\ \phi_p^{n+1} &= \phi_p^* + \frac{(v_s\phi_s^* - v_n\phi_n^*)}{\Delta x \Delta y} \Delta t \Delta x + \phi_p^* \Delta t \Delta x \frac{v_n - v_s}{\Delta x \Delta y} \end{aligned} \quad (2.6)$$

Equation 2.6 can also be written in the face-flux form as,

$$\begin{aligned} \phi_p^* &= \phi_p^n + \frac{(F_w - F_e)}{\Delta x \Delta y} + \phi_p^* \Delta t \Delta y \frac{u_e - u_w}{\Delta x \Delta y} \\ \phi_p^{n+1} &= \phi_p^* + \frac{(F_s - F_n)}{\Delta x \Delta y} + \phi_p^* \Delta t \Delta x \frac{v_n - v_s}{\Delta x \Delta y} \end{aligned} \quad (2.7)$$

To evaluate the face fluxes, the appropriate fluid configuration in the cell is selected and geometrical calculations of the face fluxes for all four sides(2D) are performed. The example for this geometrical calculation is demonstrated in Fig. 2.3.

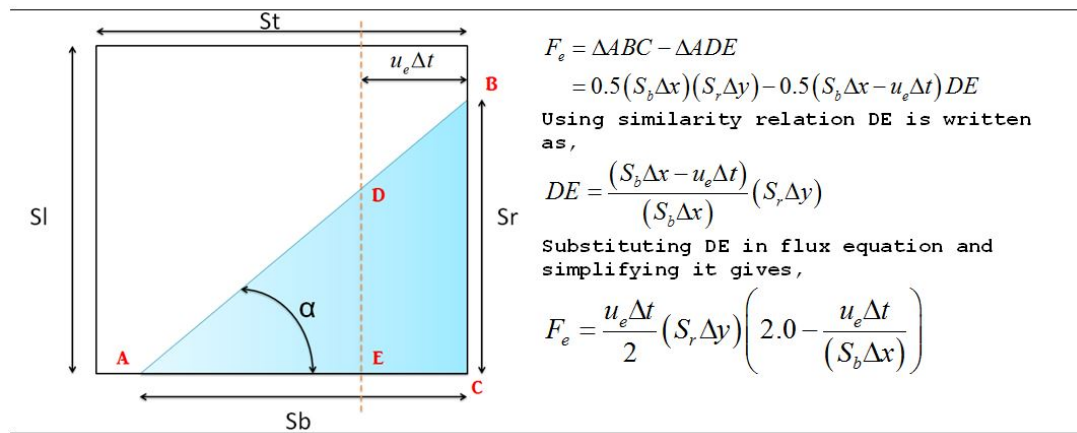


Figure 2.3: Sample calculation of east face flux for Case I.

The advection methodology is validated against the test cases mentioned in work of<sup>74</sup>Rider et al.,<sup>72</sup>Saincher and Banerjee and<sup>75</sup>Ahn and Shashkov. Hence, single vortex test, droplet test, deformation test and Superman flow test is performed to validate the VOF solver and the results are demonstrated in Fig. 2.4.

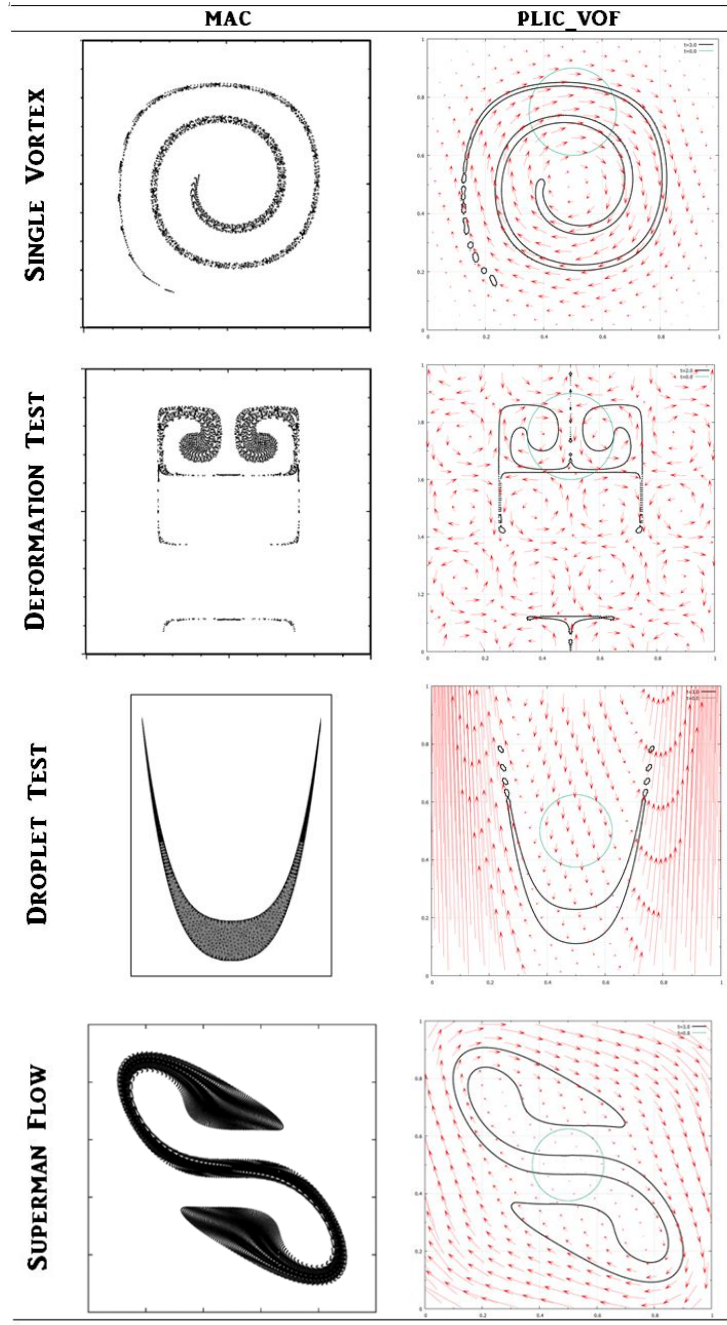


Figure 2.4: Advection test results are presented for unit square domain with grid of  $128^2$  and the having time stepping of  $\Delta t=0.0078125$  for single vortex and deformation test while  $\Delta t = 0.00625$  and  $\Delta t = 0.0025$  for superman flow and droplet flow, respectively.

The VOF solver is coupled with the *Navier-Stokes* solver, and its performance is validated against the *dam-break* test case. This test case was selected to verify the capability of the solver at a high-density ratio. In this test case the water column of unit size is made to collapse in the domain of  $7 \times 1.75$  which is resolved by the grid of  $256 \times 64$ . The Reynolds number for the test is 37629 with a time step size of 0.001, and the simulation is performed for 4000 cycles. The boundary conditions applied for the problem are defined in Fig. 2.5. Interface topology of the *dam-break* case is demonstrated using fluid polygons in Fig. 2.6. Moreover, fluid front results are in agreement with the<sup>76</sup> Raessi et al. as observed from Fig. 2.7.

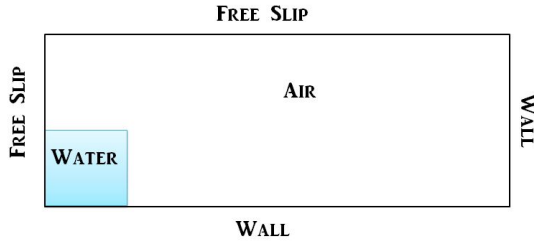


Figure 2.5: Dam break problem setup

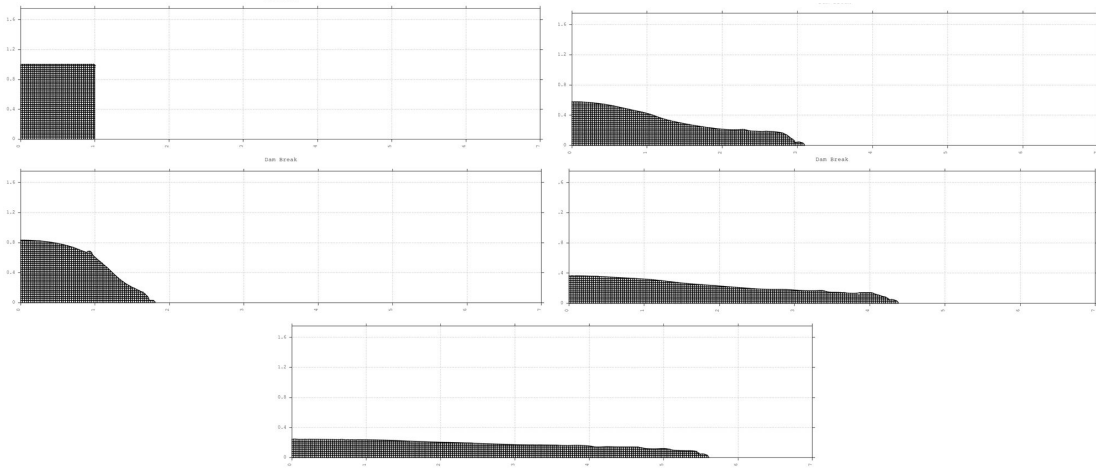
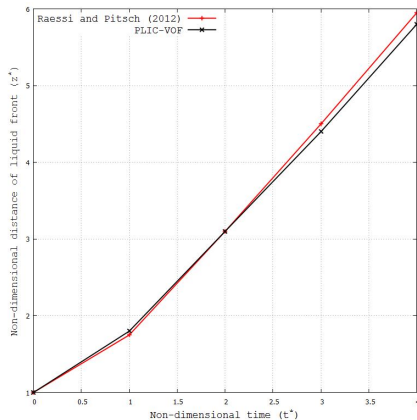


Figure 2.6: Dam break results for non-dimensional time 0, 1, 2, 3 and 4


 Figure 2.7: Fluid front positions with time compared with <sup>76</sup>Raessi and Pitsch

*Rayleigh-Taylor* (RT) instability test case is also performed in order to validate the present solver for complex interfacial topologies. In RT flow instability the heavier fluid is placed on top of the lighter fluid, and when its interface is perturbed with a small disturbance, it grows to cause instability in the flow field. This instability results in some exhilarating mushroom shapes in order to attain the natural equilibrium in the system. An initial perturbation at the interface is given in the form  $y - 0.02 * \cos((1+x)\pi) - 0.2$ . The simulations are carried out for  $T = 8$  with  $dt = 0.001$  time/ time step. The domain of  $1 \times 3$  is discretized by the grid of  $96 \times 288$ ; Re is taken to be 500 and Fr as 0.5. The

density and viscosity ratios for current simulations are taken as 1.2 and 1.0, respectively. The boundary conditions for the current case are taken as a free slip for both side limits of the domain, whereas the wall for upper and lower limit of the domain. The results for this simulation is shown in Fig. 2.8 and is in excellent agreement with<sup>70</sup> Rudman and<sup>72</sup> Saincher and Banerjee. The results demonstrated in Fig. 2.8 for present solver are compared with<sup>70</sup> Rudman and are found to be in agreement with his results.

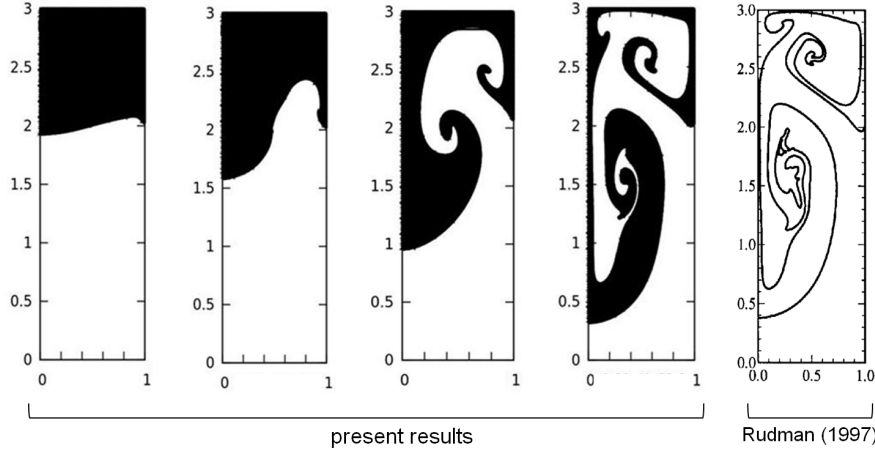


Figure 2.8: The results for RT instability are presented at non-dimensional time of 2, 4, 6 and 8.

### 2.2.2 Algebraic VOF Method

The three-dimensional results demonstrated in the present study are based on the algebraic VOF method. This method is adopted for three-dimensional analysis due to its elegant implementation and its applicability over arbitrary meshes. The scalar field of  $\phi$  is evaluated using transport Equation 2.4, which can be discretized as shown in Equation 2.8.

$$\frac{\phi_p^{n+1} - \phi_p^n}{\Delta t} \forall_p = - \sum_{\text{faces}} \phi_f^n F_f^n \xi + \phi_f^{n+1} F_f^{n+1} (1 - \xi) \quad (2.8)$$

Here, term  $F_f$  is the flux calculated at cell face, which is defined as  $\vec{V}_f \vec{A}_f$ . Here  $\xi$  when takes a value as 0, 1 and 1/2 lead to *implicit Euler*, *explicit Euler* and second-order *Crank-Nicholson* scheme, respectively. The present study uses  $\xi = 1/2$  formulation, which is less diffusive<sup>77</sup>.

The spatial discretization presented in Equation 2.8 requires volume fraction at the cell face, which can be determined with the help of acceptor cell ( $A$ ) and donor cell ( $D$ ), as shown in Figure 2.9 using Equation 2.9.

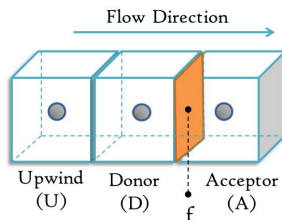


Figure 2.9: Cell nomenclature based on the flow direction.

$$\phi_f = (1 - \beta_f)\phi_D + \beta_f\phi_A \quad (2.9)$$

where,  $\beta_f$  is the weighting function that is obtained using the normalised values of the volume fraction ( $\phi$ ) as,

$$\beta_f = \frac{\tilde{\phi}_f - \tilde{\phi}_D}{1 - \tilde{\phi}_D} \quad (2.10)$$

such that the normalised values denoted by  $\sim$  are defined as,

$$\tilde{\phi} = \frac{\phi - \phi_U}{\phi_A - \phi_U} \quad (2.11)$$

Thus, to find the weighting function  $\beta_f$ , given by Equation 2.10 it is essential that the accurate evaluation of normalized face volume fraction  $\tilde{\phi}_f$  is performed. This evaluation needs to be monotonic and highly resolved to achieve a sharp and accurate interface definition. Thus, as denoted in Equation 2.12,  $\tilde{\phi}_f$  is calculated using the switching between *bounded* (BD) scheme and *high-resolution* (HR) scheme based on the interface orientation.

$$\tilde{\phi}_f = \gamma_f \tilde{\phi}_{BD} + (1 - \gamma_f) \tilde{\phi}_{HR} \quad (2.12)$$

Here,  $\gamma_f = f(\theta)$  is a switching function that attains the value  $0 \leq \gamma_f \leq 1$  based on the interface orientation  $\theta$  which is defined as

$$\theta = \left| \frac{(\nabla \phi)_D \cdot \vec{d}}{|(\nabla \phi)_D| \cdot |\vec{d}|} \right|$$

such that,  $\vec{d}$  is the distance vector connecting centroids of the donor and acceptor cells.

The compressive VOF schemes used to evaluate face volume fraction are based on the *normalised variable diagram* (NVD). Here the normalised volume fraction at the face ( $\tilde{\phi}_f$ ) when it attains the value close to the upwind difference scheme ( $\tilde{\phi}_f = \tilde{\phi}_D$ ) leads to numerical diffusion at the interface, and the scheme loses sharpness. Moreover,  $\tilde{\phi}_f$  value close to the downwind scheme( $\tilde{\phi}_f = 1$ ) sharpens the interface but results in stepping disturbances at the interface.

In this section, the improved compressive VOF method *Smoothly Adapting Interfacial Scheme based on Hybridization* (SAISH) is introduced along with its normalized variable diagram (NVD). SAISH adopts a hybrid approach while defining the bounded and high-resolution schemes. This enables it to provide the required accuracy, robustness and computational efficiency.

A numerical scheme must adhere to the convective boundedness criterion<sup>78</sup> to maintain the volume fractions within  $[0, 1]$  and thereby, must operate within the triangular region enclosed by the lines  $\tilde{\phi}_D = 0$ ,  $\tilde{\phi}_f = 1$  and  $\tilde{\phi}_D = \tilde{\phi}_f$  as shown in Fig. 2.10. Consequently, the *bounded* scheme( $\tilde{\phi}_{BD}$ ) for the proposed method can be represented using normalized variable formulation (NVF) as:

$$\tilde{\phi}_{BD} = \begin{cases} 4\tilde{\phi}_D & 0 \leq \tilde{\phi}_D \leq 1/4 \\ 1 & 1/4 < \tilde{\phi}_D \leq 1 \\ \tilde{\phi}_D & \text{else} \end{cases} \quad (2.13)$$

It can be observed that  $\tilde{\phi}_{BD}$  in the proposed scheme is more compressive than FBICS<sup>79</sup> and CUIBS<sup>80</sup> schemes. This is due to an increased downwinding provided by term  $4\tilde{\phi}_D$  in the bounded scheme as compared to  $3\tilde{\phi}_D$  compression provided by FBICS and CUIBS schemes (refer Fig. 2.10). Moreover, unlike CICSAM<sup>77</sup> and M-CICSAM<sup>81</sup>, the *high-resolution* scheme formulation does not involve *Co* number and thus it free from the *Co* dependence. This allows the proposed scheme to be sharper than other schemes. As discussed earlier, this has a subsequent drawback of creating wrinkles at the interface and therefore, needs to be blended using proper weighting function with non-oscillatory high resolution ( $\tilde{\phi}_{HR}$ ) scheme.

Therefore, to accompany  $\tilde{\phi}_{BD}$  scheme in the present method *High-resolution* scheme ( $\tilde{\phi}_{HR}$ ) comprising of Fromm's<sup>82</sup> difference scheme and *hybrid linear/parabolic approximation* (HLPA) scheme<sup>83</sup> is used. Therefore, the functional relationships for  $\phi_f$  of these schemes are as follows,

$$\begin{aligned} \text{HLPA: } \phi_f &= \phi_D + \frac{(\phi_A - \phi_D)(\phi_D - \phi_U)}{\phi_A - \phi_U} \\ \text{Fromm: } \phi_f &= \phi_D + \frac{(\phi_A - \phi_U)}{4} \end{aligned}$$

The normalised form of these schemes can be observed in Fig. 2.10. It is found through Fig. 2.10 that both these schemes pass through the point  $(0.5, 0.75)$ , which makes them at least second-order accurate<sup>84</sup>. Fromm difference scheme near the origin ( $\tilde{\phi}_D < 1/4$ ) operates out of the TVD region ( $\tilde{\phi}_f = 2\tilde{\phi}_D$ ), which is more prone to oscillatory solutions and in the region  $\tilde{\phi}_D \rightarrow 1$ , it operates within the TVD region by being much sharper. On the other hand, region where  $\tilde{\phi}_D \rightarrow 1$  and  $\tilde{\phi}_D \rightarrow 0$ , HLPA scheme becomes diffusive as it operates near an upwind difference scheme in order to preserve the boundedness of the solution which proves to be advantageous at  $\tilde{\phi}_D \rightarrow 0$ .

The proposed method utilizes the advantages of these schemes by forming a hybrid high-resolution scheme ( $\tilde{\phi}_{HR}$ ) as defined by Equation 2.14 and Fig. 2.10. It is observed from Fig. 2.10 that unlike FBICS and CUIBS, the proposed method operates within the TVD region and thus provides the non-oscillatory solution. Another aspect of the proposed scheme is its smooth switching between the HLPA (initially upwind) and Fromm scheme. This allows the scheme to be computationally efficient as the convergence rates are improved through such switching<sup>85, 86</sup>. Other schemes such as CICSAM, CUIBS, FBICS, M-CICSAM demonstrate sharp changes in the schemes, which are computationally expensive.

$$\tilde{\phi}_{HR} = \begin{cases} \tilde{\phi}_D(2 - \tilde{\phi}_D) & 0 \leq \tilde{\phi}_D \leq 1/2 \\ \tilde{\phi}_D + \frac{1}{4} & 1/2 < \tilde{\phi}_D \leq 3/4 \\ 1 & 3/4 < \tilde{\phi}_D \leq 1 \\ \tilde{\phi}_D & \text{else} \end{cases} \quad (2.14)$$

The switching parameter  $\gamma_f$  that switches between  $\phi_{BD}$  and  $\phi_{HR}$  is a function of the interface orientation  $\theta$  and is based on the suggestion proposed by<sup>87</sup> Heyns et al. where  $\gamma_f = \min(\theta^m, 1)$ . Here,  $m$  is a constant introduced to balance the effect of the schemes used. The value of  $m$  in the present study is set to be two as it provides a better balance between  $\phi_{BD}$  and  $\phi_{HR}$  schemes<sup>87</sup>. The *normalized variable diagram* (NVD) for the proposed method can be depicted from Fig. 2.10. It can be observed here that the  $\tilde{\phi}_{HR}$  scheme lies within the *total variation diminishing* (TVD) regime ( $\tilde{\phi}_f = 2\tilde{\phi}_D$ ) and passes through  $(0.5, 0.75)$ ; therefore, it ensures boundedness and linearity preservation.

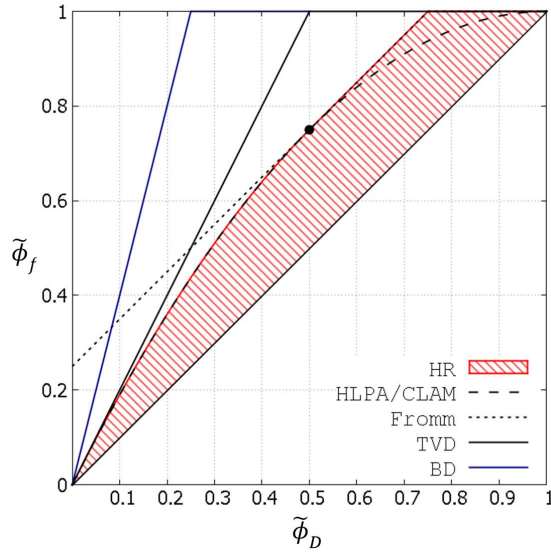


Figure 2.10: NVD for SAISH demonstrating HR and BD regions.

The difficulty associated with the VOF advection is the existence of local extrema that results in overshoots and undershoots in volume fraction values. These un-physical results in the solution are a consequence of integration inaccuracies<sup>88 74</sup>. Such overshoots and undershoots cause the departure of the solution from exhaustive mass conservation capability. This difficulty can be addressed by the use of local redistribution of volume fraction<sup>89</sup>.

The overshoot ( $\phi > 1.0$ ) in volume fraction is dealt with by adding the excess volume fraction to the most filled cell around the cell under consideration. In the same way, undershoot ( $\phi < 0.0$ ) in volume fraction is addressed by removing the required quantity of volume fraction from the least filled cell and adding it to the cell under consideration. This process repeats itself until the volume fraction in each cell achieves boundedness. The results demonstrated in the present study are based on an inclusion of the local redistribution method, and any change in the methodology will be stated accordingly.

Advection of volume fraction using a single vortex flow field is a standard test to evaluate the performance of the numerical method against the shearing flow. Initially the liquid sphere of radius 0.15 is placed at  $(0.5, 0.75, 0.25)$  inside the domain of  $1 \times 1 \times 2$ . This domain is discretized using the grid resolution of  $64 \times 64 \times 128$ . The initial sphere is subjected to the flow field for the period of  $T = 6$  and is defined as:

$$\begin{aligned} u &= \sin(2\pi y)\sin^2(\pi x) \cos\left(\frac{\pi t}{T}\right) \\ v &= \sin(2\pi x)\sin^2(\pi y) \cos\left(\frac{\pi t}{T}\right) \\ w &= \left(1 - \sqrt{(2x-1)^2 + (2y-1)^2}\right)^2 \cos\left(\frac{\pi t}{T}\right) \end{aligned} \quad (2.15)$$

The iso-surfaces for volume fraction 0.5 are depicted in Fig. 2.11 for the defined velocity field at *Courant* number 0.6. The extreme right line plot represent  $\phi$  contours of 0.25, 0.5 and 0.75 on a sectional plane taken at the mid of the final state. It is evident through the comparison shown in Fig. 2.11 that the proposed scheme demonstrates a sharper and accurate interface as compared to other schemes. It is also observed that CUIBS and FBICS exhibit unphysical wrinkles on a surface ( $T/2$ ) due to the compressive

nature of their *HR* schemes. On the other hand, M-CICSAM is free from wrinkles but undergoes mass loss owing to numerical diffusion at higher Courant numbers.

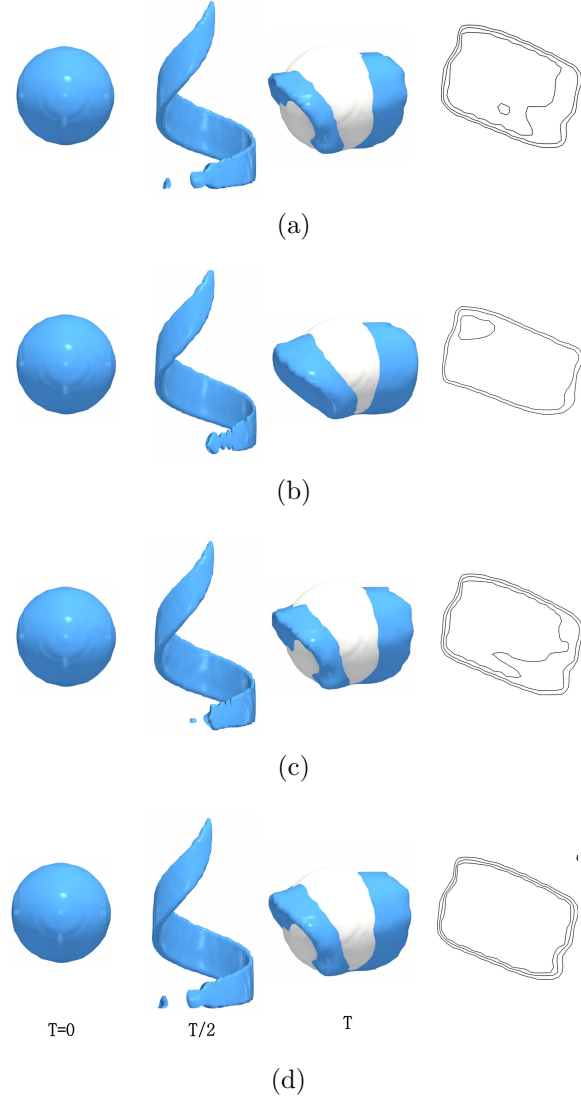


Figure 2.11: Iso-surfaces for 0.5 volume fraction for the single vortex test using a) *CUIBS* and b) *FBICS* c) *M-CICSAM* and d) *SAISH* at  $Co = 0.6$  (white iso-surface denotes initial state). The sectional view on the right contains contours 0.25, 0.5 and 0.75.

The *mass error* ( $\epsilon$ ) for the proposed method is compared with the existing algebraic VOF methods such as CICSAM<sup>77</sup>, CUIBS<sup>80</sup>, FBICS<sup>79</sup> and M-CICSAM<sup>81</sup>. Fig. 2.12 shows mass error for these methods at Courant values of 0.35, 0.6 and 0.9. It can be observed that the proposed method is comparatively robust at elevated Courant conditions and has better mass preserving capability as compared to the other schemes.

The  $L_1$  error and the computational time ( $CT$ ) in CPU seconds associated with the single vortex test obtained using the mentioned methods at different Courant conditions is shown in Table 2.2. The computational time is estimated over the *Intel-i7 (3.4GHz) processor* using the *time()* function of *C++*. It can be observed that SAISH is capable of producing accurate solution with better computational efficiency as compared to other methods. The results of CICSAM method showed significant distortion at  $Co = 0.9$  and thus are not reported in Table 2.2.

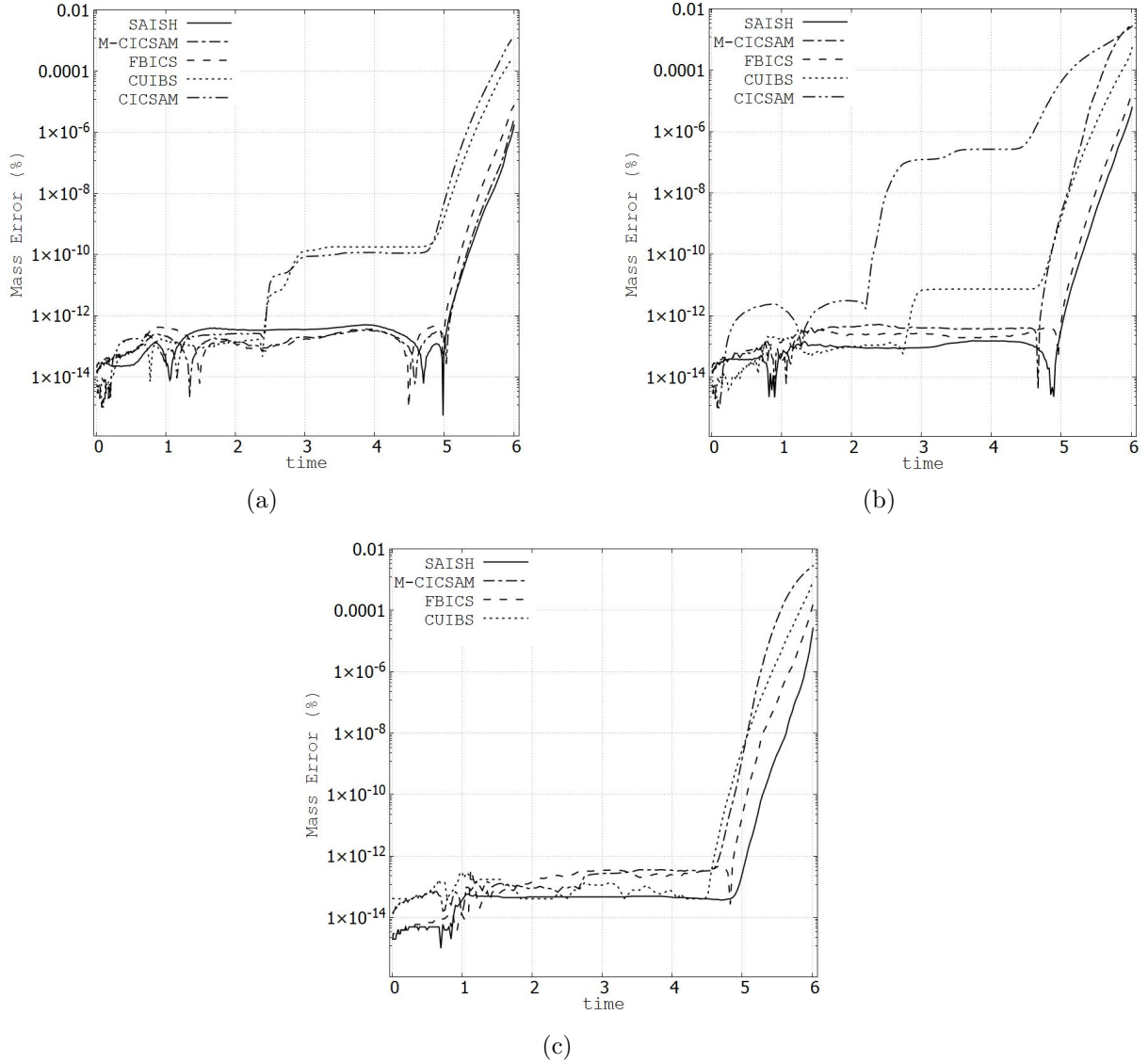


Figure 2.12: Mass error( $\epsilon$ ) at a)  $Co = 0.35$  b)  $Co = 0.6$  and c)  $Co = 0.9$  for single vortex test.

Table 2.2: Average  $L_1$  error and computational time( $CT$ ) for single vortex test for various methods at different Courant values.

Method	$L_1$			$CT$		
	Courant number			Courant number		
	0.35	0.6	0.9	0.35	0.6	0.9
CICSAM <sup>77</sup>	0.98	1.1	--	3401.87	3010.96	--
CUIBS <sup>80</sup>	0.8412	1.01	1.09	3796.5	2997.29	2836.6
FBICS <sup>79</sup>	0.713	0.763	0.8	3700.76	3077.25	2772.7
M-CICSAM <sup>81</sup>	0.6	0.78	0.93	2569.7	2176.08	1997.58
SAISH	0.421	0.65	0.74	2414.11	1947.09	1907.46

The order of convergence is estimated for the proposed scheme based on the  $L_1$  error

at Courant number 0.6 as depicted in Table 2.3. The order( $p$ ) is evaluated as

$$p = \frac{\ln(L_{1(2h)}/L_{1(h)})}{\ln(r)}$$

where,  $h$  and  $r$  denote the grid size and ratio. The convergence rate is observed to improve with grid and has first order accuracy for the present single vortex test.

Table 2.3: Convergence rate based on  $L_1$  error for the single vortex test at  $Co = 0.6$ .

Number of cells	$L_1$	Order
65536	1.5	
524288	0.65	1.21
4194304	0.244	1.41

The second canonical test case deforms the sphere of radius 0.15, whose centre is located at  $(0.35, 0.35, 0.35)$  in the unit cube that is resolved using the grid of  $96 \times 96 \times 96$ . This sphere is subjected to the velocity field for the period of  $T = 3$  and is given as:

$$\begin{aligned} u &= 2 \sin(2\pi z) \sin(2\pi y) \sin^2(\pi x) \cos\left(\frac{\pi t}{T}\right) \\ v &= -\sin(2\pi z) \sin(2\pi x) \sin^2(\pi y) \cos\left(\frac{\pi t}{T}\right) \\ w &= -\sin(2\pi y) \sin(2\pi x) \sin^2(\pi z) \cos\left(\frac{\pi t}{T}\right) \end{aligned} \quad (2.16)$$

Fig. 2.13 demonstrates the qualitative comparison between the proposed method and other methods based on the surface topologies. It can be observed here that the proposed method resolves the interface accurately as fluid volume undergoes thinning while deforming. The sectional contours on the right demonstrate the sharpness of the proposed scheme over other schemes.

Fig. 2.14 shows the comparison of mass error( $\epsilon$ ) between SAISH and the existing VOF methods for the deformation test. It is evident from Fig. 2.14 that the proposed method shows the least magnitude of mass error( $\epsilon$ ) as compared to the other methods when applied to the deformation velocity field. Also, the influence of Courant condition on the proposed method is found to be minimal when compared with the other methods.

The quantitative comparison of the  $L_1$  error and the computational time( $CT$ ) between the proposed method and various other VOF methods for the deformation test is demonstrated in Table 2.4. It can be asserted from the results that, the proposed method efficiently demonstrates better accuracy than the other methods. Moreover, the order of convergence for the proposed method at  $Co = 0.6$  is demonstrated in Table 2.5. It is observed that for the deformation test, second-order accuracy is achieved.

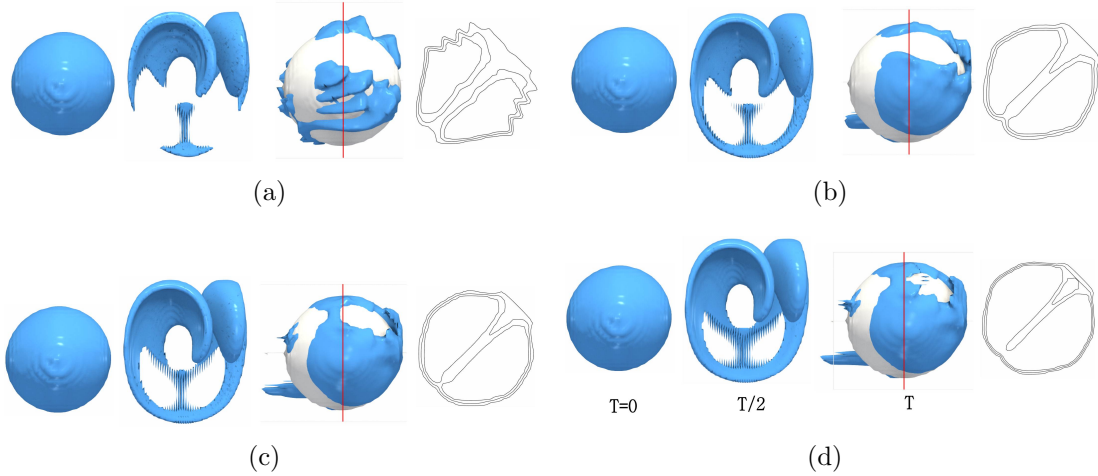


Figure 2.13: Iso-surfaces for 0.5 volume fraction for the deformation test using a) *CUIBS* and b) *FBICS* c) *M-CICSAM* and d) *SAISH* at  $Co = 0.6$  (white iso-surface denotes initial state). The sectional view on the right contains contours 0.25, 0.5 and 0.75.

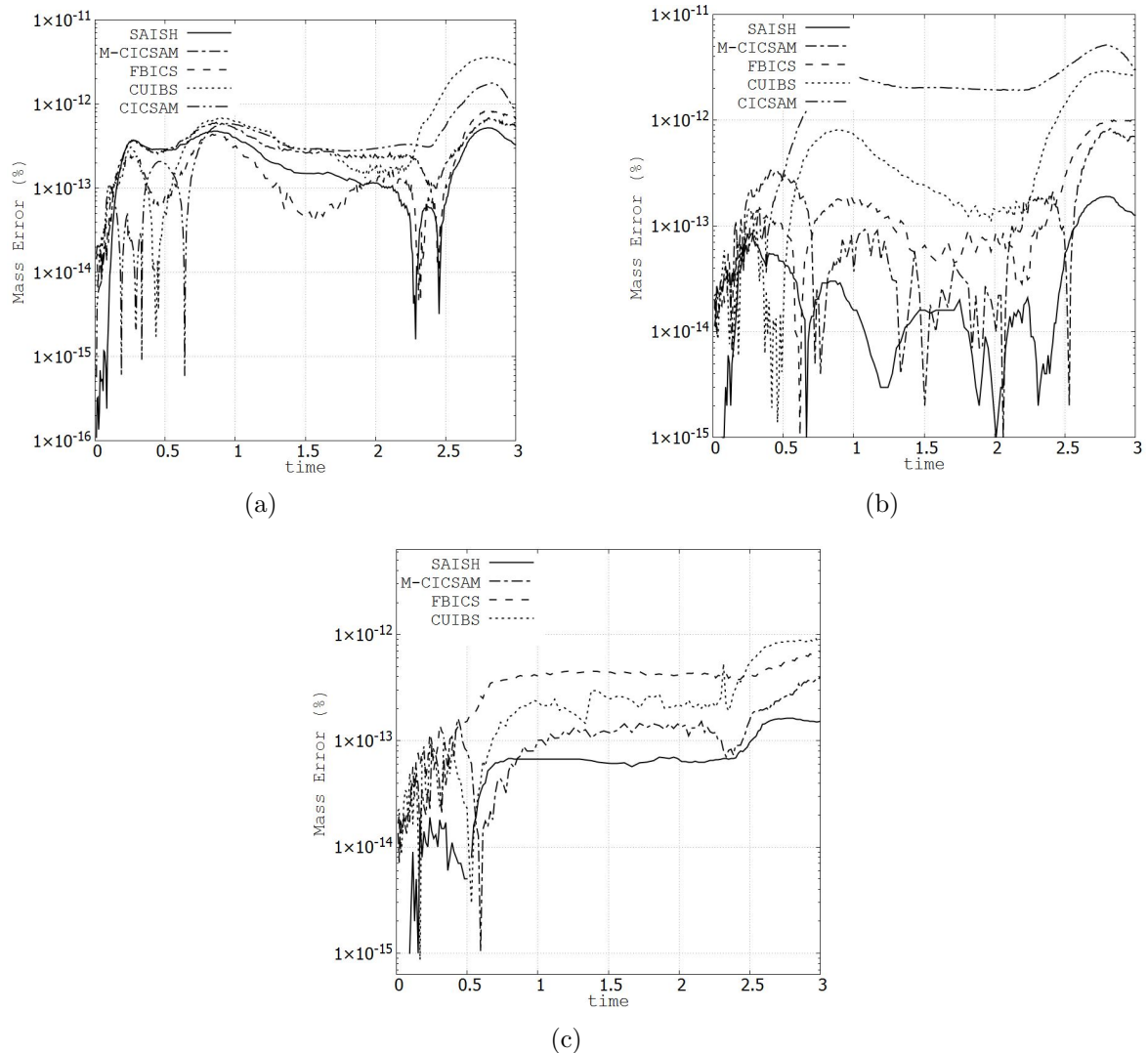


Figure 2.14: Mass error( $\epsilon$ ) at a)  $Co = 0.35$  b)  $Co = 0.6$  and c)  $Co = 0.9$  for deformation test.

Table 2.4: Average  $L_1$  error and computational time( $CT$ ) for deformation test for various methods at different Courant values.

Method	$L_1$			$CT$		
	Courant number			Courant number		
	0.35	0.6	0.9	0.35	0.6	0.9
CICSAM <sup>77</sup>	0.73	0.96	--	1558.95	1161.73	--
CUIBS <sup>80</sup>	0.589	0.726	0.824	1688.97	1250	1099.8
FBICS <sup>79</sup>	0.308	0.579	0.70	1641.41	1433.3	1084.05
M-CICSAM <sup>81</sup>	0.32	0.72	0.83	1179.52	1109.91	817.84
SAISH	0.214	0.28	0.595	1031.42	951.65	742.05

Table 2.5: Convergence rate based on  $L_1$  error for the deformation test at  $Co = 0.6$ .

Number of cells	$L_1$	Order
32768	0.5966	
262144	0.28	1.09
2097152	0.0663	2.08

To test the ability of the proposed scheme to accurately depict the free surface flows, the simulations for a breaking dam are carried out. Thus, the widely used classical test cases of breaking dam by *Martin et al.*<sup>90</sup> and *Araki et al.*<sup>91</sup> is simulated using the proposed method (SAISH). The spatial variables are scaled based on the water column height  $h^*$  whereas the temporal scales are based on  $h^*/U$ , where  $U$  denotes the reference velocity defined as  $\sqrt{gh^*}$ .

In the first breaking dam test case, experiments performed by *Martin et al.*<sup>90</sup> with  $h^* = 2.25\text{inch}$  and configuration of  $n^2 = 1$  are simulated using the proposed method. Therefore, a water column of non-dimensional size equal to the unit cube is made to collapse inside the domain of size  $5 \times 2.5 \times 1$ . This domain which is occupied by air is resolved using the uniform grid of  $256 \times 128 \times 68$ . The top face of the domain is treated by the pressure outlet boundary condition whereas; all other faces are treated as wall. Also, the Courant value for carrying out the simulations is set to be 0.5.

Fig. 2.15 demonstrates the free surface evolution during the collapse of the water column at a different non-dimensional time ( $t^*$ ), while Fig. 2.16 presents the comparison between the proposed method and the experimental measurements<sup>90</sup> for the liquid front and decreasing column height. It is observed that the results are in good agreement with the experiments and thus assert that the proposed method is capable of accurately depicting the free surface flows.

The second breaking dam test selected here is based on the experiments performed by *Araki et al.*<sup>91</sup> with the liquid column height  $h^* = 0.4m$ . This test is selected due to the complicated interface features arising from the sloshing of water, which can prove to be numerically challenging. The simulation is performed by collapsing a water column of size  $1.25 \times 1 \times 1.25$  in an air-filled domain of size  $2.5 \times 2.5 \times 1.25$ . This computational domain is discretized using the grid resolution of  $120 \times 120 \times 60$ . The spatial and temporal

scales used here are identical to the earlier test case with Courant value maintained at 0.5. Moreover, the boundary conditions are kept similar as in the previous test case.

Fig. 2.17 shows the complex sloshing motion demonstrated by the collapsing water column over time. The interface topologies and the air entrapment demonstrated in the present results are in good agreement with both *Lattice Boltzmann Method* (LBM) simulations and the experiments performed by Araki et al.<sup>91</sup>. Also, the quantitative comparisons between the present simulations and the experiments<sup>91</sup> based on the liquid height measurements done at  $x = 0.25m$  and  $x = 0.75m$  are shown in Fig. 2.18. These quantitative comparisons demonstrate good agreement with Araki et al.<sup>91</sup>. The disagreement between experimental measurements and present results at  $t \sim 1.4$  in Fig. 2.18(a) are due to the experimental difficulty in liquid height measurements when bubbles and water mass mix violently as mentioned by Araki et al.<sup>91</sup>. Also, it can be observed that during this period ( $t \sim 1.4$ ) the present simulations agree well with the LBM results obtained by Araki et al.<sup>91</sup>.

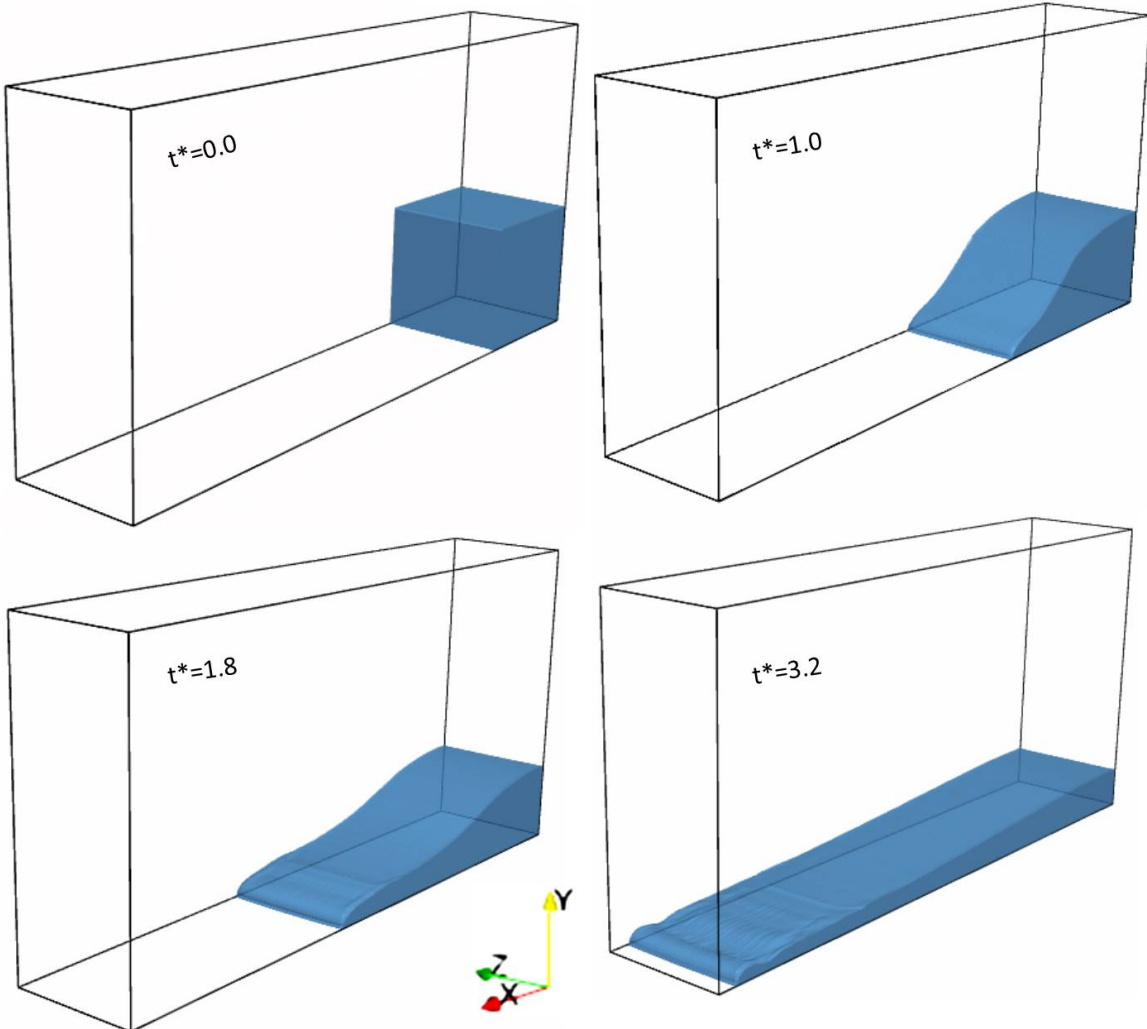


Figure 2.15: Free surface evolution of the first breaking dam test case based on Martin et al.<sup>90</sup>.

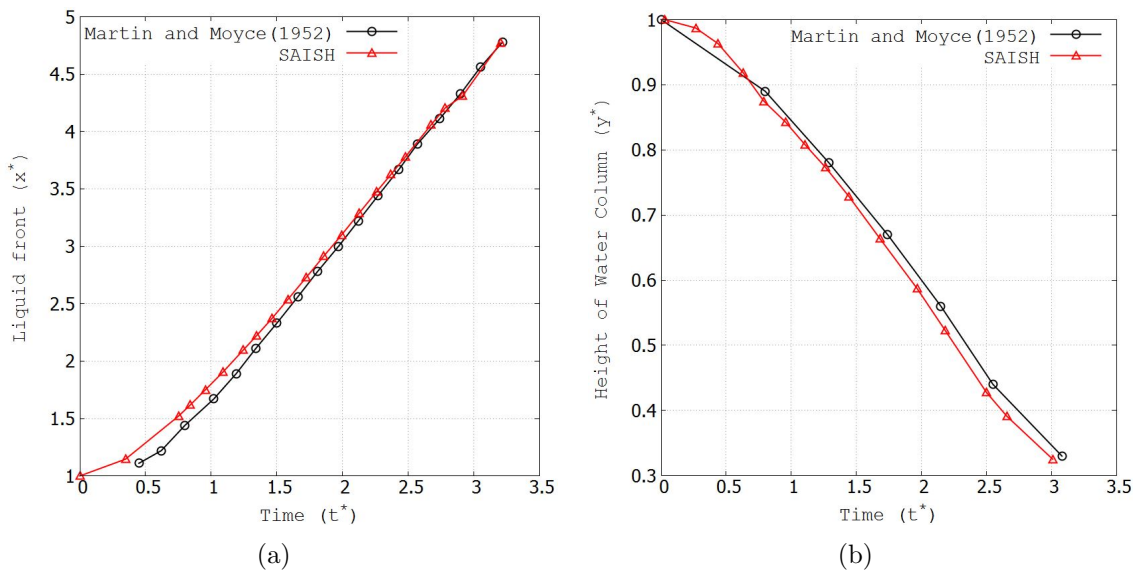


Figure 2.16: Comparison between SAISH and experimental measurements<sup>90</sup> of a) liquid front and b) liquid column height with respect to time.

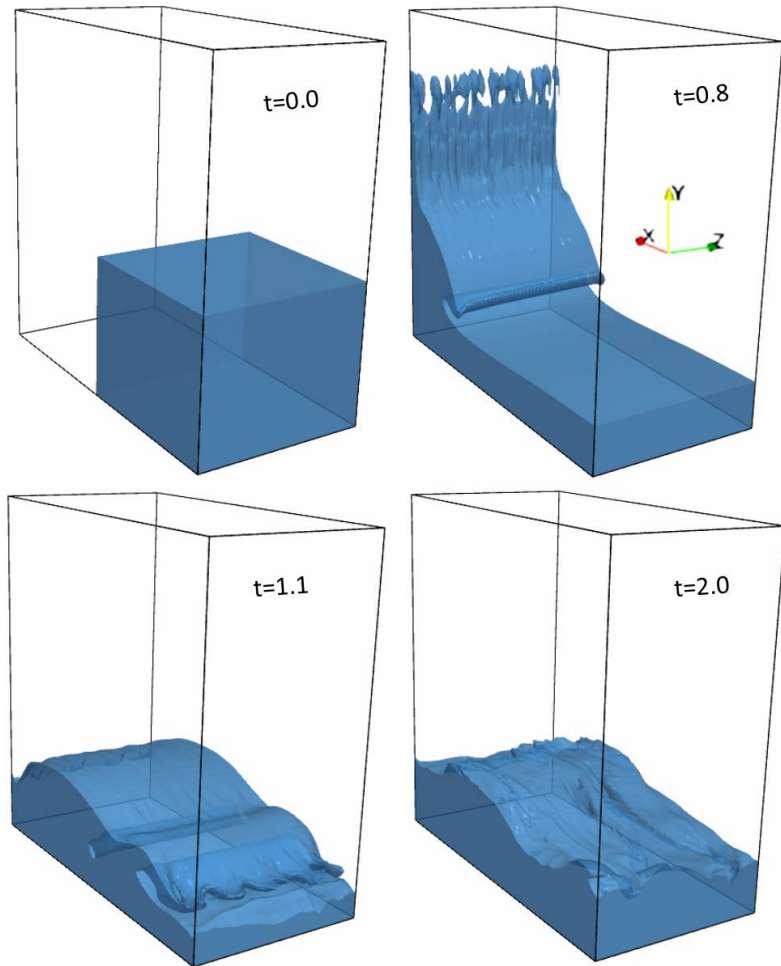


Figure 2.17: Free surface evolution of the second breaking dam test case based on Araki et al.<sup>91</sup>.

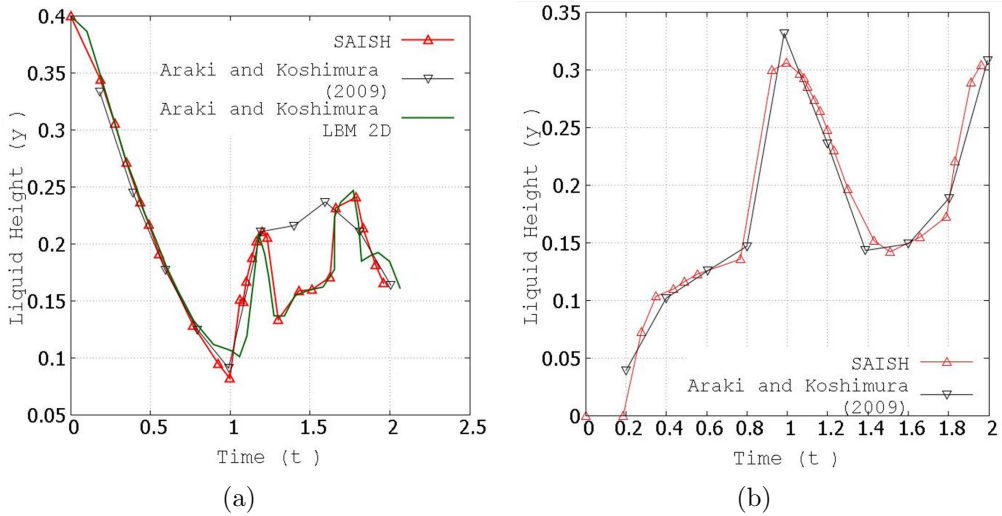


Figure 2.18: Comparison between SAISH and Araki et al.’s measurements<sup>91</sup> of liquid height in  $m$  at a)  $x = 0.25m$  and b)  $x = 0.75m$  with respect to time in seconds.

## 2.3 Surface Tension Modelling

The third term on right-hand side of Equation 2.2 is the surface tension force acting at the interface of two fluids. This term is modelled using the *continuum surface force* (CSF) method<sup>92</sup> and is expressed as,

$$F_{ST_i} = \sigma \kappa n_i \delta_s + \nabla_{\parallel} \sigma \quad (2.17)$$

such that  $\sigma$  denotes the surface tension coefficient,  $\kappa$  is the local mean curvature of the interface, and  $n_i$  serves as the surface normal vector pointing outwards. The Dirac delta function  $\delta_s$  is non-zero only at the interface and is given as  $|\nabla_i \phi| / [\phi]$ , where  $[\phi]$  denotes the maximum jump in volume fraction, which in the current study is unity. The interface interface normal vector is evaluated as  $-\nabla_i \phi / |\nabla_i \phi|$ , and thus, the non-dimensional surface tension force after neglecting *Marangoni forces* ( $\nabla_{\parallel} \sigma$ ) can be written as in Equation 2.18.

$$F_{ST_i}^* = -\sigma \kappa^* \frac{\nabla_i^* \phi}{We [\phi]} \quad (2.18)$$

such that,  $\kappa^* = \kappa h_0$ , and  $We$  represents the Weber number defined as  $\rho_l U^2 h_0 / \sigma$ . The second term on the right-hand side of Equation 2.17 is the variation of the surface tension force along the surface. This typically happens in the real world due to the presence of some impurities and contaminations on an interface and the forces along the surface are known as *Marangoni forces*. These forces are neglected in the entire present work.

The curvature ( $\kappa$ ) in Equation 2.18 is calculated using the height function (HF) method, which provides second-order accurate solution, and its two and three-dimensional formulation is given by Equation 2.19 and Equation 2.20, respectively<sup>93</sup>.

$$\kappa_{2D}^* = \frac{\partial^2 h / \partial x_i^{*2}}{\left[ 1 + \left( \frac{\partial h}{\partial x_i^*} \right)^2 \right]^{3/2}} \quad (2.19)$$

$$\kappa_{3D}^* = \frac{h_{x^*x^*} + h_{y^*y^*} + h_{x^*x^*}h_{y^*}^2 + h_{y^*y^*}h_{x^*}^2 - 2h_{x^*}h_{y^*}h_{x^*y^*}}{(1 + h_{x^*}^2 + h_{y^*}^2)^{3/2}} \quad (2.20)$$

where the fluid height ( $h$ ) is calculated by summing the liquid volumes in the direction most normal to the interface by using the stencil of  $7 \times 3$  (2D) or  $7 \times 3 \times 3$  (3D). In a two-dimensional framework, this method needs to evaluate the most normal direction using  $\max(n_{x^*}, n_{y^*})$  and provide a  $7 \times 3$  stencil in that particular direction. The HF (*height function*) method utilizes the volume fraction values in the given stencil, and based on the below-defined discretization (e.g.  $n_{y^*} > n_{x^*}$ ), the value of curvature is evaluated as (The similar extension to three-dimensions can be made intuitively)

$$\frac{\partial h}{\partial x^*} = \frac{h_3 - h_1}{2\Delta x^*}$$

$$\frac{\partial^2 h}{\partial x^{*2}} = \frac{h_3 - 2h_2 + h_1}{(\Delta x^*)^2}$$

where,

$$h_1 = \sum_{j=3}^{j+3} \phi_{i-1,j} \quad h_2 = \sum_{j=3}^{j+3} \phi_{i,j} \quad h_3 = \sum_{j=3}^{j+3} \phi_{i+1,j}$$

To verify the surface tension model, a canonical test case of the static droplet is considered where the domain of  $8 \times 8$  is resolved using the grid size of  $\Delta x^* = 0.2$  and the fluid droplet has a radius of  $R = 2$ . The surface tension coefficient is taken as 73 dyne/cm and computation is performed for  $t = 0.05$  sec with  $dt = 0.001$  time/time step. An analytical solution for the problem in hand is estimated using the *Young-Laplace* equation, and the resulting pressure difference across the interface is found to be  $36.5$  N/cm<sup>2</sup>. Hence, numerical simulation tries to achieve this pressure difference so that it stands verified.

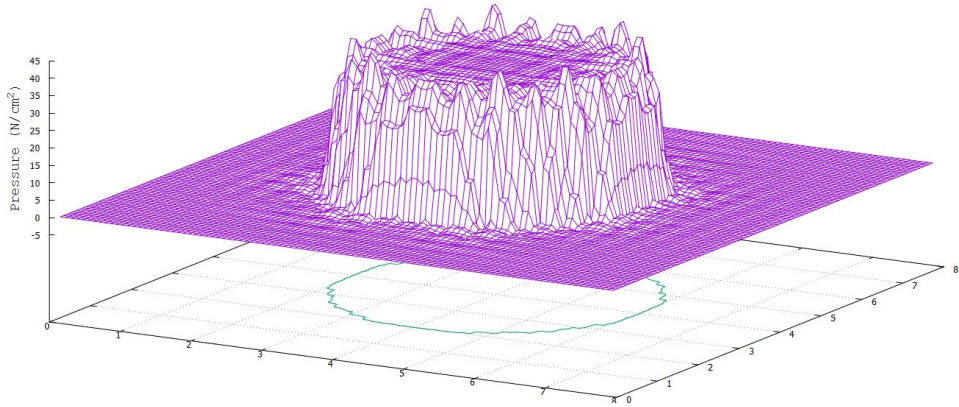


Figure 2.19: The surface plot for static droplet case where no mollification is applied and the density ratio is maintained at 10 (using  $\kappa$  formulation by<sup>94</sup> Brackbill et al.).

As it is observed from Fig. 2.19, the spurious currents cause disturbances at the interface of both fluids when traditional approach<sup>92</sup> is adopted to evaluate  $\kappa$ . These unphysical irregularities are due to an imbalance between surface tension force and pressure. To rectify this issue, mollification of the phase-field needs to be performed to even out

the spikes at an interface. Thus, one of the most commonly used mollification function is the  $K_8$  kernel, but, here we have tested several other mollification functions such as *Gaussian* and *box blur* for their accuracy. Once this smoothing function is obtained, the mollification is carried by multiplying its value in a particular cell with the volume fraction of that cell. The mollifications applied here are for 9 cell stencil, and bandwidth for smoothing is taken as  $1.9\sqrt{\Delta x^*}$ . The comparison of these mollification methodologies using the traditional approach <sup>92</sup> for  $\kappa$  with HF method is depicted in Fig. 2.20. It is observed that the HF methodology depicts the interface accurately with minimal spurious currents at an interface. The surface profile for the static droplet case using HF method is depicted in Fig. 2.21, which captures accurate pressure drop compared to traditional results obtained in Fig. 2.19.

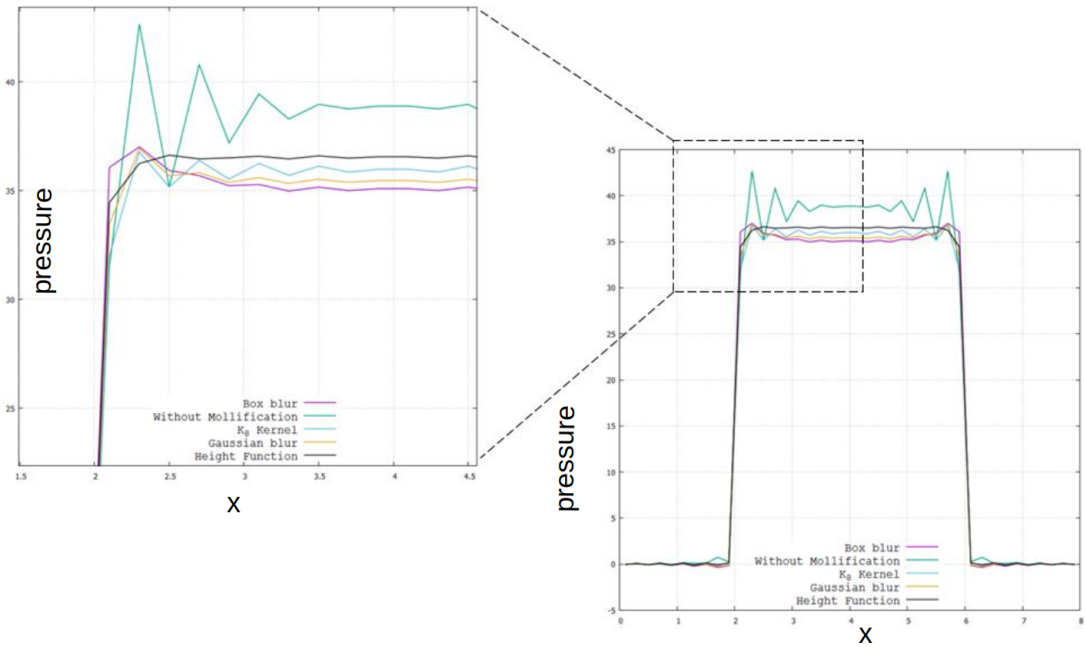


Figure 2.20: Comparison of CSF-HF method with other mollification strategies for the pressure variation along a horizontal line passing through the centre of domain.

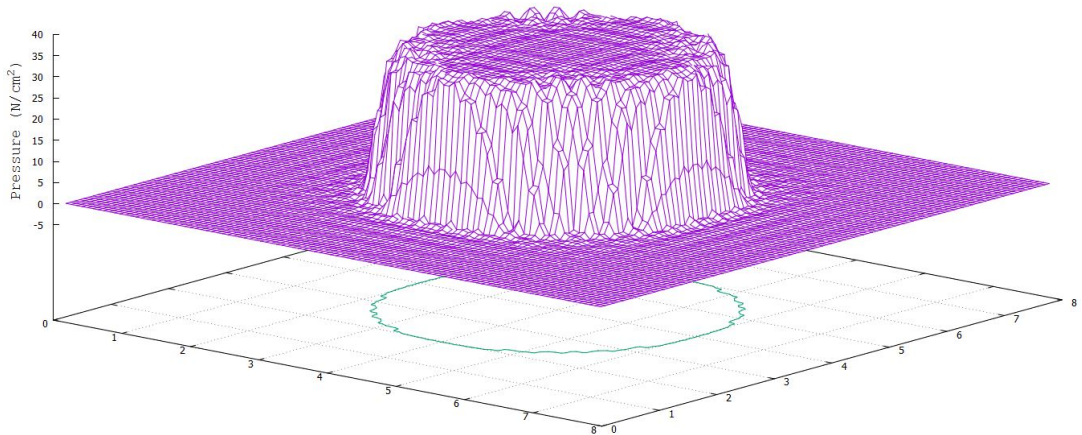


Figure 2.21: Surface profile for pressure variation in static bubble test case using HF method.

The spurious currents at the interface result from an imbalance between the pressure and surface tension force. This happens due to the basic assumption that is made for the surface tension force, where this force is viewed as a volumetric source function defined as  $\iiint_{CV} \sigma \kappa \hat{n} dV$ . The surface tension has to be evaluated at the control surface of the cell rather than its control volume (cell centroid). Hence, this fundamental definition will lead to treating the surface tension force as a tensor (Cauchy's integral theorem (1825)), and the improved definition can be written as Equation 2.21.

$$\iiint_{CV} \nabla \sigma \kappa \hat{n} dV = \iint_{CS} \sigma \kappa \hat{n} \vec{dS} \quad (2.21)$$

The  $\vec{dS}$  in Equation 2.21 has to be continuous to represent Dirac operator in the continuous form. Thus, we can write,

$$\iint_{CS} \sigma \kappa \hat{n} \vec{dS} = \sigma \kappa \hat{n} \delta_s$$

Here, surface Dirac  $\delta_s$  is a digital signal that changes from 1 to 0 or vice-versa but yet it has to be continuous. Therefore, surface dirac can be represented by a Heaviside function which will behave continuously<sup>95</sup> Popinet. The Heaviside function or  $\delta_s$  is represented as  $|\nabla \phi| / [\phi]$ .

The critical part in balancing the forces numerically is to solve these forces at a common point, either at the cell faces or at the centroid of a cell. Thus, the procedure to discretize the surface tension force can be easily understood by Equation 2.22.

$$F_{surf} = \left\langle \langle \sigma \kappa \hat{n} \delta_s \rangle_{c \rightarrow f} \right\rangle_{f \rightarrow c} \quad (2.22)$$

where, the term  $\langle \rangle_{c \rightarrow f}$  denotes linear interpolation from cell centre to faces. The static droplet test was implemented using balanced force algorithm with HF method (non convoluted  $\phi$ ) and without HF (with convoluted  $\phi$ ), and the results of the spurious current for the initial time step and final time step are compared in Table 2.6. It is observed that the spurious currents have reduced for the balanced CSF method as compared to the traditional CSF method <sup>92</sup>.

<b>Method</b>	<b><math>dt=0.001</math></b>	<b><math>dt=0.05</math></b>
<b>Convolution (Francoise)</b>	0.00487	0.163
<b>HF (Francoise)</b>	0.00401	0.0402
<b>Williams (BKZ)</b>	0.349	2.55
<b>Williams (Method I)</b>	0.103	0.846
<b>Williams (Method II)</b>	0.0855	0.386
<b>Convolution (current study)</b>	0.00468	0.0579
<b>HF (current study)</b>	0.00463	0.04279

Table 2.6: The comparisons of the maximum spurious velocity ( $m/s$ ) is performed after time first and  $50^{th}$  cycle respectively (The convolution method used here is  $K_6$ ).

The rising bubble test case is presented here to verify the ability of the balanced force algorithm to capture the interface topology accurately. The domain consists of a  $2 \times 3$  water column with the mesh resolution of  $40 \times 60$  and an air bubble having an initial

radius  $R = 1$  at  $(1,1)$  rises through it. The time-stepping used in this test is  $\Delta t = 0.0001$ . Fig. 2.22 demonstrates the rapid change in curvature ( $t = 0.5$ ) where the HF method provides better results due to its second-order accuracy.

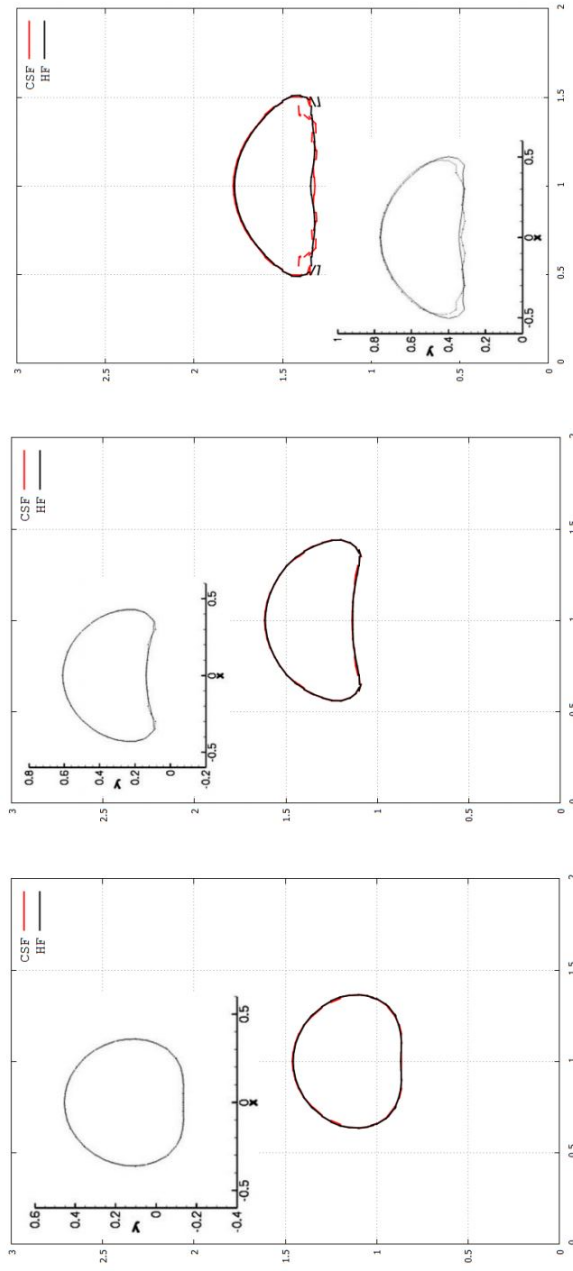


Figure 2.22: Rising bubble at time 0.2, 0.35 and 0.5 with  $\sigma = 728 \text{ dyne/cm}$ . The results of HF-CSF (black) method and traditional CSF (red) method are compared from current study with<sup>96</sup> Francoise et al. (Internal figures with axes).

## 2.4 Solution Methodology

The discretization of governing equations is performed using finite volume method with collocated grid arrangement. The temporal and convective terms are discretized using explicit two-stage second-order *Runge-Kutta*(RK) method<sup>97</sup> and *total variation diminishing*

ing (TVD) scheme<sup>98</sup> with *Superbee* limiter<sup>99</sup>, respectively. Semi-explicit solutions for the Navier-Stokes equations are obtained where the pressure is obtained implicitly whereas, velocity is calculated explicitly. The pressure Poisson equation is solved using *bi-conjugate gradient stabilized* (Bi-CGSTAB) method<sup>100</sup> having a diagonal pre-conditioner, which is provided with the convergence criterion of  $1 \times 10^{-6}$ . The Courant threshold is maintained at 0.1 by having the average time step as  $1 \times 10^{-5}$ .

To improve upon the computational speed of the code, parallel calculations were performed using OpenMP (open multi-processing) API (application processing interface) that supports the shared memory architecture. The parallel routine makes use of the multi-threading method where the master thread is forked into the worker threads which perform a discrete instruction individually and then join again to form a single master thread with all the results from instruction as shown in Fig. 2.23.

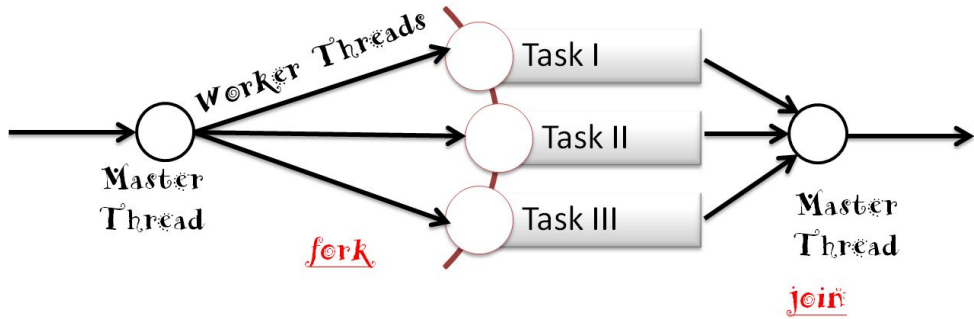


Figure 2.23: Fork and join method of parallelization.

The sample directive for the OpenMP parallelization can be written as follows,

```
#pragma omp parallel for collapse(2) schedule() private() reduction(:)
```

The **#pragma omp parallel** allows the compiler to locate the parallel part in the code, whereas **for** followed by it allows the compiler to know that the next *for loop* after the directive is to be made parallel. The directive **collapse()** combines the *for loops* into one single loop so that it can be divided into the worker threads as a single task using **schedule()**. The *scheduling* can be made **static** where manually the number of tasks are assigned to each worker or can be made **dynamic** where the compiler decides the number of workers needed based on the free *cache memory* near the location of a particular thread. The **private()** mode allows the data of each variable to be kept personal by each thread. If this data is to be communicated to other threads then directive changes to **default(shared)**. The threads in certain instructions need to carry out arithmetic operations by sharing a variable amongst themselves, and this operation is performed by the directive **reduction(:)**.

In the current study, the compiler was instructed to *collapse* the loops into one single loop, and then tasks were distributed using *schedule(static)* with an equal number of instructions to each thread (pressure correction solver loops are scheduled as *dynamic* to make use of the free *cache memory* near the idle thread). The parallel directives were supported by the *-O2* optimization flag during the simulations.

The load calculations of the sub-routines shown in Fig. 2.24 was calculated on *Intel Core (TM) i7-4770* with 4 cores working at a clock speed of 3.4 GHz. It was seen that the Momentum interpolation step, Krylov solver and source step are scaled better as the

number of cores increase, whereas the VOF, velocity update and file writing are not scaled well enough. This happens due to the fact that VOF is based on geometric reconstruction, which does not have any iterations to perform and file writing and updating require large data communications when the core number is incremented.

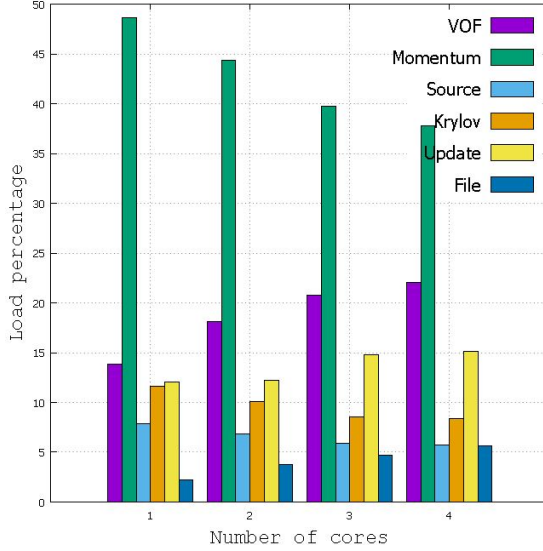


Figure 2.24: Load calculation of subroutines at increasing number of processors.

Also, speedup of the OpenMP code was tested on a 12 core Intel Xeon as shown in Fig. 2.25. As it is seen, the maximum speedup is 7 and hasn't saturated. Thus if more cores are used, the speedup might improve.

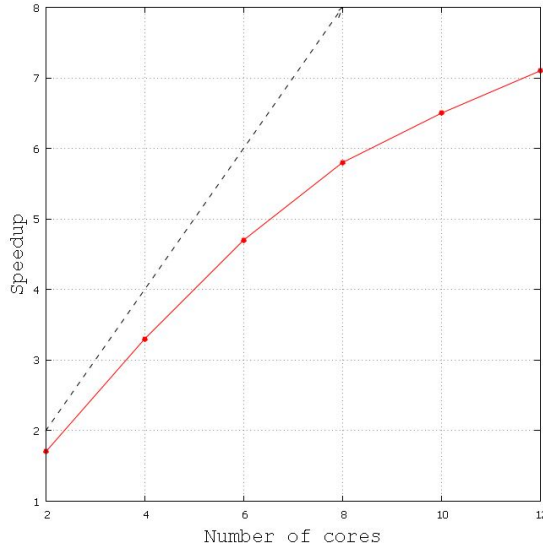


Figure 2.25: Speedup for OpenMP code.

The following algorithm demonstrates the solution methodology for the NS and VOF equations. Initially, the VOF equation is solved and is checked for its boundedness using the redistribution method. This volume fraction is used to calculate the mixed cell properties like density and viscosity. Finally, the NS equations are solved for the pressure and velocity field.

---

Summary of the two-phase flow solver algorithm

---

```

1: if (time > Required Duration) then return false else proceed
2:   procedure : VOF SOLVER
3:      $\phi^{n+1} \leftarrow$  Solve VOF Equation
4:     Redistribution  $\leftarrow$  Regulate overshoot and undershoot [ $\phi > 1.0$  or  $\phi < 0.0$ ]
5:      $\phi^n = \phi^{n+1} \leftarrow$  Update the previous time step value
6:   procedure : CALCULATE MIXED CELL FLUID PROPERTIES
7:      $\rho_{ij} = \phi_{ij} + (1 - \phi_{ij})\rho_{gas}/\rho_{liq}$ 
8:      $\mu_{ij} = \phi_{ij} + (1 - \phi_{ij})\mu_{gas}/\mu_{liq}$ 
9:   procedure : NAVIER-STOKES SOLVER
10:     $U^{(1)} = U^n + \Delta t F(U^n) \leftarrow$  Stage I
11:     $U^{n+1} = U^n + \frac{1}{2}\Delta t F(U^n) + \frac{1}{2}\Delta t F(U^{(1)}) \leftarrow$  Stage II
12:     $u^n = u^{n+1}; v^n = v^{n+1}; w^n = w^{n+1}; p^n = p^{n+1} \leftarrow$  Update Flow Variables
13:    time = time +  $\Delta t$ 

```

---

## 2.5 Discretization of Spatial and Temporal Terms

The governing equations are discretized using a finite volume method with the collocated grid arrangement where all the variables are stored at the centroid of each cell. The convective terms are discretized using the TVD (*total variation diminishing*) scheme with a *Superbee* limiter<sup>101</sup>. Thus, the interpolation of an advected scalar ( $\zeta$ ) at the cell face as shown in Fig. 2.26 is derived by Equation 2.23,

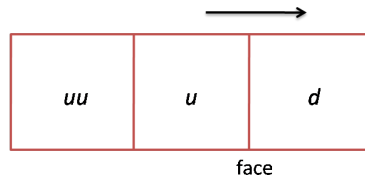


Figure 2.26: Cell nomenclature for TVD scheme

$$\zeta_{face} = \zeta_u + \frac{\psi(r)}{2}(\zeta_u - \zeta_d) \quad (2.23)$$

where,

$$\psi(r) = \max[0, \min(2r, 1), \min(r, 2)]$$

and

$$r = \frac{\zeta_u - \zeta_{uu}}{\zeta_d - \zeta_u}$$

such that the subscripts  $u$ ,  $uu$  and  $d$  represent the upwind, far-upwind and downwind cells for the cell face in consideration. In Equation 2.23, the flux limiter  $\psi(r)$  is a *Superbee* limiter given by<sup>101</sup> Roe which is a function of  $r$  that represents the ratio of successive scalar gradients.

A comparison of the TVD-Superbee<sup>1</sup> scheme with the other higher-order advection schemes is depicted in Fig. 2.27. This comparison is based on a typical single shock

---

<sup>1</sup>*Superbee* limiter is selected based on its better performance over the other limiters <sup>102;103</sup>.

problem<sup>104</sup>. This problem consists of a unit square two-dimensional domain which is supplied with a scalar of magnitude  $\zeta = 2$  and  $\zeta = 1$  from the bottom and left face respectively at a constant velocity, which results in a scalar shock at diagonal of the unit domain.

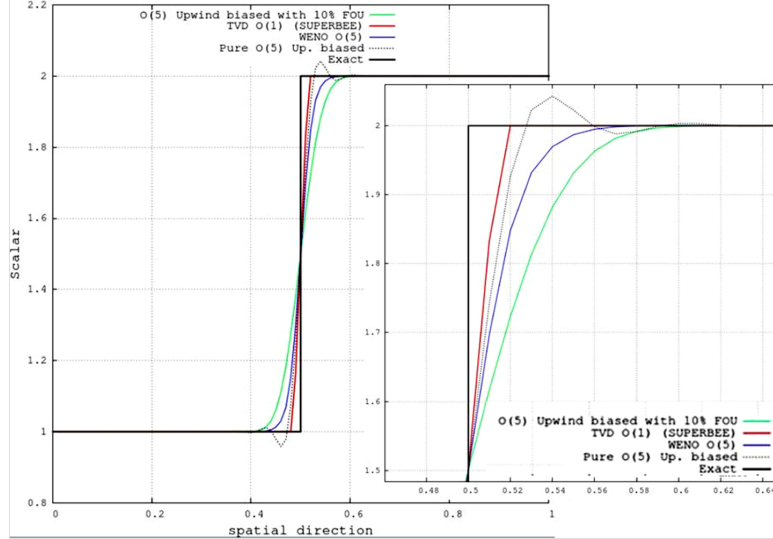


Figure 2.27: Comparison of advection schemes for a single shock problem.

It is observed that the pure form of upwind biased O(5) scheme creates oscillations near the discontinuity (*Gudonov's theorem*), thus it has to be blended with the lower order scheme like FOU (*first-order upwind*) to damp these unphysical oscillations. Still, the TVD scheme provides satisfactory results compared to the other schemes and, therefore, has been chosen here due to its compactness and ease of usage for non-uniform grids. Moreover, results for a complex one-dimensional shock problem are demonstrated in Fig 2.28 that compare the TVD-Superbee scheme with other higher order advection schemes. It can be observed that the WENO (*weighted essentially non-oscillatory*) scheme performs better than TVD when the multiple discontinuities are present, but it was also noticed during the test that computational time for WENO is greater than TVD scheme.

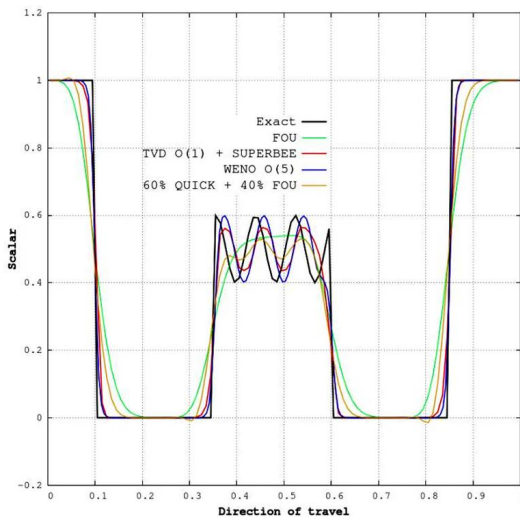


Figure 2.28: Comparison of advection schemes for a complex one-dimensional discontinuity

Moreover, a diffusion term in Equation 2.2 is spatially discretized in a direction  $s$  using the central difference formulation and is evaluated at a given face using Equation 2.24.

$$\begin{aligned} \frac{1}{\rho^* \text{Re}} \iint_{CS} \mu^* \frac{\partial \zeta}{\partial s} d\vec{A} &= \left[ \frac{\Delta d \phi_d + \Delta dd \phi_{dd}}{(\Delta d + \Delta p)(\Delta d + \Delta dd)} + \frac{\Delta uu \phi_{uu}}{(\Delta p + \Delta u)(\Delta u + \Delta uu)} \right] \sum_f \frac{A_f \mu_f^*}{\rho_f^* \text{Re}} \\ &- \left[ \frac{\Delta d \phi_d + \Delta p \phi_p}{(\Delta p + \Delta u)(\Delta p + \Delta d)} + \frac{\Delta p \phi_p}{(\Delta p + \Delta u)(\Delta p + \Delta d)} \right] \sum_f \frac{A_f \mu_f^*}{\rho_f^* \text{Re}} \end{aligned} \quad (2.24)$$

The temporal discretization is performed using the explicit two-stage second-order *Runge-Kutta* (RK2) method, which provides adequate simplicity and temporal accuracy for the problem in hand<sup>97</sup>. The average time-stepping  $\Delta t$  is maintained at  $1 \times 10^{-4}$  time/time step to satisfy the *Courant* ( $Co$ ) condition in the simulations, which is set to be  $Co \leq 0.1$ .

*This page intentionally left blank.*

---

## CHAPTER 3

---

### STABILITY OF AN OSCILLATING JET

The liquid jet when perturbed sinusoidally at the inlet will lead to instability under certain conditions. Understanding the causes and consequences of such a behaviour is surprisingly not deliberated explicitly in literature so far. This chapter aims towards analysing the spatial instability of such jets which is not yet reported in the literature. Therefore, present work attempts to improve upon the perceptive of spatially oscillating planar liquid jet in a quiescent gas and accurately predict the growth of its perturbed interface in space using an in-house Navier-Stokes based two phase solver as discussed in the previous chapter. This numerical model is validated against the experimental results provided by<sup>12</sup> Asare et al. for both thick and thin jet configurations. The grid convergence study is conducted as per *American Society of Mechanical Engineers* (ASME) standards<sup>105</sup> for the problem in hand, which achieves third order accurate solution. Special attention is also paid towards depicting the influence of Re, We, Fr, and the inlet velocity profile on the growth of perturbations.

A two-dimensional domain under consideration is depicted in Fig 3.1. An oscillating water sheet with an infinite width and thickness of  $2h_0$  is injected into the quiescent air at a velocity  $V_{in}$ . The domain size in terms of half sheet thickness  $h_0$  is  $80h_0 \times 180h_0$ . The liquid sheet injection section is stationed at the centre of the top face of the domain through which the liquid descends in the negative  $y$  direction.

The inlet velocity of the liquid sheet  $V_{in}$  has two components in space, one of which enables the jet to attain the inlet velocity and the other serves as a sinusoidal perturbation to the jet which later evolves as an instability. The  $u^*$  and  $v^*$  components of the inlet velocity are expressed in Equation 3.1,

$$\begin{aligned} u^* &= A_0 \sin(2\pi St \times t^*) \\ v^* &= V_{inlet} \end{aligned} \tag{3.1}$$

where  $St$  represents the *Strouhal number* describing oscillation frequency ( $f$ ) in the jet with an initial perturbation amplitude  $A_0$  and is given as  $St = fU/h_0$ . The velocity profile at the inlet is parabolic in nature to emulate the developed flow through the nozzle. A region around the inlet is treated as a wall, whereas the side faces are dealt as the free slip boundaries. The bottom face of the computational domain is prescribed with the pressure outlet condition as depicted in Fig 3.1. The physical properties for air and water are based on the normal temperature of  $20^\circ C$  and  $101.325 \text{ kPa}$  pressure. Thus, these values are shown in Table 3.1 with the non-dimensional parameters used in the simulation.

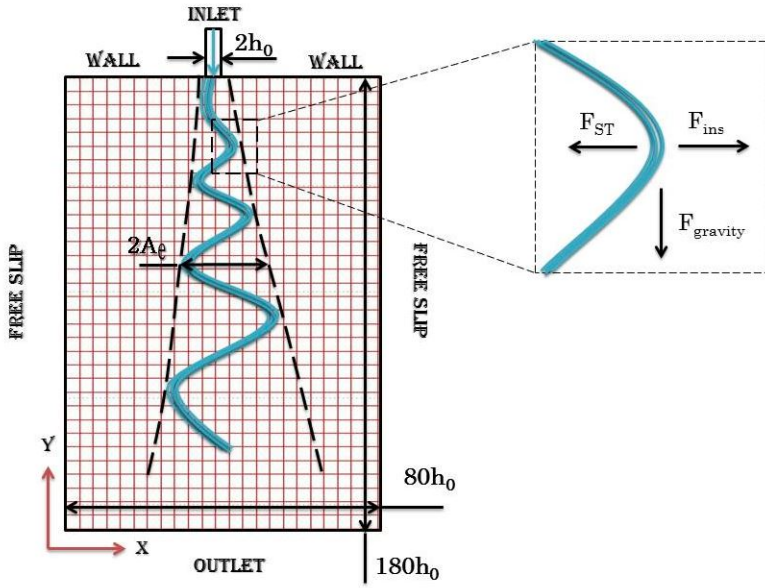


Figure 3.1: Computational domain and boundary conditions for the spatially oscillating jet instability.

Table 3.1: Physical Properties and Non-Dimensional Parameters.

Water Density	$\rho_l = 998 \text{ kg/m}^3$
Water Viscosity	$\mu_l = 1.002 \times 10^{-3} \text{ kg/ms}$
Air Density	$\rho_g = 1.188 \text{ kg/m}^3$
Air Viscosity	$\mu_g = 1.81 \times 10^{-5} \text{ kg/ms}$
Surface Tension Coefficient	$\sigma = 0.07275 \text{ kg/s}^2$
Sheet Thickness	$2h_0 = 0.00788 \text{ m}$
Perturbation Amplitude	$A_0 = 0.09$
Injection velocity	$V_{inlet} = 2.05 \text{ m/s}$
Reynolds Number( $Re$ )	$Re = \rho_l U h_0 / \mu_l$
Weber Number( $We$ )	$We = \rho_l U^2 h_0 / \sigma$
Froude Number( $Fr$ )	$Fr = U / \sqrt{gh_0}$

The grid refinement study is performed to examine the spatial convergence of the solution. It is carried out on three uniform grids having constant refinement ratio of 1.3 in each direction with the finest grid bearing the resolution of  $522 \times 910$  in  $x$  and  $y$  direction respectively. This grid refinement study is based on the generalized *Richardson extrapolation theory* where the grid independence is reached when the spatial discretization error asymptotically approaches to zero<sup>106</sup>. Fig 3.2 shows the effect of grid refinement on absolute vorticity, mean axial velocity and mean volume fraction. It can be observed from Fig 3.2 that though finest grid solutions are not yet completely grid independent but they lie in the asymptotic region of convergence.

The order of grid convergence is evaluated based on Equation 3.2, where the absolute value  $|p|$  is necessary to ensure extrapolation towards grid size tending to zero<sup>107</sup>.

$$p = \left| \ln \left( \frac{|w_z|_{coarse} - |w_z|_{medium}}{|w_z|_{medium} - |w_z|_{fine}} \right) / \ln(r) \right| \quad (3.2)$$

Here,  $r$  is the refinement ratio and the absolute vorticity  $|w_z|$  is evaluated at  $t^* = 70$ ,

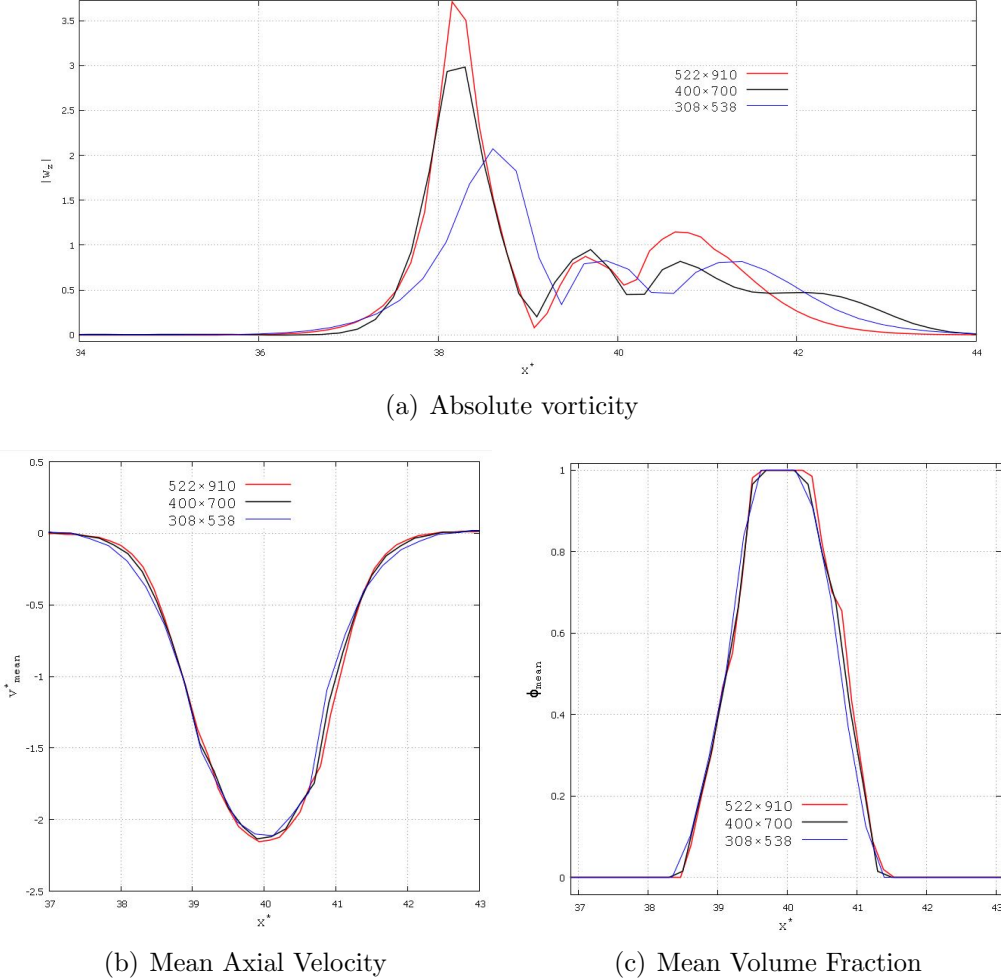


Figure 3.2: Grid resolution study for the three different grids with refinement ratio of 1.3 in both directions at  $y^*=10$  and  $t^*=70$ .

$y^* = 10$  and  $x^* = 38.5$ . The solution was found to be third order accurate ( $|p| \sim 3$ ). Further, the *grid convergence index* (GCI) is calculated between coarse and medium grid ( $GCI_{CM}$ ) and again between medium and fine grid ( $GCI_{MF}$ ) using Equation 3.3,

$$GCI = \frac{F_s |e|}{r^p - 1} \quad (3.3)$$

where, factor of safety  $F_s$  is considered to be 1.25 as the three grid levels are used in the study<sup>108</sup> and  $|e|$  is an error estimate between the two consecutive grid levels. Hence, it was found that the  $GCI_{CM}$  and  $GCI_{MF}$  are 1.39% and 0.65% respectively denoting spatial convergence of the solution. Fig 3.3 shows the use of *Richardson extrapolation* to estimate higher order solution at grid size tending to zero from the lower order values. Also, the solutions for different grids were checked for their nature of convergence by evaluating the ratio  $GCI_{CM}/(GCI_{MF}r^p)$ , where it is found to be 0.987, confirming the asymptotic convergence. As the  $GCI_{MF}$  value shows very small variation of 0.65% between the fine and medium grid, the current simulations were performed using grid resolution of  $400 \times 700$  to avoid the computational expense.

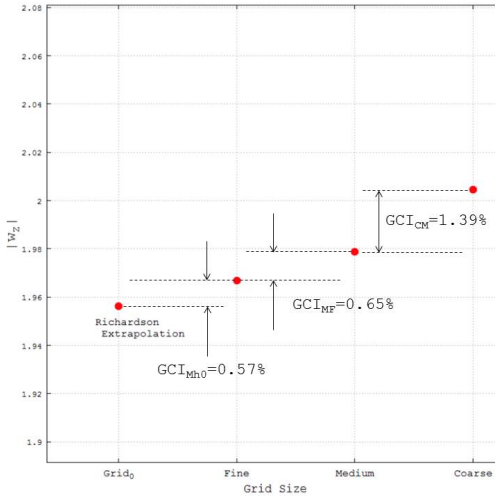


Figure 3.3: Richardson extrapolation of  $|w_z|$  at grid size tending to zero.

A growth of an initial perturbation is compared with the experimental data of<sup>12</sup> Asare et al. as these experiments are more relevant to the current study. These experiments were performed on a set of two nozzle configurations namely *Nozzle A* and *Nozzle B* as given in Table 3.2. Two configurations were chosen such that both the thick ( $kh_0 > 0.25$ ) and thin ( $kh_0 \ll 1$ ) sheet approximations are validated. Thus, in the first simulation (*S01*) *Nozzle A* configuration (thin sheet) was chosen with the forcing frequency and amplitude of 70Hz and 0.2mm respectively, whereas in the second simulation (*S02*) *Nozzle B* configuration (thick sheet) with the forcing frequency and amplitude of 20Hz and 1.0mm respectively was chosen.

Table 3.2: Nozzle configuration and inlet parameters used by<sup>12</sup> Asare.

Nozzle	Sheet thickness (mm)	Sheet width (mm)	Jet Velocity (m/s)	Forcing frequency (Hz)	Forcing amplitude (mm)
Nozzle A	1.59	78	5.0	30, 50, 70, 100	0.08, 0.1, 0.2, 0.3
Nozzle B	7.90	75	2.05	20, 30, 50, 70	0.80, 1.0, 1.6

The growth rate of the sinuous perturbation is also compared with results provided by the temporal *linear stability analysis*, where a liquid sheet of thickness  $2h_0$  and inlet velocity  $U_0$  is perturbed by  $\eta = A_e(y)\cos(ky - \omega t)$  such that,  $k$  and  $\omega$  denote the wave number and complex angular frequency. The initial conditions for  $\eta$  is set to  $\eta(y, 0) = 0$ . Therefore, dispersion relation is as shown by Equation 3.4. It can be obtained by perturbing the inviscid flow equations by  $(u, v, p) = (U, V, P)(x)e^{(iky+\omega t)}$ .

$$\rho_l(\omega + ikV_{in})^2 \tanh(kh_0) + \rho_g\omega^2 + \sigma k^3 = 0 \quad (3.4)$$

Here,  $U, V$  and  $P$  denote the amplitude of disturbance for the respective variable. Moreover, the envelope ( $A_e$ ) formed due to the growth of amplitude is estimated as,

$$A_e(y) = A_0 (e^{\omega_i y/U_0} - e^{-\omega_i y/U_0}) \quad (3.5)$$

The simulation *S01* is performed with the domain of size  $80 \times 360$  having the grid resolution of  $400 \times 1400$ , whereas *S02* is performed based on the details provided earlier in Fig. 3.1. Thus, the values of non-dimensional parameters used in Equation 2.2 for *S01* and *S02* are provided in Table 3.3. Here, the growth rate in terms of jet envelope is studied by measuring the non-dimensional growth ( $A_e/A_0$ ), where  $A_e$  denotes the spatial growth of a perturbation at particular fall distance. The measurement routine of a growth  $A_e$  is performed at the leading edge from the mean position of the jet at a particular instant in time as demonstrated in the Fig. 3.1. During this measurement the fluid lumps at the interface are excluded as they can cause ambiguity in results. The normalised measurements of growth in amplitude ( $A_e/A_0$ ) are compared with the growth envelope obtained using temporal linear stability analysis.

Table 3.3: The non-dimensional parameters used for the simulations *S01* and *S02*.

	Grid Size (Domain Size)	$Re$	$We$	$Fr$	$St$
S01	$400 \times 1400$ ( $80 \times 360$ )	887.64	10.95	11.35	0.347
S02	$400 \times 700$ ( $80 \times 180$ )	4426.96	54.72	5.0864	0.495

Fig 3.4 and 3.5 demonstrate the development and growth of a disturbance in the jet during *S01* simulations. The numerical results near the nozzle agree well with the linear theory as compared to the experiments, which is due to the fact that<sup>12</sup> Asare et al. was unable to measure the amplitude correctly in this region. The results away from the nozzle deviate from the linear theory due to the non-linear effects in the growth of a disturbance. Also, the numerical results are found to be within 5% of the experimental values.

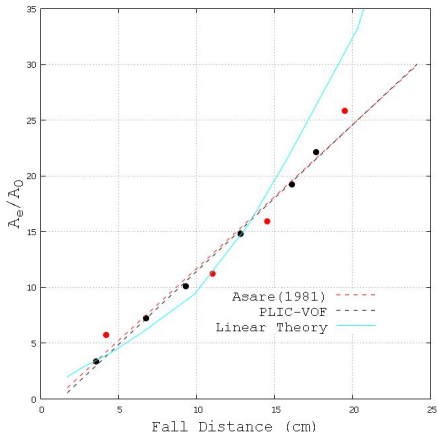


Figure 3.4: Comparison of the oscillation amplitude with experiments<sup>12</sup> for *S01* simulation.

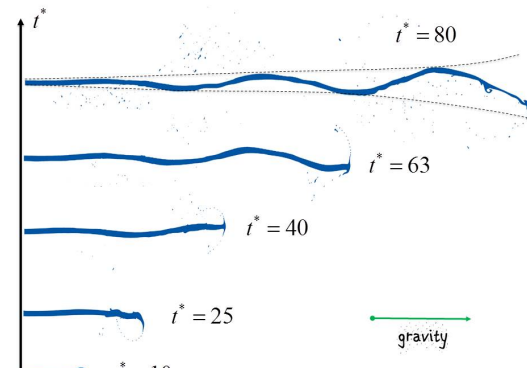


Figure 3.5: Jet development with *S01* configuration.

Fig 3.6 and 3.7 show the development and growth of a disturbance in the jet for simulations using *S02* configuration. The similar trend is observed here as the numerical predictions compare well with the linear theory near the inlet and start to deviate as the jet descends in the domain. A growth rate predicted by the numerical simulations lie within 6% of the experimental growth rate.

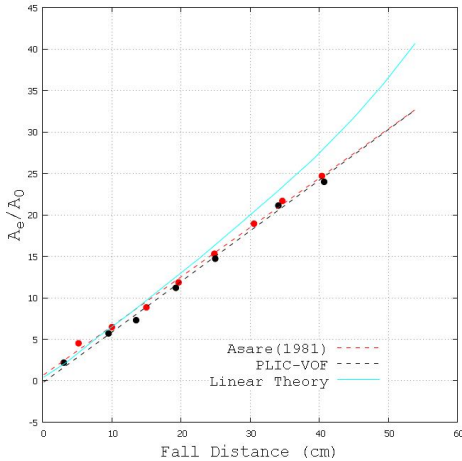


Figure 3.6: Comparison of the oscillation amplitude with experiments<sup>12</sup> for *S02* simulation.

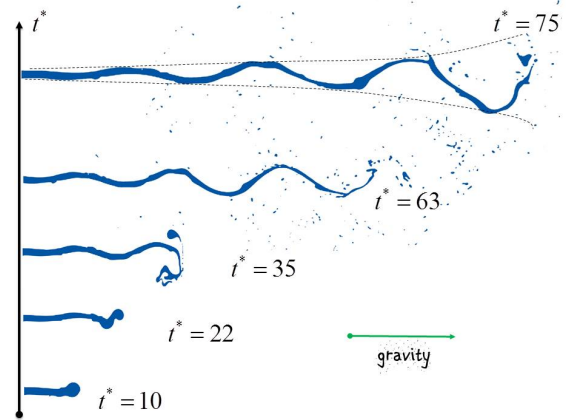


Figure 3.7: Jet development with *S02* configuration.

The slight under predictions shown by the numerical results are owing to the dissipation error shown by advection scheme which dampen the amplitude of a perturbation. The results can conclude that the linear stability analysis can predict the initial development of the jet well, but away from an inlet region non-linearities deviate the prediction which are evident from the transition of sinusoidal disturbance to steeper peaks downstream of the flow.

### 3.1 Development of an Oscillating Liquid Jet

The planar jet injected into the quiescent air with the sinusoidal perturbation provided by the transverse velocity is shown in Fig. 3.8. It is observed from the Fig. 3.8(a) that perturbations augment spatially while the jet descends into the domain. Thus, it becomes important to investigate the reasons for such an instability and the effect such jet behaviour has on the surrounding fluid.

An increase in the amplitude of perturbation as observed in Fig. 3.8(a) is caused due to the pressure difference created across the jet. Pressure variation graph inscribed in Fig 3.8(b) shows that pressure near the leading edge is lower as compared to pressure at trailing edge. This pressure difference is manifested due to the vortical structure developed in the air due to the shear layer formation near the jet interface. This low pressure region near the crest will exert the force on the jet towards the centre of vortex as explained further in this section. Hence, as the amplitude increases, this pressure difference augments further downstream to cause instability in these jet.

Fig. 3.9 shows vorticity and vortex development in the jet as it spatially oscillates in the domain. As jet enters the quiescent air, a mushroom shaped front is formed through the transverse liquid spread which is caused by its impact on the stagnant air. This transverse spreading rolls up due to the baroclinic torque ( $(\nabla\rho \times \nabla p)/\rho^2$ ) occurring due to the *Rayleigh Taylor* instability<sup>109 110</sup>. This misalignment between density and pressure gradients manifest an upward plume creating the head vortices at the jet front similar to a steady straight jet. This front dynamics is followed by the formation of individual vortices at the leading edge of a deflection which are caused by the dominant shear layer near an interface. It is depicted that the vortices near a jet front are influenced by the strong vorticity of the head vortices leading to their merger. On the other hand, *Rayleigh*

*Taylor* instability continue to form the head vortices during each cycle of the maximum deflection, leaving behind vortices that cause the local re circulations<sup>1</sup>. It is also observed that the vorticity field across the jet is asymmetric due to the squeezing and stretching of the shear layer in the leading and trailing edges respectively and this agrees with the results presented by<sup>1</sup> Ostermann et al.. This asymmetry makes the velocity gradient at the leading side to exceed that of the trailing side and augments the pressure difference causing the instability in a jet.

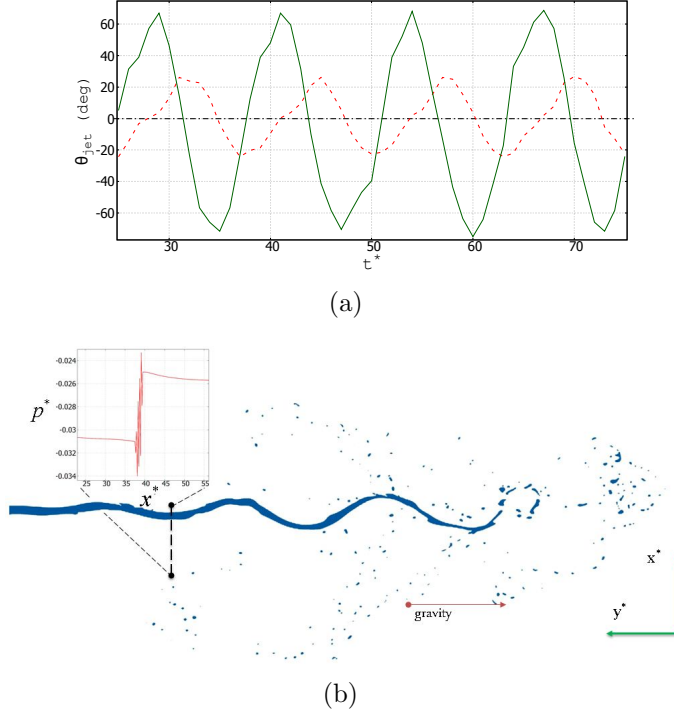


Figure 3.8: Deflection of the jet ( $\theta_{jet}$ ) measured at  $y^* = 170$  (dashed red) and  $y^* = 150$  (solid green) with data retrieved at  $\Delta t = 1$  (a) and snapshot of developing jet and its disintegration (b).

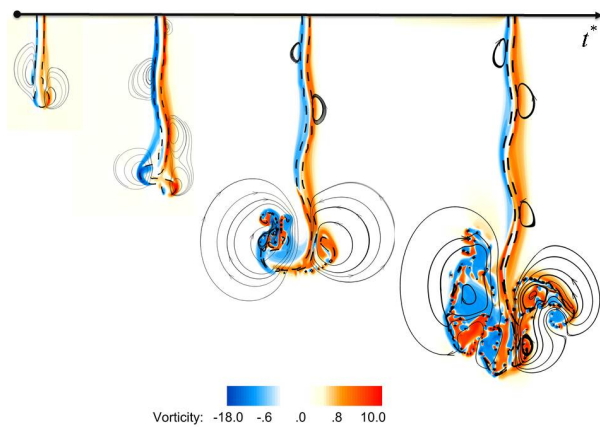


Figure 3.9: Vorticity and streamlines (solid lines) in the jet (dashed lines) at  $t^* = 13, 27, 37$  and  $50$  (from left).

An interpretation of the results in terms of *enstrophy* becomes important as visual-

ization of mere vorticity in the domain will have both positive and negative components, making it difficult to gauge the magnitude of rotation. Thus, the *enstrophy transport equation* (ETE)<sup>111</sup> as given by Equation 3.6 is used in the present study to measure the intensity of rotation or viscous energy dissipation in the fluid. Here, the vortex stretching term ( $w \cdot \nabla v$ ) reduces to zero, due to the two dimensional nature of the equations and a body force such as gravity is assumed to be conservative.

$$\frac{Dw_z^2}{Dt^*} = \frac{\mu^*}{\rho^* \text{Re}} \nabla^2 w_z^2 - \frac{2\mu^*}{\text{Re} \rho^*} (\nabla w_z)^2 + \frac{w_z}{\rho^* \text{We}} (\nabla \times F_{ST}) \quad (3.6)$$

The first term on the right hand side of Equation 3.6 indicates the spatial spreading of the *enstrophy* due to viscous diffusion, whereas as the second and third term indicate the *enstrophy dissipation* and surface tension force respectively. As  $\|w_z\|_2^2 \sim \left\| \nabla \vec{V} \right\|_2^2$ , we can co-relate the loss of *kinetic energy* ( $\frac{1}{2} \rho \left\| \vec{V} \right\|_2^2$ ) due to viscous dissipation in the fluid with *enstrophy* creation or destruction according to the sign of right hand side (R.H.S.) of Equation 3.6<sup>111</sup>. Thus, it is observed from Fig. 3.10 that the magnitude of these contours at the interface is more in the near-field and depletes around the interface at downstream. This suggests that the kinetic energy loss is higher near the inlet whereas away from the inlet positive R.H.S. values are only observed at the distinct peaks of jet; suggesting that the jet loses energy only at the peak region. Also, at the downstream, atomization induces local rotation in air which is evident from the higher contour values.

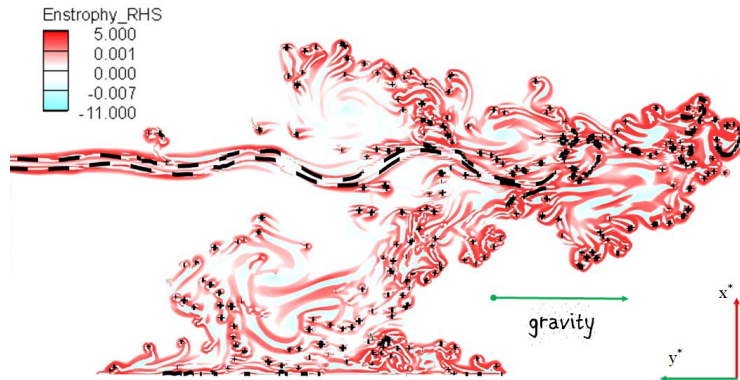


Figure 3.10: R.H.S. of Equation 3.6 with jet(dashed lines) at  $t^* = 60$ .

Fig. 3.11 demonstrates the contribution of different R.H.S. terms at  $y^* = 150$  when the jet is approaching its maximum deflection (right of the inlet) at  $t^* = 40$  and then changes direction (towards left). It can be seen that the diffusion term ( $\frac{\mu^*}{\rho^* \text{Re}} \nabla^2 w_z^2$ ) is dominant cause of *enstrophy* creation or destruction as compared to the dissipation term. Also, it is found that the surface tension force has negligible effect on the *enstrophy* and thus can be termed as a conservative force in this particular region. As jet is deflected towards the right of a mean position, as in Fig. 3.11(a) and 3.11(b), the *enstrophy* value depletes at the trailing edge (left) and become minimum at the point of maximum deflection as observed in Fig 3.11(b). At the leading edge (right) *enstrophy* value increases and becomes maximum at  $t^* = 40$ , resulting in the formation of rotational region in the fluid near a peak. As the jet starts to deflect in an opposite direction (towards left), the equilibrium position is attained at  $t^* = 42$  where both edges display almost equal amount of rotation and then, the *enstrophy* starts to generate at the leading edge (left).

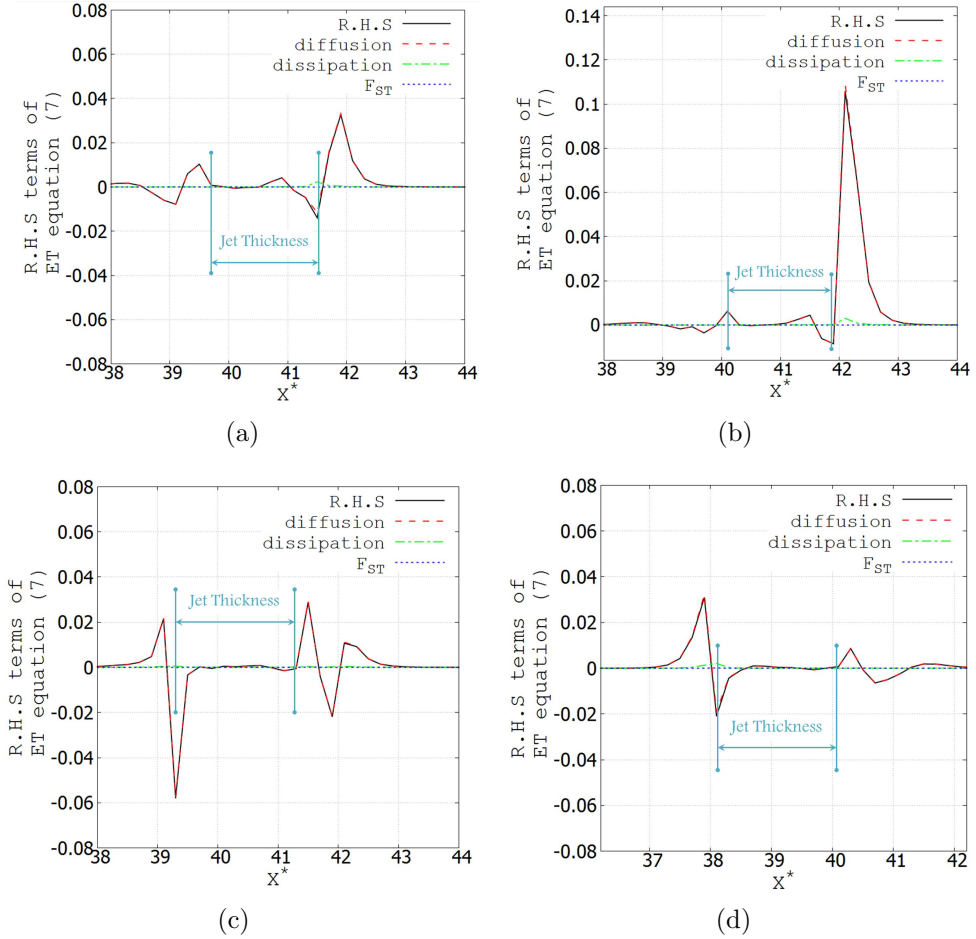


Figure 3.11: R.H.S. of ETE 3.6 at time  $t^* = 38$  (a),  $t^* = 40$  (b),  $t^* = 42$  (c) and  $t^* = 44$  (d).

To understand the influence of these vortical structures on the jet, it is necessary to visualize the lamb vector( $I$ ) and its divergence ( $\nabla \cdot I$ ) as the lamb vector exist only in the region of non-zero velocity and is non-parallel to vorticity( $w_z$ ) making it more localized than the vorticity<sup>112 113</sup>. Moreover they are also capable to demonstrate the dynamical changes in the domain in the form of kinetic energy changes<sup>112</sup>. Thus, vortex force( $F_{vort}$ ) and divergence of lamb vector are evaluated using Equation 3.7 and 3.8 respectively.

$$F_{vort} = \rho^*(u \times \omega) = \rho^* v \omega_z \hat{i} - \rho^* u \omega_z \hat{j} \quad (3.7)$$

$$\nabla \cdot I = (v \frac{\partial \omega}{\partial y} - \omega \omega) \hat{i} - (u \frac{\partial \omega}{\partial x} - \omega \omega) \hat{j} \quad (3.8)$$

Here,  $F_{vort}$  in Equation 3.7 is the product of density, velocity and vorticity with unit vectors  $i$  and  $j$ . Whereas, right hand side of Equation 3.8 has the flexion product as the first term and *enstrophy* as the second. Fig. 3.12 shows contours for  $\nabla \cdot I$  focused at a typical peak of an oscillating jet. The  $\nabla \cdot I$  (hydrodynamic charge density) value at the peak changes sign, which signifies a distinct dynamical change<sup>112</sup>. Thus, positive valued contour next to the leading edge denotes the unwinding of a vortex where the angular momentum of the vortex is converted into linear momentum. This energy is imparted onto the jet to translate its peak towards the vortex. This results in the jet being pulled according to

the lamb vectors and vortex force lines, towards the centre of a vortex where the positive value signifies higher rotational capacity. Also, it is observed that the primary vortex gives rise to secondary small scale vortices that are deflected in the peripheral direction due to centrifugal force, which may have an impact on the flow field. The negative contour values of  $\nabla \cdot I$  suggest that these vortices have store kinetic energy and can impart momentum onto the surrounding fluid.

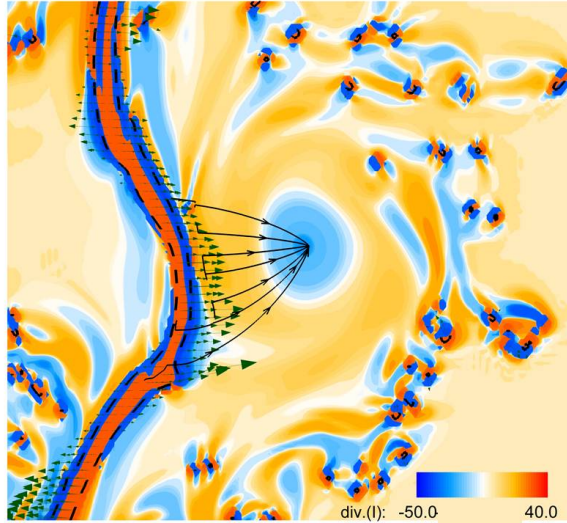


Figure 3.12: Contours for  $\nabla \cdot I$  and lamb vectors( $I$ ) (green arrows with 0.5 scaling) around a peak in the jet(dashed lines) with vortex force lines (black solid curves).

The falling oscillating jet accelerates as its axial velocity increases when it penetrates the domain as a result of gravitational forces. Thus, as observed from Fig. 3.13, to conserve the mass of a fluid, the jet thickness reduces proportional to an increase in the jet axial velocity. This decrease in the jet thickness leads to primary breakup of the jet beyond which the axial velocity increases exponentially at the downstream end.

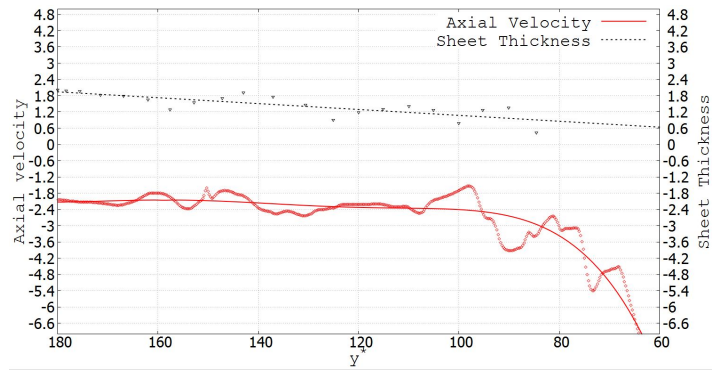


Figure 3.13: Non-dimensional axial velocity ( $v^*$ ) (red markers) and jet thickness (black markers) ( $2h_0$ ) at  $x^* = 40$  and  $t^* = 60$  where the jet descends into the negative  $y^*$  direction of the domain. Solid and dotted lines denote the best fit curves for the respective markers.

The breakup mechanism observed in two dimensional scenario is as depicted in Fig. 3.14. The deflected jet experiences flow separation at the leading edge causing disturbance at the interface which grows based on the *Kelvin Helmholtz* (KH) instability to

form droplets. Also, another mechanism of droplet formation is observed where the upward plumes caused by the *Rayleigh Taylor* (RT) instability disintegrates as depicted in Fig. 3.14(b). Thus, KH and RT instabilities are responsible for the disintegration of an interface in the oscillating jet, which also comply with the observations made by<sup>24</sup> Schmidt et al.. Apart from these instabilities capillary action at the peaks also cause sheet breakup as explained in Sec. 3.4.

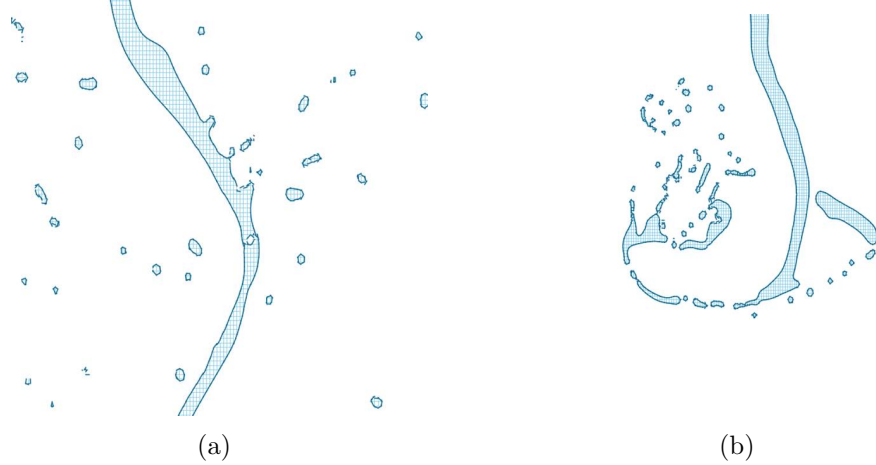


Figure 3.14: Fluid polygons showing jet interface disintegration mechanism by *Kelvin-Helmholtz* instability (a) and *Rayleigh-Taylor* instability (b).

## 3.2 Effect of Reynolds Number

In order to study the effect of viscosity on the jet development and the energy interaction between the two fluids, four different Reynolds number of 500, 2500, 4400 and 6500 have been considered. The values for other non-dimensional parameters are  $We = 54.72$ ,  $Fr = 5.08$ ,  $St = 0.495$  and the velocity profile at the inlet is parabolic.

Fig. 3.15(a) demonstrates the non-dimensional growth rates ( $A_e/A_0$ ) for increasing Reynolds number ( $Re$ ). It can be definitively observed that the viscosity acts as a stabilizing force and dampens the perturbation amplitude, which is also supported by the study of<sup>114 115</sup>. A growth rate observed for  $Re = 6500$  agrees satisfactorily with the inviscid linear theory and thus, such jet can be viewed as an inviscid jet showing the maximum growth of a disturbance. It is also depicted from Fig. 3.15(b) that the jet in the near-field remains sinusoidal and experiences non-linear growth away from it<sup>11 114</sup>. Such a behaviour is more prominent at higher Reynolds numbers.

Fig. 3.16 shows the *mean enstrophy* (over 60 time periods) of the jet at its maximum deflection for various  $Re$  values. The  $Re = 6500$  results demonstrate the highest *enstrophy* at the leading edge, which proves the existence of strong rotational intensity that results in the growth of a disturbance. The viscous diffusion of the *enstrophy* is observed at lower  $Re$  values and this diffusion depletes as  $Re$  value increases; which becomes evident from the steeper peaks in the *enstrophy* values.

Fig. 3.17 represent the *mean transverse vortex force* ( $- < \rho v^* w_z >$ ) acting on the jet formed due to the rotational field near the leading edge of the jet. It is observed that, as the Reynolds number increases the pull felt by the jet towards an eye of the vortex becomes stronger.

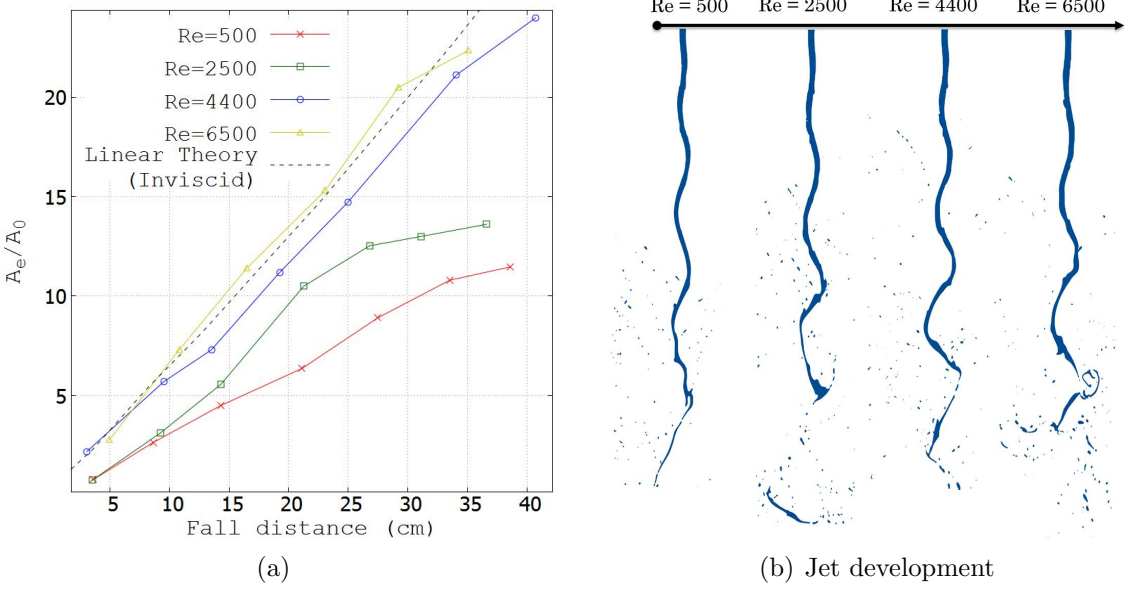


Figure 3.15: Effect of Reynolds number ( $Re$ ) on the growth rate ( $A_e/A_0$ ) of the initial perturbation( $A_0$ ) (a) and jet development (b) at  $t^* = 68$ .

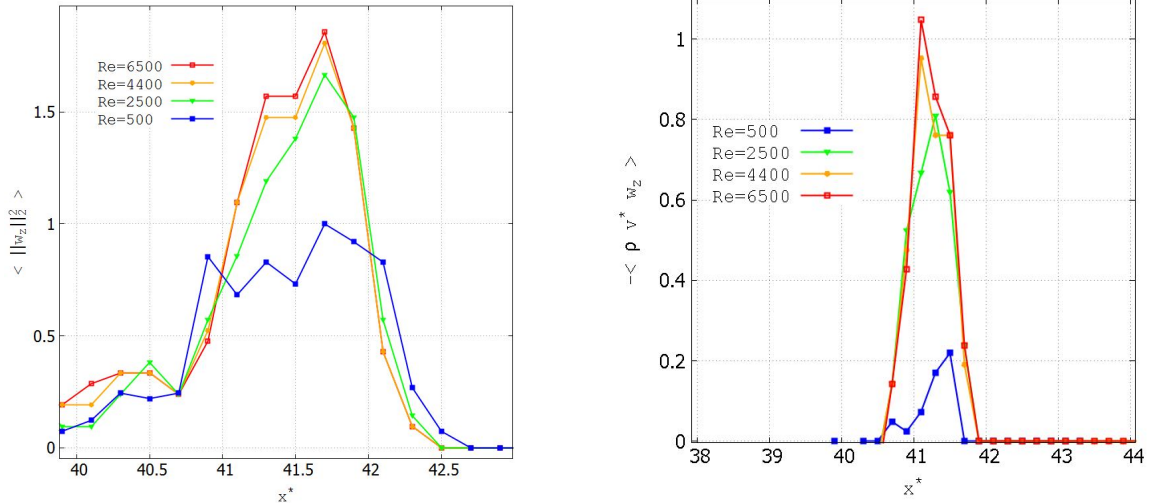


Figure 3.16: Mean Enstrophy ( $\langle \|w\|_2^2 \rangle$ ) of the jet at  $y^* = 150$  with increasing  $Re$ .

Figure 3.17: Mean transverse vortex force felt by the jet at the leading edge at  $y^* = 150$  with increasing  $Re$ .

### 3.3 Effect of Weber number

The effect of surface tension on the growth of a perturbation and its topology is studied for Weber numbers 10, 55, 100 and 200 in this section. The values for other non-dimensional parameters are  $Re = 4426.96$ ,  $Fr = 5.08$ ,  $St = 0.495$  and the velocity profile at the inlet is parabolic. Fig 3.18(a) demonstrates the growth of an initial perturbation ( $A_0$ ) at different Weber numbers. It can be observed that, surface tension acts as a stabilizing force for the given perturbations in an oscillating jet and these observations are consistent with <sup>114 115</sup>. This increase in amplitude of oscillation ( $A_e/A_0$ ) at higher  $We$  is a result of the increased relative velocity caused by the inertia force at the interface. Fig. 3.18(b) demonstrates the volume fractions of the liquid jet with increasing values of Weber number. The increased

interaction between air and water cause local non-linearities which deform the sheet more with an increase in  $We$ . This non-linearity (visible as steeper peaks in the oscillations) induces breakup of the jet as observed by<sup>12</sup> Asare et al..

Weber number also influences the planar jet thickness, where Fig. 3.19(a) demonstrates the thinning of liquid jet with an increase in  $We$ . The thinning of liquid jet at higher Weber numbers is due to an increase in the axial velocity of jet. This is confirmed by Fig. 3.19(b) that shows the axial velocity distribution for each  $We$  at  $t^* = 74$  along the jet centre. Another observation that can be made from Fig. 3.18(b) is the increased amount of atomization that has resulted from the large surface energy at higher  $We$ <sup>114</sup>.

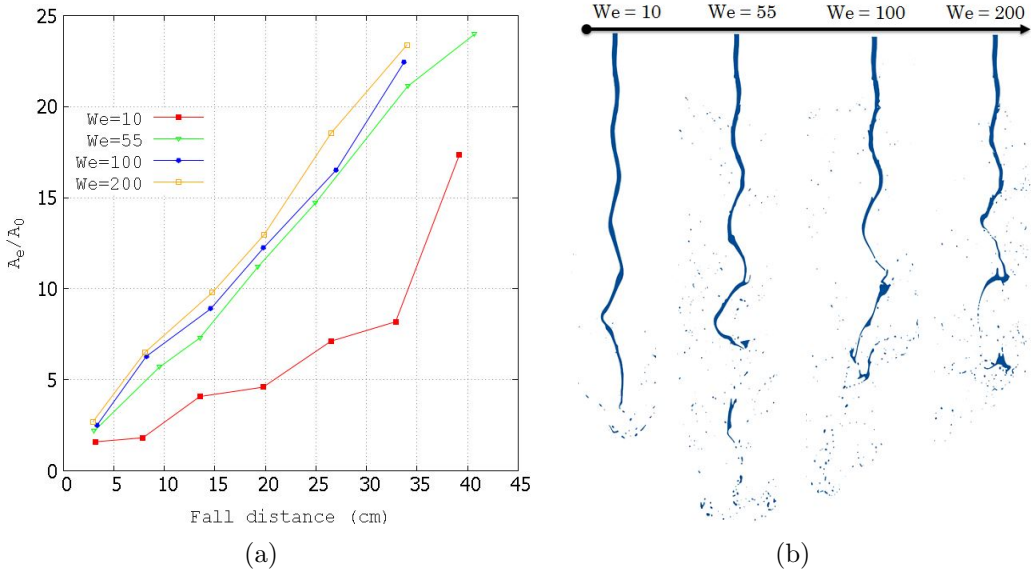


Figure 3.18: Effect of Weber number ( $We$ ) on the growth rate ( $A_e/A_0$ ) of the initial perturbation( $A_0$ ) (a) and jet development (b) at  $t^* = 74$ .

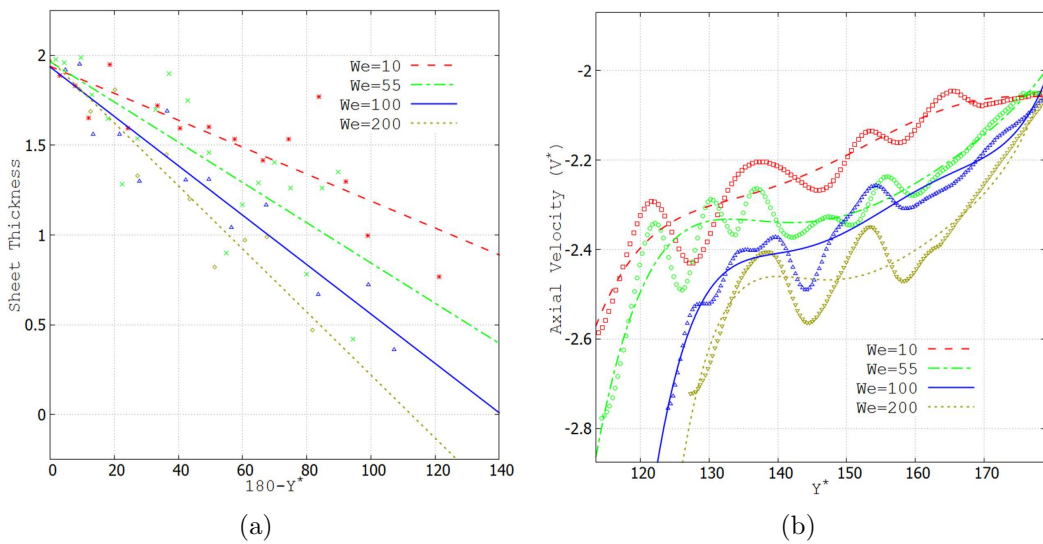


Figure 3.19: Effect of Weber number on the jet thickness in negative  $y^*$  direction (a) and jet axial velocity (b).

### 3.4 Effect of Froude number

The behaviour of an oscillating jet is studied for the different Froude numbers of 5, 15, 25 and 35. The values for other non-dimensional parameters are  $Re = 4426.96$ ,  $We = 54.72$ ,  $St = 0.495$  and the velocity profile at the inlet is parabolic. Thus, the effect of gravity on the propagation, topology and stability of the jet is analysed.

Fig. 3.20(a) demonstrates the trajectory of oscillating jet for various Froude numbers. The propagation of jet is significantly influenced at higher  $Fr$  values. As acceleration due to gravity reduces, the only force driving the jet is an inertia force and thus, decrease in the phase velocity of the disturbance with increase in  $Fr$  is observed. Thus, Fig. 3.20(b) also exhibits reduced jet thickness at  $Fr = 5$  which becomes obvious with increased axial velocity.

The amplitudes depicted in Fig 3.20(a) suggest that as  $Fr$  increases, disturbance reaches its maximum growth followed by its damping. This maximum amplitude is reached by the virtue of inertia forces which are dominant initially as  $Fr$  increases but, as  $Fr$  increases further the surface tension forces become dominant due to higher curvature values at the peaks. As surface tension forces tend to stabilize these perturbations, an amplitude is observed to get damped at higher Froude numbers.

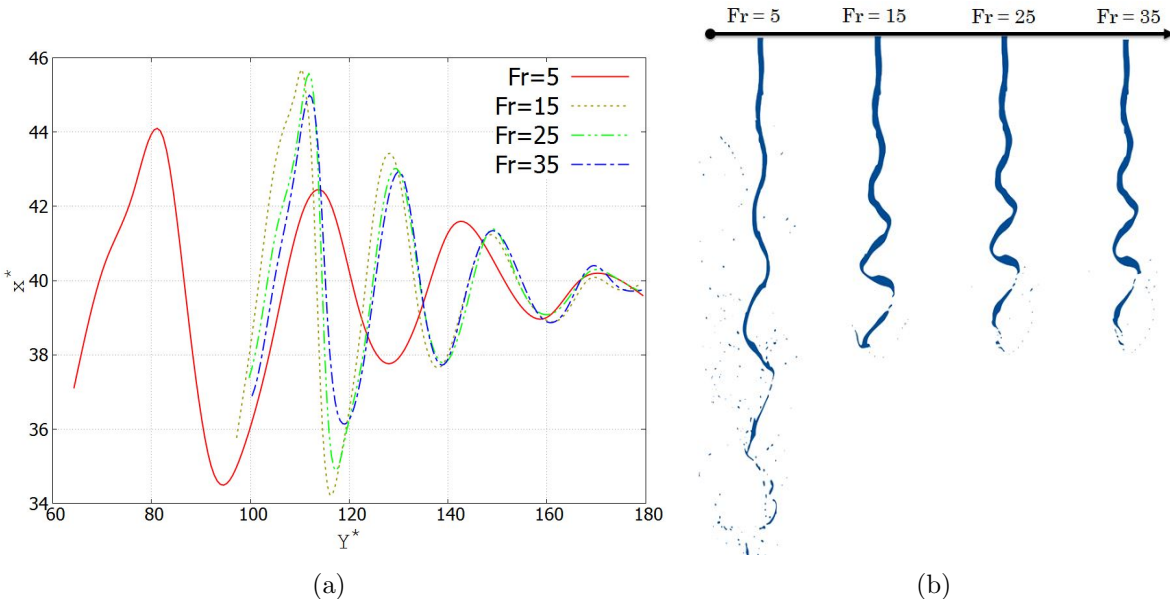


Figure 3.20: Effect of Froude ( $Fr$ ) number on jet deflection traced along the half jet width (a) and its topology using volume fractions (b).

Non-linear growth of the perturbation is more dominant away from the nozzle which creates more steeper deflection in the jet. Fig. 3.21 shows mechanism through which the non-linear growth leads to the primary breakup of the jet. Stations 1 and 2 in Fig. 3.21(a) show the peaks having smaller radius of curvature. Hence, the fluid from stations 1 and 2 is pushed out into the neighbouring regions creating a bulge of fluid owing to higher pressure at these stations. The curvature augments even more due to the amplification in amplitude of perturbation and this thins out the bridge between two bulges and eventually the jet breaks creating a satellite droplet as shown in Fig. 3.21(d). Hence, apart from the KH and RT instabilities, role of capillary breakup mechanism is also observed during present simulations.

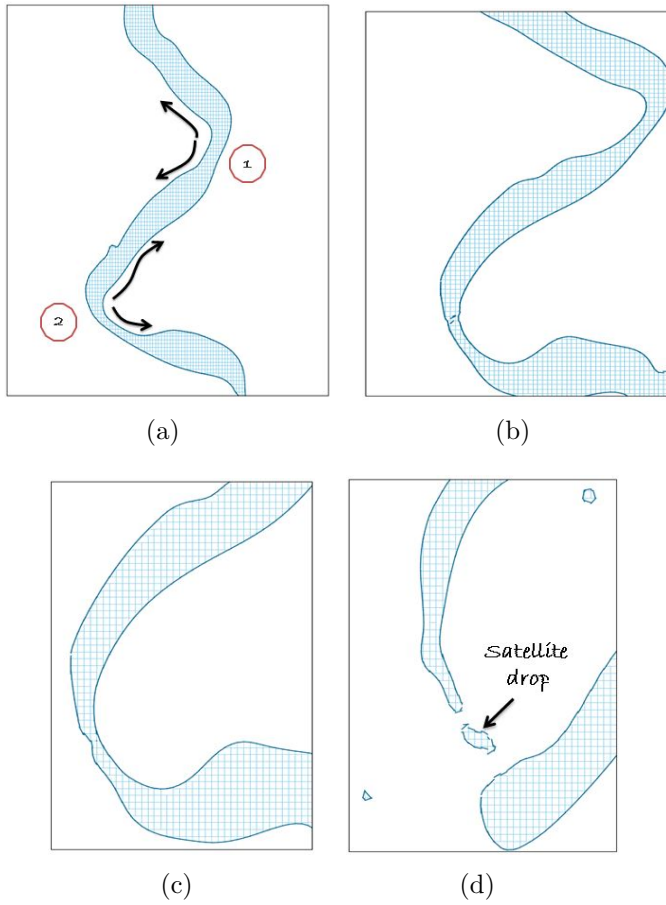


Figure 3.21: Fluid polygons displaying the mechanism of primary capillary breakup in an oscillating jet at  $t^* = 68$  (a),  $t^* = 70$  (b),  $t^* = 74$  (c) and  $t^* = 80$  (d).

### 3.5 Effect of Inlet-Velocity Profile

Effect of uniform inlet velocity profile on the stability of a jet is studied in this section and results are compared with the jet emanating with the parabolic inlet velocity profile. The values for non-dimensional parameters used for this study are  $Re = 4426.96$ ,  $We = 54.72$ ,  $Fr = 5.08$  and  $St = 0.495$ . Fig. 3.22(a) demonstrates the deflection of jet for uniform and parabolic inlet velocity profile. The jet destabilizes if the inlet velocity profile is made flatter and grows in amplitude. This growth arises due to the higher relative velocity between the two fluids at the interface as depicted in Fig 3.23 where the velocity profile shifts upwards due to greater deflection of jet as in case of uniform profile. This causes the aerodynamic instability to grow at the interface.

As a jet travels downstream, the axial velocity of the jet increases causing increased interaction between the two fluids. This energy exchange across the interface causes interfacial disturbances of different wavelengths to occur and interact. These non-linearities are observed to arrive a lot earlier in the case of uniform profile as compared to the parabolic nature of an inlet velocity, which augment even more at the downstream to cause early breakup in the jet.

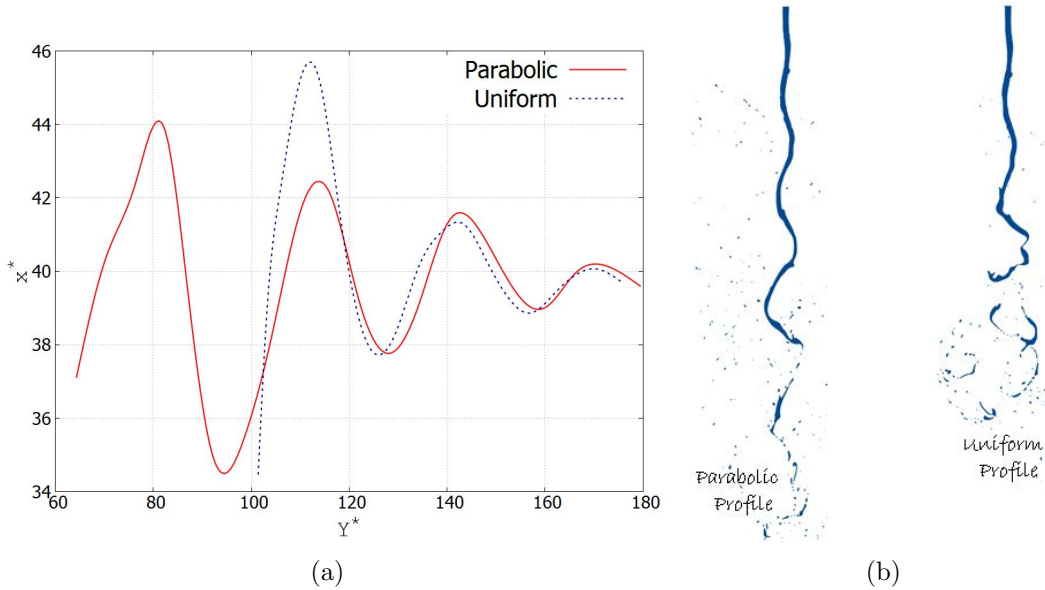


Figure 3.22: Effect of inlet velocity profile on jet deflection traced along the half jet width (a) and its topology using volume fractions (b).

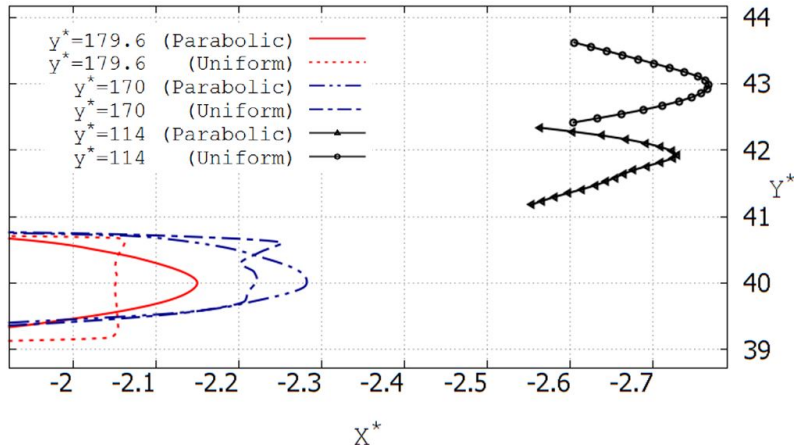


Figure 3.23: Axial velocity profiles as jet propagates in negative  $y^*$  direction.

## 3.6 Closure

Present study reveals that the instability in an oscillating jet is caused due to a pull felt by it toward the vortical structure formed at the leading edge. These vortical structures are affected by the repetitive formation of head vortices at the jet front due to the RT instability. These head vortices that are convected at a greater velocity as compared to leading edge vortices produce local re-circulations in the flow field. RT and KH instabilities developed due to these vortical structures eventually cause primary breakup of the jet. The present analysis demonstrated the role of capillary instability in jet breakup in association with these instabilities.

Parametric analysis demonstrates that viscosity and surface tension have a stabilizing effect on the oscillating planar jets. On the other hand, as the Froude number is increased, it is found that the growth of perturbation reaches the maximum due to inertia, and then,

the jet starts to stabilize as the influence of surface tension increases. The jet is also found to get destabilized when inlet velocity profile is uniform. A parabolic inlet velocity profile on the contrary stabilizes it. This happens due to the higher relative velocity between the two fluids at the interface provided by the uniform velocity profile.

*This page intentionally left blank.*

---

## CHAPTER 4

---

# COHERENT STRUCTURES IN AN OSCILLATING JET

A coherent structure is a connected turbulent fluid mass with a phase correlated vorticity over the extent of entire structure<sup>25</sup>. These structures are responsible for the mass and momentum exchange in the shear layer. The complex flow can be decomposed into some kind of relatively simpler coherent structures. These structures often provide valuable information about the physical behaviour of the system. Such studies can lead to significant insights into the complicated flow field formed by the jets subjected to spatial or temporal oscillations.

The momentum transport and entrainment of a developing plane jet is dominated by coherent structures. Percipience about the formation, evolution and interaction of these coherent structures for oscillating planar jet is still not clearly depicted in literature. In the present chapter, numerical investigations are reported for analysing spatially oscillating planar jet by solving Navier-Stokes equations coupled with volume of fluid (VOF) method to track air-water interface. Coherent structures in the flow for Reynolds numbers ( $Re$ ) 4500 and 500 are identified using *Q-criterion*. Furthermore, the dominant flow structures are identified and analysed using *proper orthogonal decomposition* (POD) and *dynamic mode decomposition* (DMD).

The computational domain of size  $80h_0 \times 110h_0 \times 80h_0$  is considered for the present study and is depicted in Fig. 4.1. The oscillating water jet of thickness  $2h_0$  and width  $w_0$  emanates through centre of the top face of the domain into a quiescent air. The jet has an inlet velocity  $V_{in}$  as it falls in the  $-y$  direction under the influence of gravity. The vertical faces of the domain are treated with the free slip boundary condition, whereas the bottom face is a typical pressure outlet for the fluids. Top face contains the jet inlet at the centre while rest of the face is considered as wall. The inlet velocity condition for the jet needs two components in  $x$  and  $y$  directions as  $u^*$  and  $v^*$  respectively to produce oscillations. The  $y$  – *component* of velocity ( $v^*$ ) has parabolic profile with mean velocity being  $V_{in}$  to emulate the fully developed velocity profile. The  $x$  – *component* of the velocity ( $u^*$ ) provides the sinuous perturbations to the jet which at the downstream end develops into instability. Thus, the inlet velocity vector has transverse ( $u^*$ ) and axial ( $v^*$ )

velocity components which can be given as

$$\begin{aligned} u^* &= A_0 \sin(2\pi St \cdot t^*) \\ v^* &= V_{in} \\ w^* &= 0 \end{aligned} \quad (4.1)$$

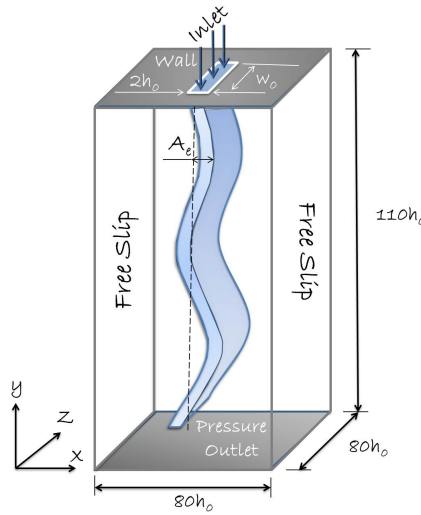


Figure 4.1: Computational domain and boundary conditions for the oscillating jet.

such that,  $St$  denotes *Strouhal number* describing perturbation frequency ( $f$ ) of jet which is defined as  $St = fh_0/U$ . The sinusoidal perturbations are provided with a constant initial amplitude  $A_0$ . The physical properties of air and water are defined at normal temperature and pressure. The inlet parameters and flow conditions used are as shown in Table 4.1.

Table 4.1: Inlet parameters and flow conditions used for the present study

Re	We	Fr	$h_0$ (m)	$w_0$ (m)	$V_{in}$ (m/s)	St	$A_0$
4426.96	54.72	5.08	0.00395	0.075	2.05	0.495	0.2531

The numerical uncertainty associated with the present study is quantified using the *Grid Convergence Index* (GCI)<sup>107</sup>. GCI is based on the generalized Richardson's extrapolation where, discrete solutions at different grid levels are compared. The present study makes use of  $160 \times 210 \times 160$ (Coarse),  $240 \times 315 \times 240$  (Medium) and  $360 \times 470 \times 360$  (Fine) as grid resolutions to perform grid refinement study with refinement ratio ( $r$ ) being 1.5. The effect of this grid refinement on the absolute vorticity field and axial velocity of jet is demonstrated Fig. 4.2. It can be observed from Fig. 4.2 that solution for the refined grid lies within the asymptotic convergence region as it is demonstrated ahead. Here, jet deflection( $A_e$ ) is chosen as a parameter to demonstrate grid convergence as it is known in its exact form through experiments<sup>12</sup>. Thus, the jet deflection and development for above stated grid resolutions is depicted in Fig. 4.3.

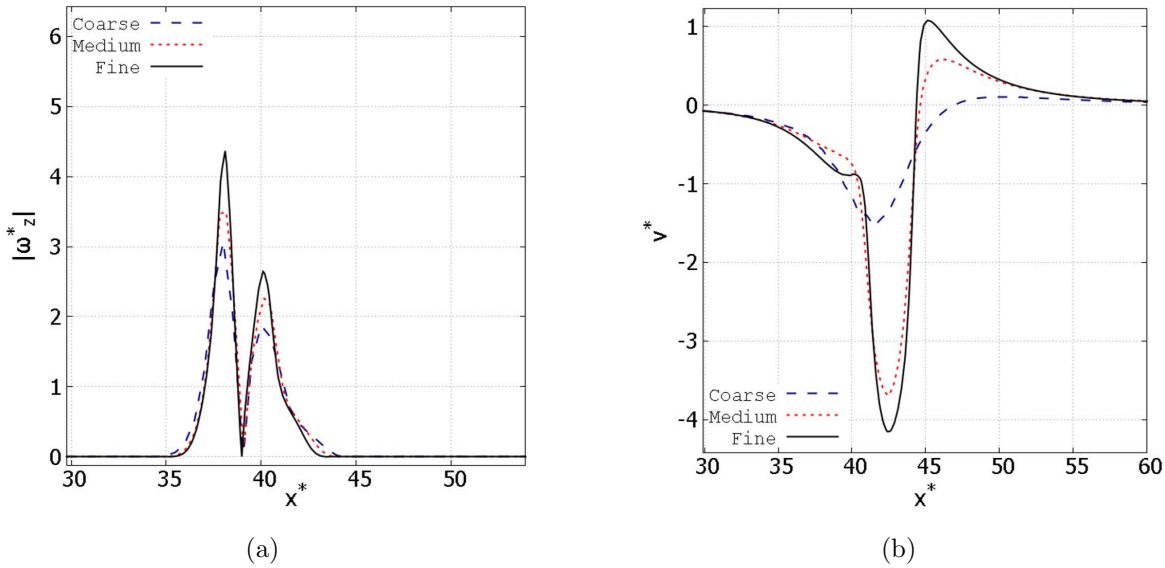


Figure 4.2: Effect of grid refinement on a) absolute vorticity ( $\omega_z^*$ ) and b) axial velocity ( $v^*$ ) during  $t^* = 10.95$  at  $y^* = 40$  and  $z^* = 40$  along  $x^*$ .

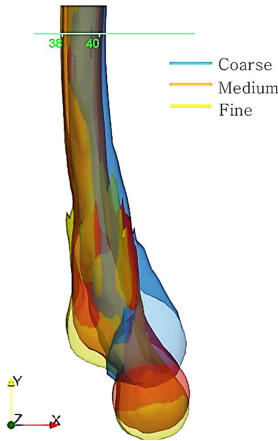


Figure 4.3: Jet deflection for three grid levels at  $t^* = 11$  with jet iso-surfaces coloured with yellow, red and blue represent Fine, Medium and Coarse mesh resolutions.

The order of grid convergence ( $p$ )<sup>107</sup> is evaluated based on Equation 4.2 and  $A_e$  is measured at  $y^* = 40$ ,  $z^* = 40$  and  $t^* = 11$ . Therefore, order of grid convergence is found to be second order accurate ( $|p| \sim 2.259$ ).

$$p = \left| \ln \left( \frac{A_{e\text{coarse}} - A_{e\text{medium}}}{A_{e\text{medium}} - A_{e\text{fine}}} \right) / \ln(r) \right| \quad (4.2)$$

The GCI values between *Coarse* and *Medium* ( $GCI_{CM}$ ) as well as between *Medium* and *Fine* ( $GCI_{MF}$ ) are evaluated using Equation 4.3.

$$GCI = \frac{F_s |e|}{r^p - 1} \quad (4.3)$$

Here,  $F_s$  and  $|e|$  denote factor of safety ( $F_s = 1.25$ ) and relative error between grid solutions respectively. The values of  $GCI_{CM}$  and  $GCI_{MF}$  are found to be 1.08% and 0.43%

respectively demonstrating spatial convergence. Moreover, the Richardson's extrapolation is performed to obtain the deflection value when grid tends to zero using the Equation 4.4.

$$A_e|_R = A_{fine} + \frac{A_{fine} - A_{medium}}{r^p - 1} \quad (4.4)$$

Hence, the value  $A_e|_R$  is utilized to evaluate the  $GCI_{RF}$  between extrapolated solution and the finest grid solution, which was found to be 0.3%. This value is close to the previous  $GCI_{MF}$  value of 0.43%. Furthermore, the asymptotic convergence is also asserted by the ratio  $GCI_{CM}/(GCI_{MF} * r^p)$  that rounds off to unity<sup>106</sup>. Hence, the present simulations are carried out at the finest grid resolution of  $360 \times 470 \times 360$ .

The present numerical model based on *SAISH-VOF* method is validated against the envelope measurements( $A_e$ ) performed by<sup>12</sup> Asare et al. for the *Nozzle B* configuration as mentioned in Table 4.2.

Table 4.2: Nozzle configuration and inlet parameters used by<sup>12</sup> Asare et al.

Nozzle	Sheet thickness (mm)	Sheet width (mm)	Jet Velocity (m/s)	Forcing frequency (Hz)	Forcing amplitude (mm)
Nozzle B	7.90	75	2.05	20	1.0

The numerical simulations are performed using the grid resolution of  $360 \times 470 \times 360$  with the physical properties and non-dimensional number as mentioned in Chapter 3. The comparison of the non-dimensional growth rate ( $A_e/A_0$ ) obtained in the present study with experimental measurements<sup>12</sup> and the linear theory prediction<sup>12</sup> are presented in Fig. 4.4. The amplitude of oscillation ( $A_e$ ) at different  $y^*$  locations is measured with reference to the initial perturbation ( $A_0$ ) at a particular instant in time when at least one oscillation cycle has exited the outflow boundary. The present results show good agreement with the experiments with maximum error found to be 6.8%. This deviation in the results are present at the near field measurements which<sup>12</sup> Asare et al. attributed to the inaccurate amplitude measurement during experimentation.

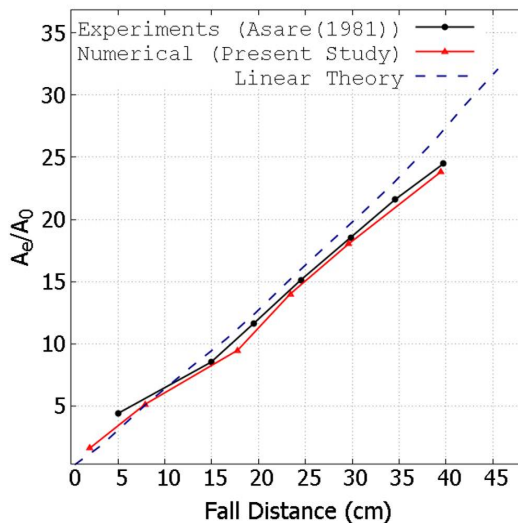


Figure 4.4: Comparison of present simulations with<sup>12</sup> Asare et al. and linear stability theory.

The near field predictions are in agreement with the linear theory (linear theory over-predicts at downstream end) as assumption of linearity in the governing equations is preserved until air interactions become dominant as demonstrated in Chapter 3. This characteristic nature of the oscillating jet is demonstrated in Fig. 4.5 where the sinuous perturbation become sharp downstream due to aerodynamic interactions and lead to jet disintegration. The numerical simulations for the present study are carried for a non-dimensional time of  $t^* = 64$ . This allows the jet to exit from the outlet boundary twice and provides almost 32 period of oscillations. A vortex the present study is identified using *Q-criterion*, where the vorticity tensor is greater than strain-rate tensor i.e.  $Q > 0$ . An additional condition of minimum pressure at vortex core also must be satisfied by the plotted vortex through *Q-criterion*. Moreover, the work of <sup>21</sup> Desjardins et al. and <sup>116</sup> Khosronejad et al. has already demonstrated the ability of *Q-criterion* to depict vortex structures in gas-liquid flows.

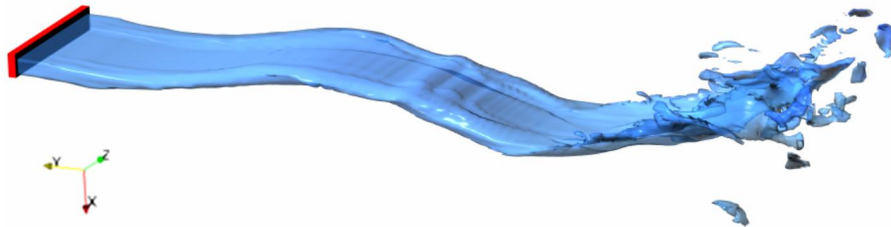


Figure 4.5: Developing oscillating planar liquid jet and its downstream disintegration at  $t^* = 27.23$  (volume rendered).

## 4.1 Head Vortex Structures

Oscillating jets exhibit a peculiar behaviour at the jet front in the form of its head vortices. Unlike steady jets, oscillating jet does not form a symmetric mushroom shaped upward plume based on *Rayleigh-Taylor*(RT) instability. Initially oscillations cause the formation of bottom lobe as a result of a baroclinic torque ( $(\nabla\rho \times \nabla p)/\rho^2$ ) acting over it as observed in Fig. 4.6(a)( $t^* = 8.56$ ). This bottom lobe is replaced by another jet front (top lobe) that is exposed to the air in stream-wise direction as observed in Fig. 4.6(a)( $t^* = 12.44$ ). This front is also acted upon by the baroclinic torque resulting in the formation of second lobe. Therefore, existence of two front lobes create two distinct head vortex rings at the front with some distance apart. Moreover, the preceding lobe undergoes RT instability and forms an upward plume. This gives rise to an asymmetric RT breakup as analysed in Chapter 3. Here, iso-surfaces in Fig. 4.6(a) are representing results obtained at  $Re = 4500$  as there is no significant difference in surface topology as compared to  $Re = 500$  apart from the oscillation amplitudes for given time units. Furthermore, Fig. 4.6(b) and 4.6(c) demonstrates the development of coherent structures defined at  $Q = 0.05$  for  $Re = 4500$  and  $Re = 500$  respectively. It is depicted that the leading head vortex slows down and overturn itself due to the upward motion of the leading lobe as a result of RT instability. During this process both the head vortices lose their ring-like structure forming large *top hairpin vortex* (THV) and *bottom hairpin vortex* (BHV). Each of the hairpin vortex has its legs formed by their respective *stream-wise trailing vortices* (SV) typically formed by the pressure gradient across the jet. These stream-wise vortices (SV) at the downstream are observed to interact and have significant impact on the flow field as discussed in

the further sections. Apart from this, a vortex aligned next to the jet deflection/peak is formed due to increase in the enstrophy of air (refer Chapter 3). These mechanisms through which the head vortices undergo transformation into hairpin vortices remain identical for both the  $Re$  values and thus, viscous forces are having negligible effect over them. The only difference in the result between the two  $Re$  values here is the intensity of rotation or enstrophy ( $\omega_z^2$ ) of BHV and THV as depicted in Fig. 4.7. It is observed that the viscous dissipation results in loss of kinetic energy for  $Re = 500$  that is evident from lower enstrophy values.

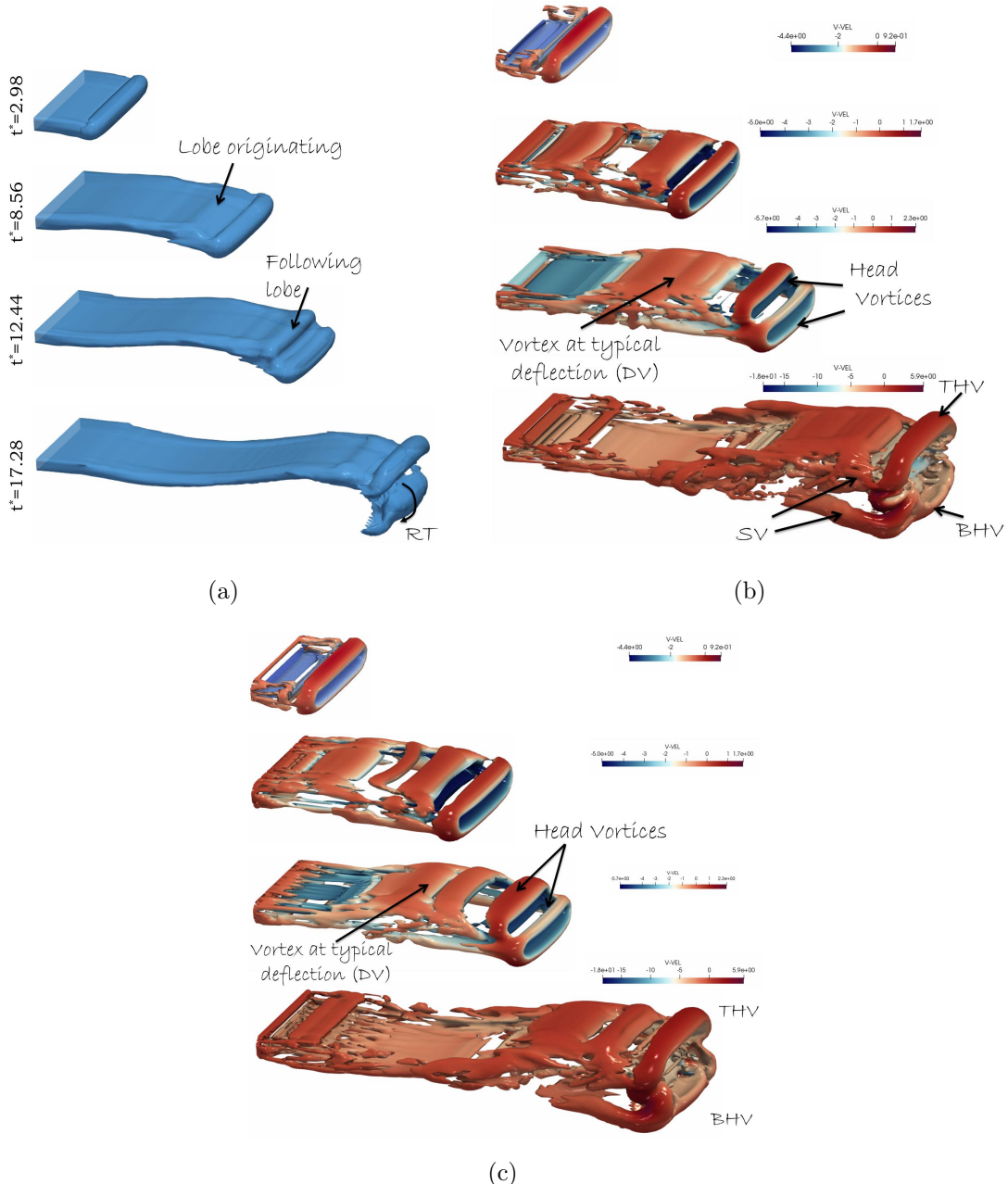


Figure 4.6: The development of head vortices shown by iso-surfaces of a) volume fraction ( $\phi = 0.5$  at  $Re = 4500$ ) and vortex structures ( $Q = 0.05$ ) for b)  $Re = 4500$  and c)  $Re = 500$  with contours denoting magnitude of stream-wise velocity  $v^*$ .

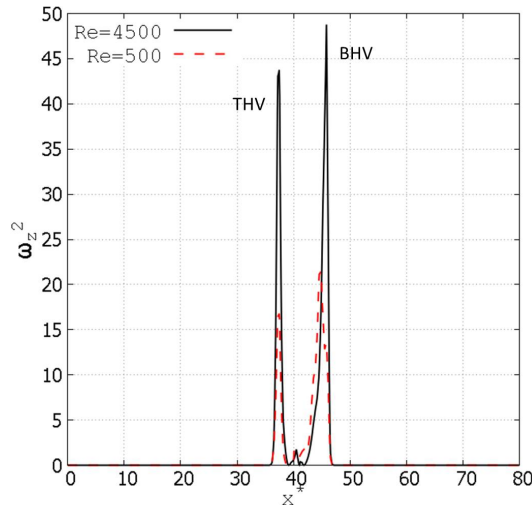


Figure 4.7: Comparison between the enstrophy values of THV and BHV for the jet at  $Re = 4500$  and  $Re = 500$  along  $x$ -axis.

The formation of two large hairpin vortices leads to complex vortex structure interaction at the jet front for  $Re = 4500$ . Fig. 4.8 demonstrates the schematic explaining formation of hairpin vortices over the plane perpendicular to stream-wise direction. The overturning of preceding lobe forms a span-wise vortex roller between the BHV and THV. This span-wise vortex is convected in the stream-wise direction at greater magnitude as compared to the jet front. Such stream-wise movement of the roller vortex causes the fluid between BHV and THV to be expelled out; leading to the formation of hairpin vortices on the plane normal to the stream-wise direction. This formation occurs at  $t^* = 18.20$  at the jet front, as shown in Fig. 4.9(a) which represents the results for  $Re = 4500$ . It is depicted from Fig. 4.9(a) that hairpin vortices originate from the sides of vortex roller and expel the fluid at greater velocity from the base as shown by the velocity vectors (red arrows with 0.5 scaling) as compared to hairpin head. On the other hand, for  $Re = 500$  the energy of vortex roller is damped by the viscous forces and doesn't retain its cylindrical shape. This is evident from Fig. 4.10(a) where velocity profile for  $Re = 500$  presents the influence of viscous damping which leads to lower fluid expulsion velocity from the front and thereby hampering the formation of hairpin vortices as demonstrated in Fig. 4.10(b).

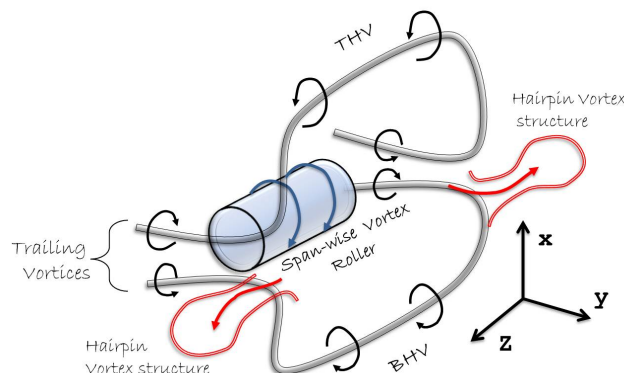


Figure 4.8: Schematic of the hairpin vortex formation at the jet front over the plane perpendicular to the stream-wise direction.

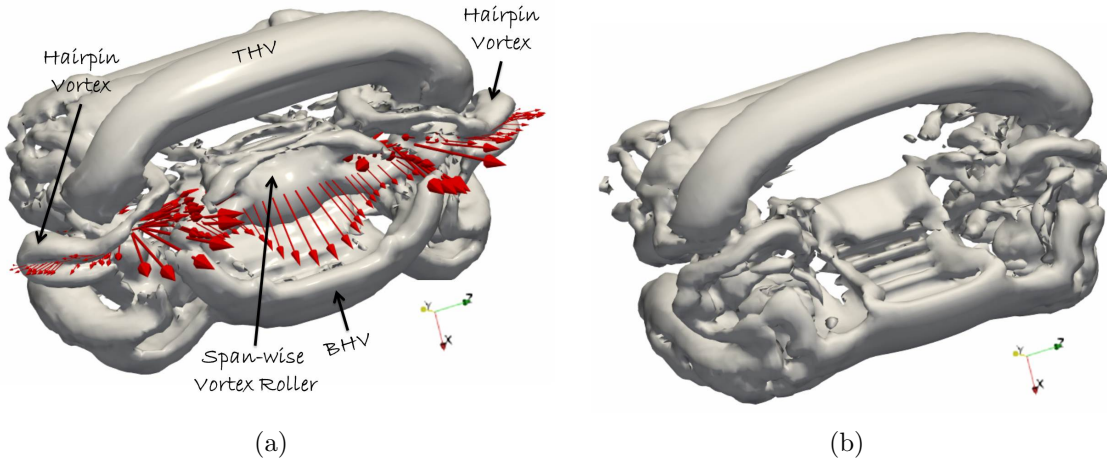


Figure 4.9: Q-criterion iso-surfaces ( $Q = 0.05$ ) of the head vortices forming hairpin vortices at a)  $Re = 4500$  and its damping at b)  $Re = 500$  (red arrows denote velocity vectors scaled by factor of 0.5).

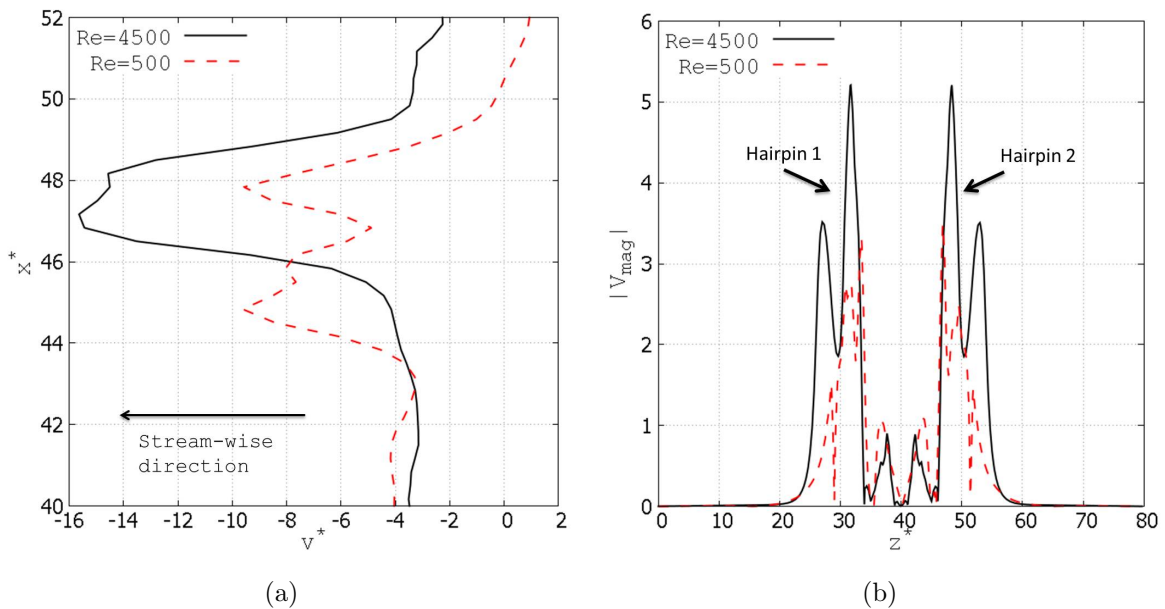


Figure 4.10: The velocity profile along  $x$ -axis placed at  $y^* = 45$  and  $z^* = 40$  a) and velocity magnitude of the fluid expelling from hairpin vortices at jet front along  $z$ -axis at  $x^* = 40$  and  $y^* = 45$  b).

The span-wise vortex roller goes through the large hairpin vortices (BHV and THV) at the front. These vortices undergo leapfrogging motion as demonstrated in Fig. 4.11. It is observed that THV remains intact for relatively longer period whereas, BHV gets annihilated during the leapfrogging. This behaviour is observed due to the direction of motion of the vortex roller, which is towards the BHV. During this process roller vortex undergoes significant distortion and results in small scale braid structures mostly oriented in stream-wise direction. This formation of braid structures is also aided by the distortion of THV resulting due to its interaction with other braid structures. Fig. 4.11(a) and Fig. 4.11(b) demonstrates the Q iso-surfaces ( $Q = 0.05$ ) for  $Re = 4500$  and  $Re = 500$  respectively at  $t^* = 18.74, 22.23$  and  $27.23$ . It is observed that the jet spread

for  $Re = 4500$  is much greater than that of  $Re = 500$ . This is due to the stabilizing effect of the viscous forces over the oscillating jet instability (refer Chapter 3). Another reason for this is the energy lost by the roller vortex, which results in subdued leapfrogging that leads to lesser fluid involvement.

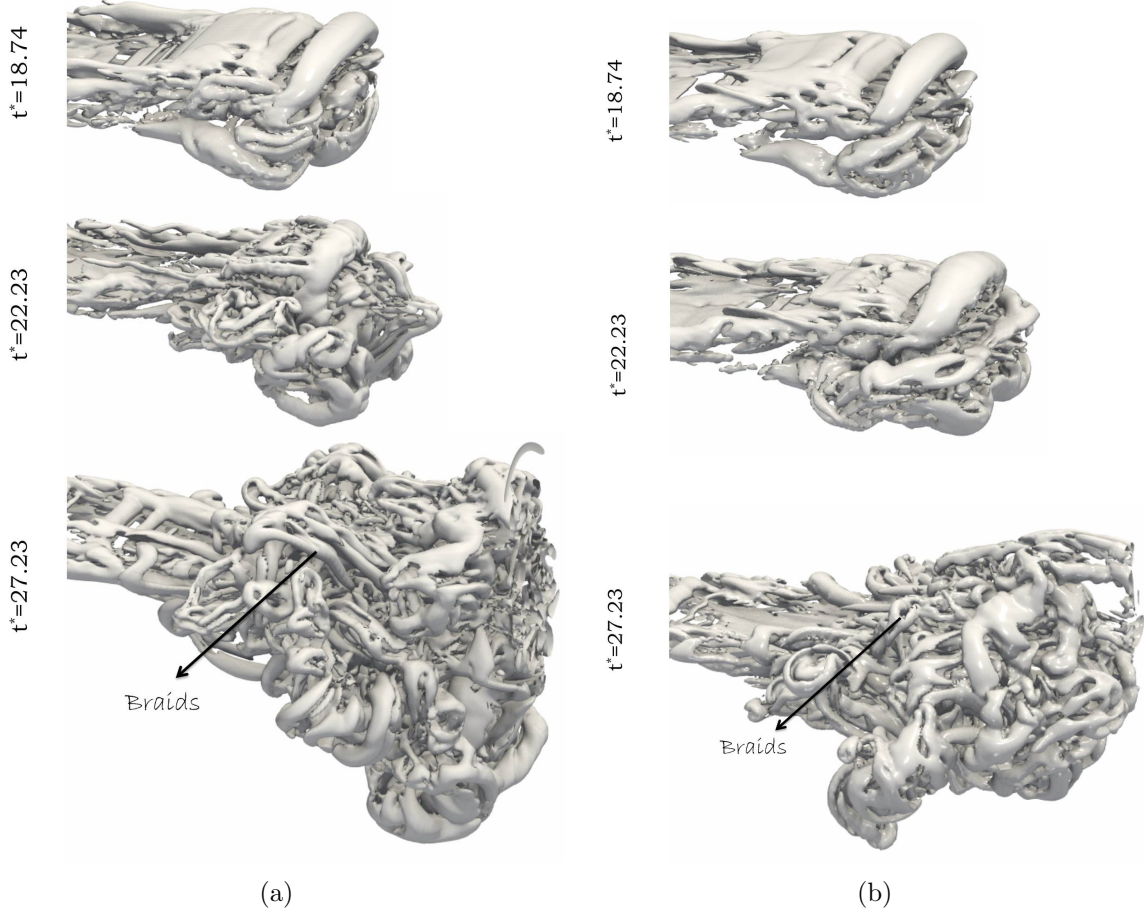


Figure 4.11: Q-criterion iso-surfaces ( $Q = 0.05$ ) for a)  $Re = 4500$  and b)  $Re = 500$  at  $t^* = 18.74, 22.23$  and  $27.23$ .

The flow field for  $Re = 500$  case is dominated by the presence of large scale structures as compared to  $Re = 4500$  where structures are much finer. Thus, in steady jet larger structures are known to improve the fluid involvement and as a result its entrainment<sup>34</sup>. On the other hand, the damping of oscillation amplitude reduces the jet spread in case of  $Re = 500$  which results in the reduced entrainment. Thus, the comparison of time-averaged stream-wise fluid entrainment for  $Re = 500$  and  $Re = 4500$  is depicted in Fig. 4.12. Here the mass entrained by jet is measured by applying Equation 4.5 over cross-section placed normal to the stream-wise direction. The mass entrainment is normalised using the time-averaged jet inlet mass flux  $\langle M_0 \rangle_T$ . It is observed through Fig. 4.12 that the entrainment increases downstream as a result of increased jet oscillations. Also, increase in Reynolds number improves the entrainment of the oscillating jet.

$$\langle M \rangle_T = \int_x \int_z \langle \rho^* v^* \rangle_T dx dz \quad (4.5)$$

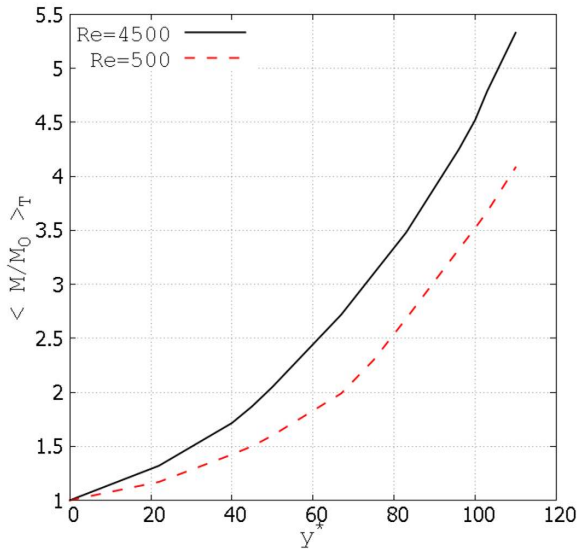


Figure 4.12: Comparison of time-averaged stream-wise entrainment between  $Re = 4500$  and 500.

## 4.2 Span-wise Vortex Structures

The fluid involvement in the oscillation direction and the interface disturbance is dominated by the span-wise vortices. These vortices mainly influence the region behind jet front and areas where jet exhibits maximum deflection. Fig. 4.13(a) demonstrates the schematic that explains the formation of KH roller vortices behind the jet front and their merger with the following vortex formed due to jet deflection. The air flow separates behind the front lobes and rolls up to form eddies<sup>117 118</sup>. These eddies disturb the interface behind the lobes that grows owing to KH instability. These eddies disturb the interface to a greater extent behind the THV as compared to BHV, as larger part of the jet falls into the trajectory of these eddies behind THV due to oscillating nature of the jet. It is to be noted that this mechanism will alternate between THV and BHV depending on the phase of oscillation of the liquid jet. The newly formed KH rollers are subjected to a greater aerodynamic drag from the fluid resulting in their formation (gas separating from the THV)<sup>117</sup>. Due to this transfer of momentum the KH rollers merge into the preceding vortex. Fig. 4.13(b) demonstrates the numerical results for the case of  $Re = 4500$  that depict the formation of KH rollers. It can be observed that the diameters of these KH rollers are smaller away from the point of maximum deflection. This is due to the merging of KH rollers as demonstrated in Fig. 4.13(c) where those formed near the point of maximum deflection are convected faster than others. This merging of KH rollers with the following large vortex leads to increase in the span of following vortex whose strength grows as it travels downstream.

The KH roller and the vortex formed due to jet deflection undergo deformations due to stretching and tilting forces<sup>118, 119</sup>. Thus, Fig. 4.14 demonstrates the comparison between span-wise stretching ( $\omega_z \partial w / \partial z$ ), stream-wise tilting ( $\omega_y \partial w / \partial y$ ) and normal tilting ( $\omega_x \partial w / \partial x$ ) for  $Re = 4500$  and  $Re = 500$ . It can be noted that the span-wise stretching dominates the  $\omega_z$  generation as compared to its tilting. Also,  $Re = 4500$  demonstrates span-wise stretching at-least two orders of magnitude greater than  $Re = 500$  which adds to its angular momentum.

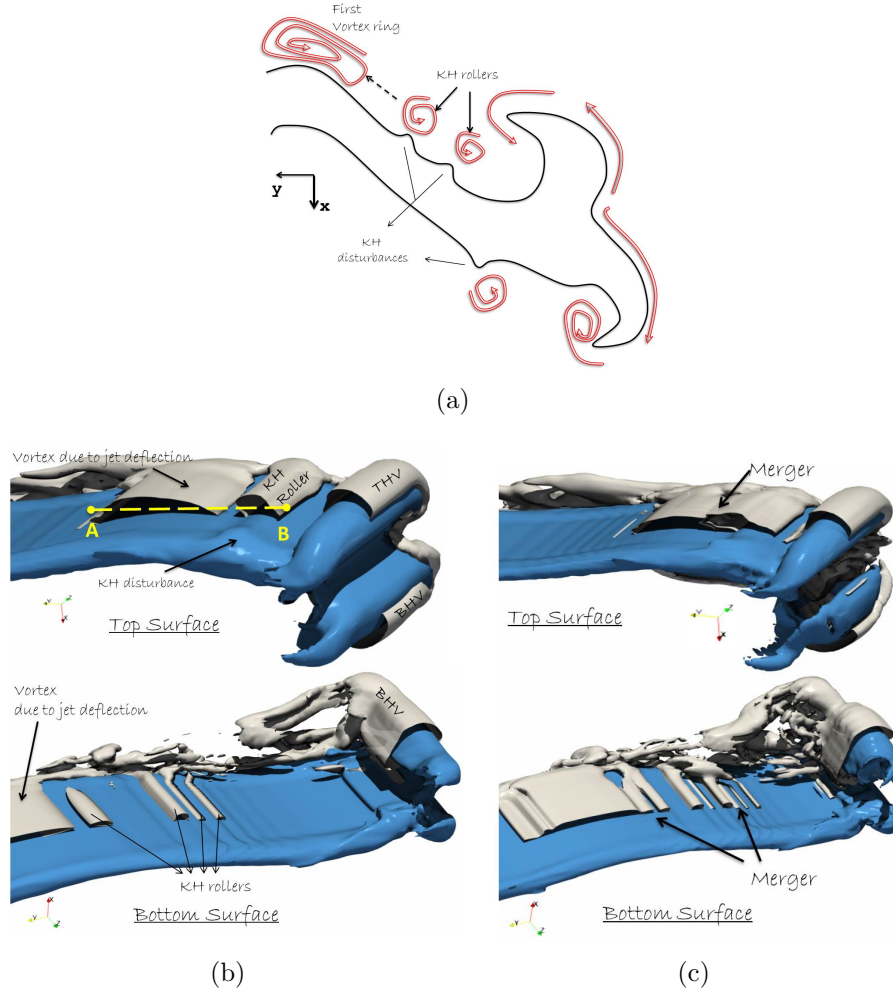


Figure 4.13: Formation and merging of KH rollers behind the jet front ( $Re = 4500$ ) shown by a) schematic and the numerical results for KH rollers b) forming at  $t^* = 16.32$  and their c) merging at  $t^* = 18.2$  for  $Q = 0.05$  (white) sliced by z-normal plane ( $z^* = 38$ ) with deflected jet (blue).

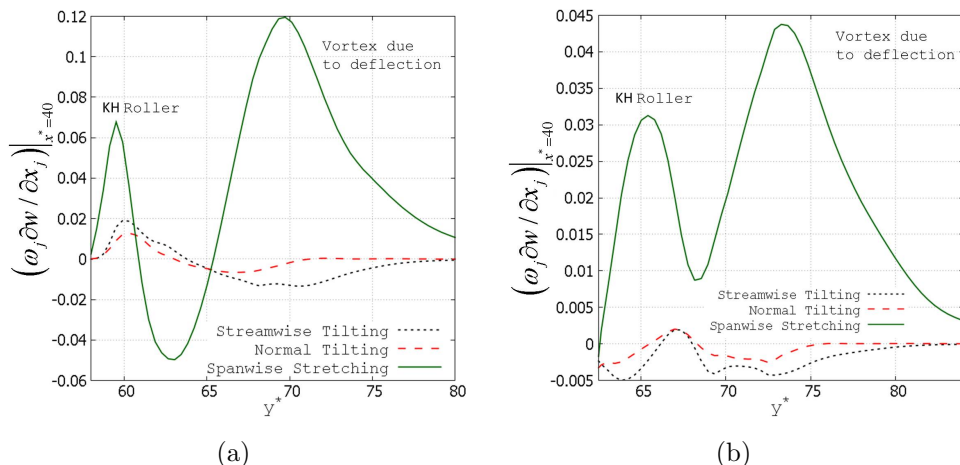


Figure 4.14: The magnitude of span-wise stretching, stream-wise tilting and normal tilting of KH roller and vortex at jet deflection along  $y - axis$  (segment A-B in Fig. 4.13(b)) at  $t^* = 16.32$  for a)  $Re = 4500$  and b)  $Re = 500$  ( $j$  being a repeating index).

In case of more viscous flow ( $Re = 500$ ) the surface shear gives rise to a distinct fluid behaviour. The KH rollers behind the jet front are identical to  $Re = 4500$  but have larger scales due to viscous diffusion. On the other hand, KH rollers near the jet deflection form KH crest and troughs due to surface deformations<sup>118</sup>. Fig. 4.15 demonstrates the top and bottom surface of the jet that exhibit interactions between KH rollers. The two KH rollers close to each other show symmetric nature of crest and troughs which are connected through a braid structure. These braid structures are formed due to stretching of the fluid between two rollers. The further stretching of the following KH roller breaks it down into the series of hairpin vortices which gets attached to the preceding KH roller with the help of connecting braids. Eventually, this formation gets merged into the vortex formed due to jet deflection. Also, it is understood that the fluid flow near the hairpin vortices slows down due to fluid being expelled through the legs of these vortices resulting in lesser entrainment.

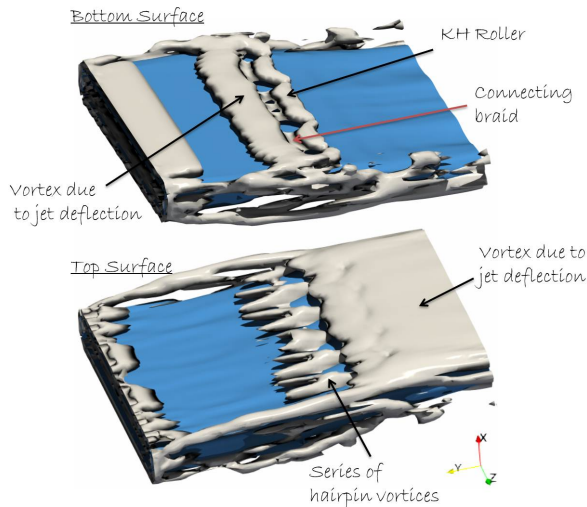


Figure 4.15: Span-wise vortices interacting at  $Re = 500$  shown by  $Q = 0.05$  (white) and jet (blue) iso-surfaces captured at  $t^* = 18.2$ .

### 4.3 Stream-wise Vortex Structures

The dominant stream-wise structures are covered in this section. These structures consist of the hairpin vortices formed over the sides of jet<sup>120</sup> and bursting of the spiralling trailing vortices. These vortex structures are found to significantly affect the fluid motion around them.

Fig. 4.16(a) demonstrates the mechanism through which the hairpin vortices are formed at the sides of jet. The trailing vortices which are nothing but the legs of THV and BHV rotate in a manner through which fluid is expelled between them. Furthermore, these vortex structures are stretched in the stream-wise direction to cause disturbances over their surfaces. Such disturbance grows to form a bridge between the two trailing vortices. Thus, these bridges result in the formation of hairpin vortices due to forward motion of the jet. These hairpin vortices undergo further breakdown as a result of stream-wise stretching. This mechanism is depicted through the numerical results for  $Re = 4500$  and  $Re = 500$  as in Fig. 4.16(b) and 4.16(c) respectively. These hairpin vortices create a passage for the fluid to be expelled away from the jet as shown by the velocity vectors (red)

in Fig. 4.16(b). On the other side, the bridging between the trailing vortices is delayed in case of  $Re = 500$  as the disturbances initially get damped due to viscous action. Once, these bridges are formed two hairpin vortices are observed on each side for  $Re = 500$  case. These vortices lose their strength quickly and breakdown shortly after formation due to greater resistance to their motion as compared to  $Re = 4500$ .

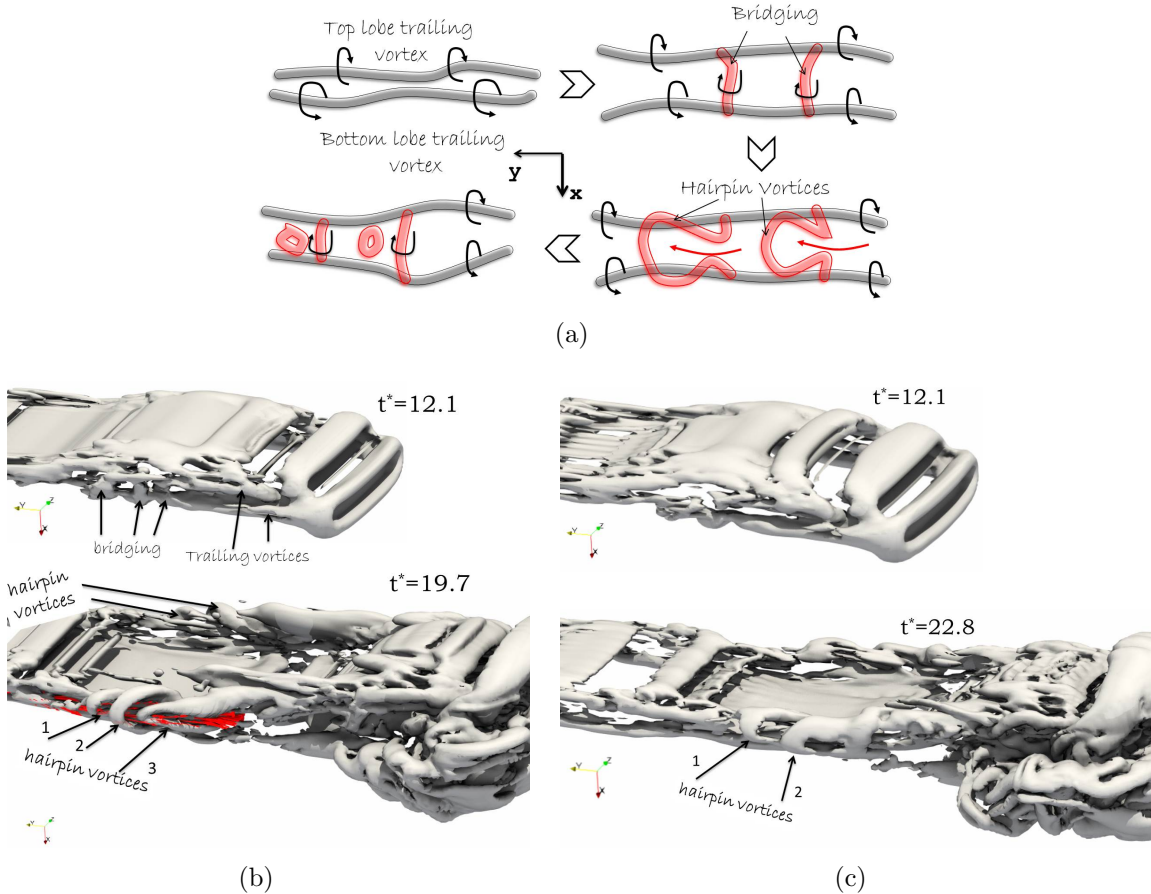
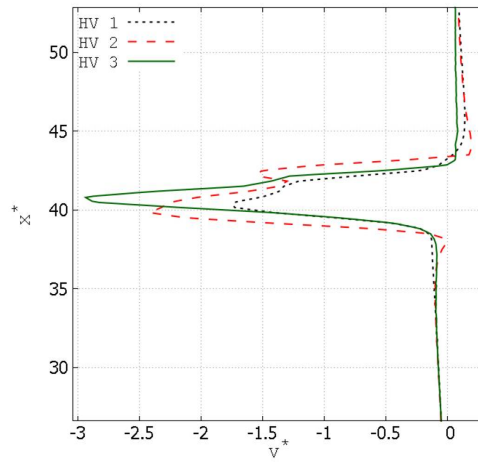


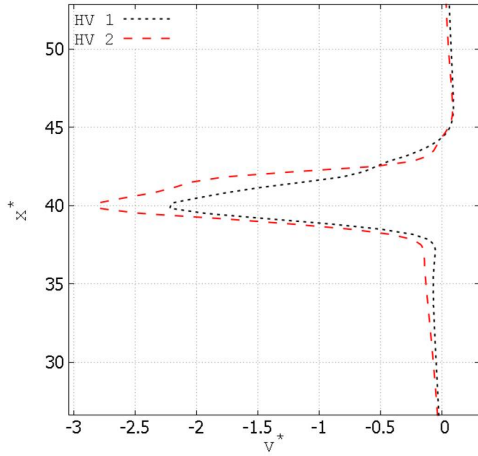
Figure 4.16: Formation of hairpin vortices shown by a) schematic and the numerical results for b)  $Re = 4500$  with red arrows denoting velocity vectors and c)  $Re = 500$  for  $Q = 0.05$ .

Moreover, Fig. 4.17 demonstrate the velocity profiles along  $x - axis$  inside the hairpin vortices at the jet sides. It is observed that the fluid accelerates through the passage created by these vortices due to induction of kinetic energy by these rotating structures. Also, based on their location hairpin 1 and 2 of  $Re = 500$  are analogues to hairpin 2 and 3 of  $Re = 4500$  which exhibit higher velocity as compare to  $Re = 500$ .

Another aspect of stream-wise vortex structures is the formation of spiral trailing vortices at the edges of jet at  $Re = 4500$  as depicted in Fig. 4.18. Initially the trailing vortices associated with the primary vortex formed due to jet oscillation are aligned in the stream-wise direction. As the trailing vortices lose their energy to the surrounding fluid the pressure at their core starts to increase and fluid moves to the periphery of these vortices<sup>121</sup>. This causes these vortices to take the spiral form giving rise to vortex bursting phenomenon. On the contrary, trailing vortices in the jet at  $Re = 500$  do not contain enough energy to self sustain and breakdown once the head vortices take complicated shapes.



(a)



(b)

Figure 4.17: The velocity profile along  $x - axis$  obtained inside three hairpin vortices at the sides (with 1 being near the inlet (Fig. 4.16(b))) for a)  $Re = 4500$  and b)  $Re = 500$ .

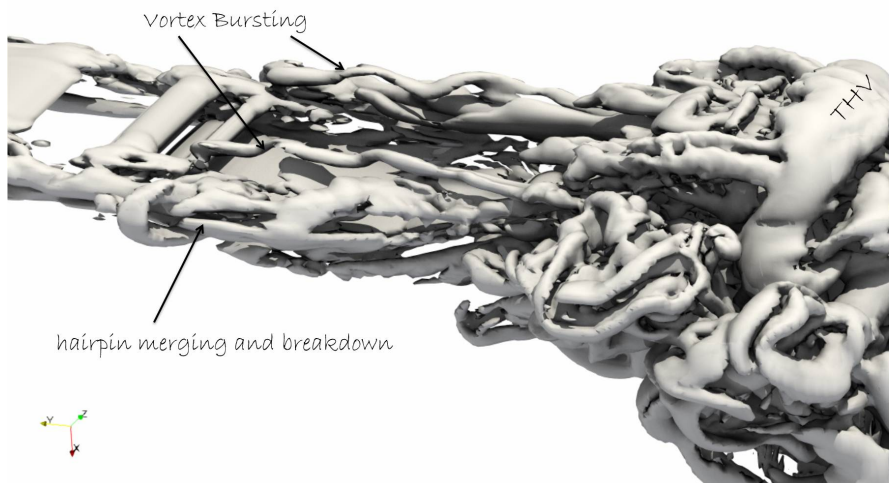


Figure 4.18: Stream-wise vortex bursting phenomenon at  $Re = 4500$ .

## 4.4 Proper Orthogonal Decomposition (POD)

Proper orthogonal decomposition determines the optimal set of eigenfunctions that can represent the data such that  $L_2$  norm of the given function in the data is maximized. The present analysis is performed over *x-normal* and *z-normal* planes that are placed at  $x^* = 40$  and  $z^* = 40$  respectively. Thus, velocity vectors ( $\vec{V}$ ) without mean-subtraction over this plane are used to perform POD as inclusion of mean flow is vital in extracting and comparing the derived information<sup>122</sup>. The present analysis is carried out using the *method of snapshots*<sup>123</sup>, where the flow field is stacked in column vectors forming matrix  $A \in \mathbb{R}^{m \times n}$  as,

$$A = \begin{bmatrix} V_1^{t_1} & V_1^{t_2} & \dots & V_1^{t_n} \\ V_2^{t_1} & V_2^{t_2} & \dots & V_2^{t_n} \\ \vdots & \vdots & \dots & \vdots \\ V_m^{t_1} & V_m^{t_2} & \dots & V_m^{t_n} \end{bmatrix} \quad (4.6)$$

such that, each column vector has  $m$  vectors equivalent to number of spatial locations over a plane considered for analysis (*xy* or *yz*) that are being stacked at each time interval  $t_i$  where,  $i = 1, 2, \dots, n$  up-to  $n$  snapshots. The present study considers 62 equidistant snapshots of the transient flow field. The matrix  $A$  undergoes *Singular Value Decomposition* (SVD) to obtain POD modes such that,

$$A = U\Sigma V^* \quad (4.7)$$

Here,  $U \in \mathbb{R}^{m \times m}$  and  $V \in \mathbb{R}^{n \times n}$  are the unitary matrices with orthonormal columns, while  $\Sigma \in \mathbb{R}^{m \times n}$  is a non-negative diagonal matrix. Here, superscript \* denotes the complex conjugate transpose. The matrices  $U$  and  $V$  acquire the spatial and temporal structures from the data, respectively. Therefore, the decoupled most dominant spatial structures obtained by  $U$  are often termed as POD modes or space-only POD modes<sup>124</sup>. Hence, the  $\vec{V}$  can be expressed by eigenfunction ( $\psi$ ) expansion as,

$$V(x, t) = \sum_{i=1}^n a_i(t) \psi_i(x) \quad (4.8)$$

where the variable  $a(t)$  accounts for all the temporal dependence of Equation 4.8 while the basis function  $\psi(x)$  characterizes for the spatial dependence. Fig. 4.19 demonstrates the amount of kinetic energy (KE) contained by each POD mode for  $Re = 4500$  and  $Re = 500$  in *z-normal* plane. It can be observed that the variation in energy content is minimal beyond  $n = 62$  and therefore, present study uses 62 snapshots for the ease of computation. Also, the energy distribution remains similar *xy* and *yz* planes. It is observed that first ten modes contain almost 75% energy of the data. Thus,  $Re$  has no effect on the reduced order of  $U$  matrix which is used to represent the data under consideration. The algorithm used to estimate POD modes for the present study is presented in Appendix A as Algorithm 1.

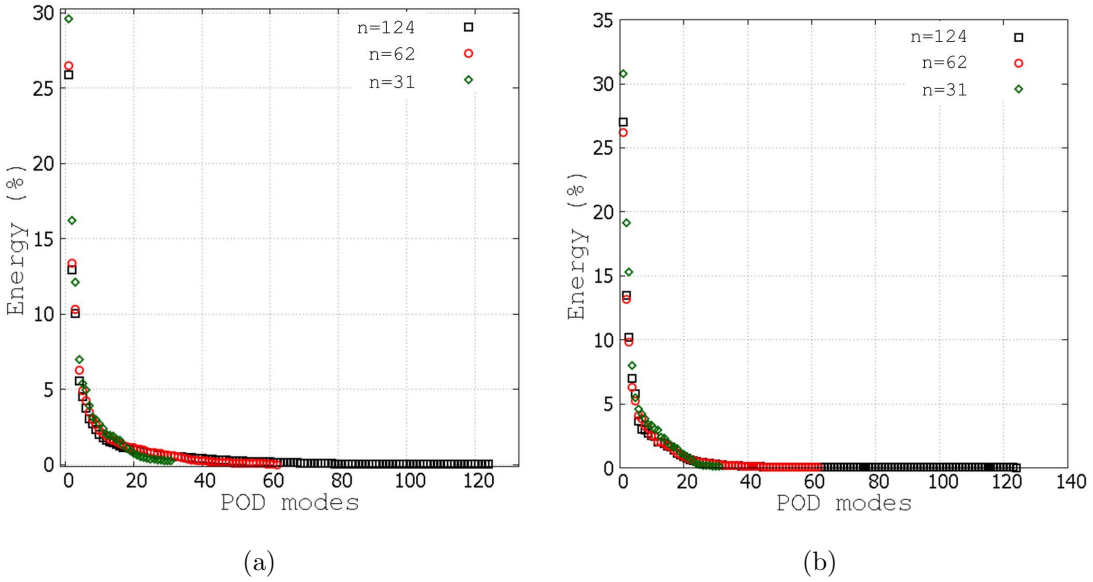


Figure 4.19: Kinetic energy content of POD modes for a)  $Re = 4500$  and b)  $Re = 500$ .

The contours for KE by first five dominant POD modes over  $xy$ -plane are demonstrated in Fig. 4.20 for  $Re = 4500$  and  $Re = 500$ . The first mode represents the ensemble average of flow field<sup>122</sup>. It is observed through first mode that  $Re = 4500$  demonstrates better spread of kinetic energy as compared to  $Re = 500$  owing to higher amplitudes of oscillations. The KE gain and loss in the local spatial region signifies the existence of vortical structures. Thus, the modes for  $Re = 500$  denote that the local structures which exist mainly at the jet deflections (peaks) and at downstream end when jet undergoes breakup. These structure diminish when higher modes are considered which indicates the loss of coherence due to viscous dissipation. On the other hand, for  $Re = 4500$  these structures remain dominant at the downstream as well as at the peaks of the deflected jet. Also, it is observed that for both cases KE being gained at the downstream end owing to the head vortex dynamics does lead to entrainment as discussed earlier.

Due to the three-dimensional nature of the flow, dominant vortical structures are also identified over the  $yz$ -plane placed at  $x = 40$  as demonstrated in Fig. 4.21. It can be observed that the structures formed at the peaks due to jet oscillations dominate the flow field for both  $Re = 4500$  and  $Re = 500$ . The third mode demonstrate the dominant effect of side hairpin vortices in case  $Re = 4500$  which for  $Re = 500$  are dampened. Also, unlike  $xy$ -plane the spread of kinetic energy for both cases of  $Re$  is identical in  $yz$ -plane. This is due to the fact that plane of oscillation ( $xy$ -plane) demonstrates the jet instability (increase in oscillation amplitude) whereas the plane normal to it ( $yz$ -plane) does not display any such flow instability apart from dissipation of kinetic energy.

The POD amplitudes  $a(t)$  for the first five modes over  $xy$ -plane are compared between  $Re = 4500$  and  $Re = 500$  in Fig. 4.22. It is depicted that the POD amplitudes grow with time signifying instability in the jet as is evident from the present numerical results. Initially for both  $Re$  cases, all modes share the same frequency which indicates that these modes are connected to the same coherent structures<sup>125</sup>. Considering the numerical results these structures correspond to the vortices present at the jet peaks and jet front. Also, there are instances where the amplitude of certain modes increase while for the same frequency other modes decrease in amplitude. This behaviour suggests that there is an energy exchange between these modes<sup>126</sup>. These energy exchanges between

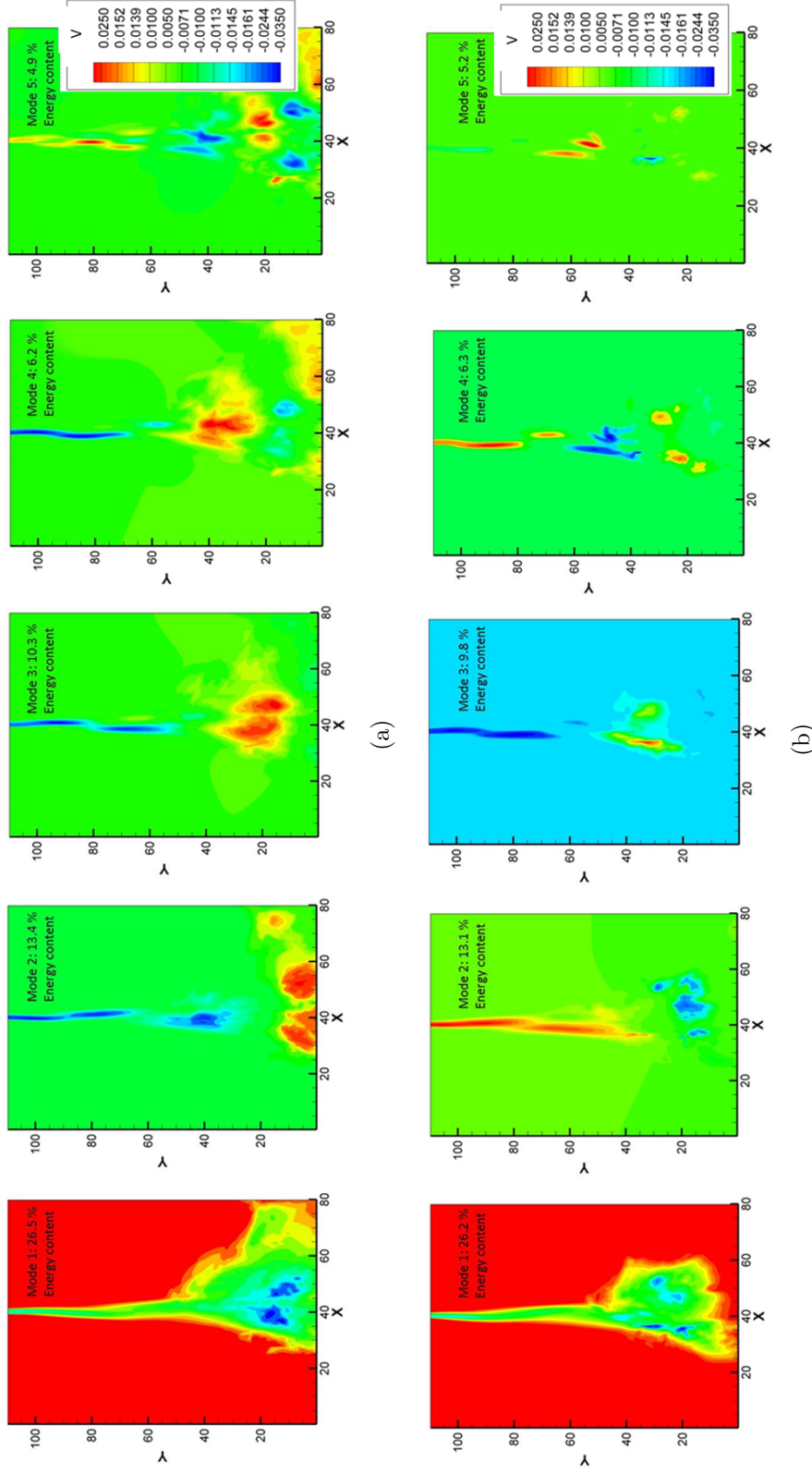


Figure 4.20: Velocity vector contours for eigenfunctions of first five dominant POD modes for a)  $Re = 4500$  and b)  $Re = 500$  over  $xy$ -plane.

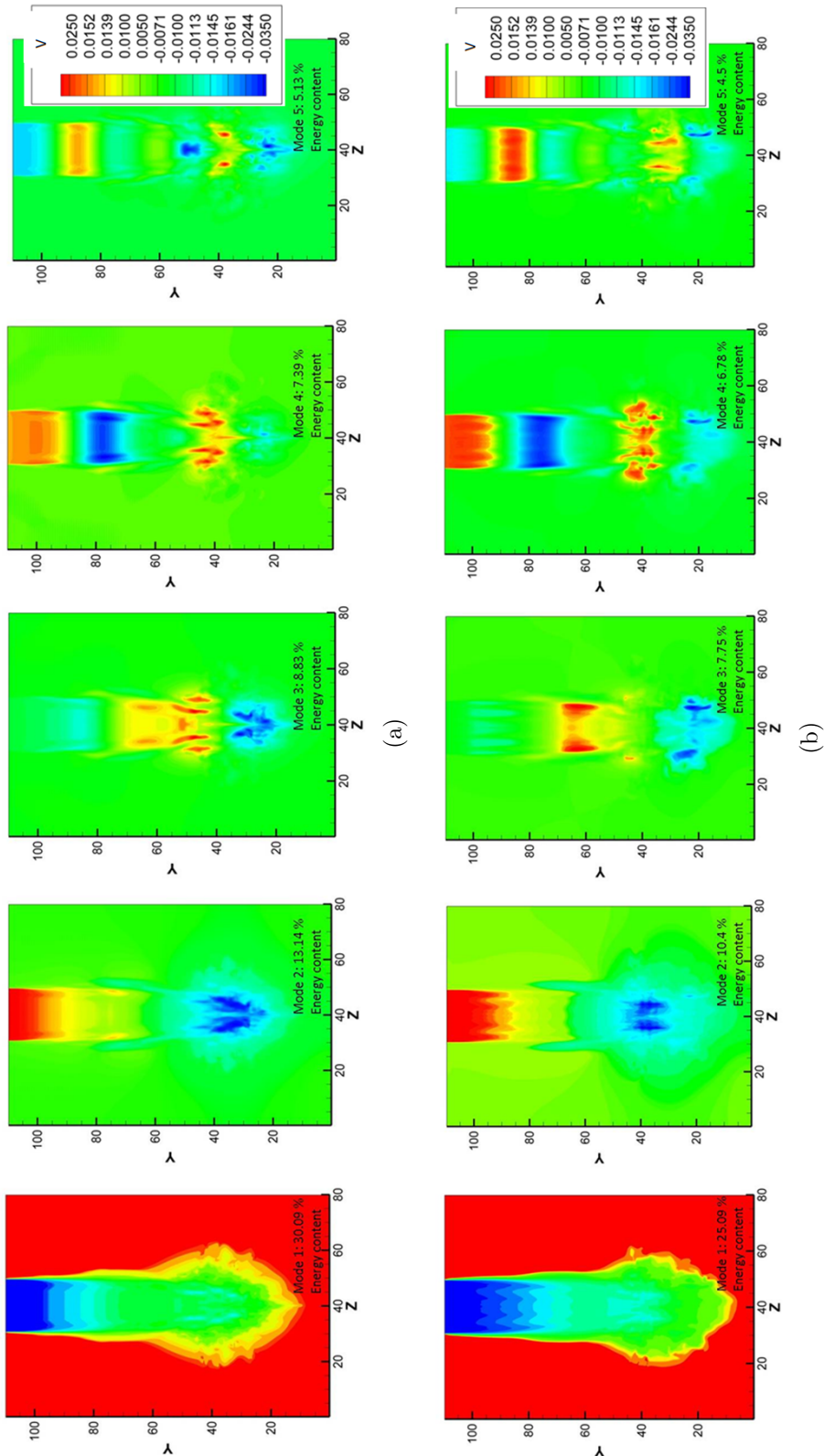


Figure 4.21: Velocity vector contours for eigenfunctions of first five dominant POD modes for a)  $Re = 4500$  and b)  $Re = 500$  in  $yz$ -plane.

modes seem to be more prominent beyond a certain point when head vortices undergo leapfrogging.

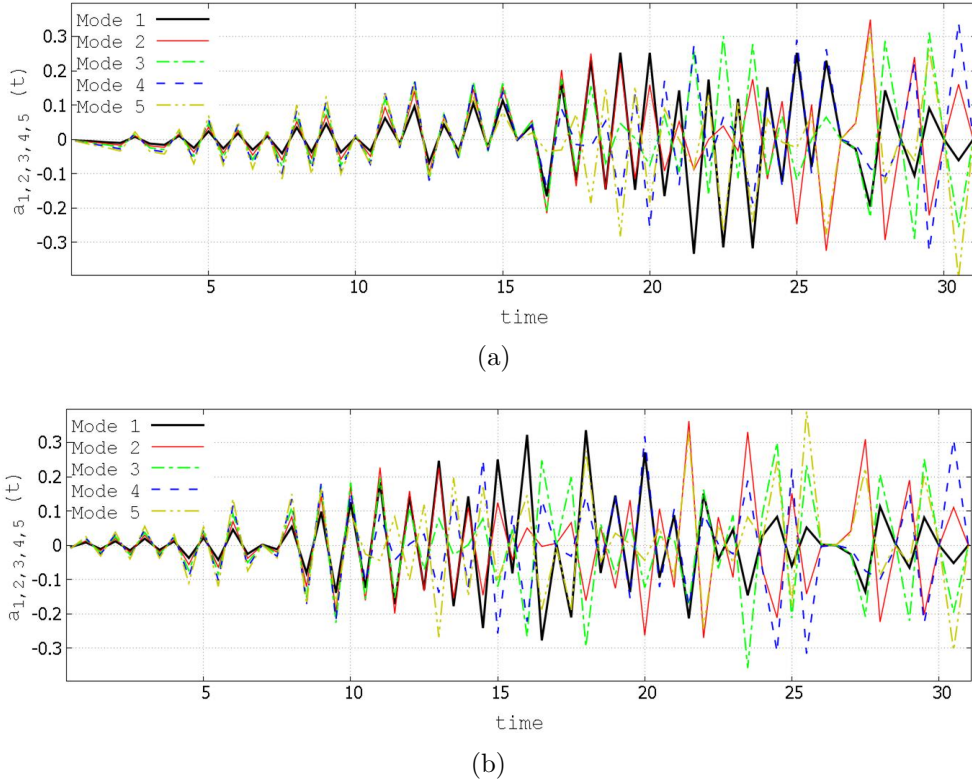


Figure 4.22: Variation of first five POD coefficients with time for a)  $Re = 4500$  and b)  $Re = 500$ .

## 4.5 Dynamic Mode Decomposition (DMD)

Dynamic mode decomposition<sup>127</sup> can reconstruct the spatial structures that develop linearly with time. DMD selects the leading eigenvalues ( $\lambda$ ) and eigenvectors ( $\Phi$ ) of the linear operator  $\mathbb{M}$  that relates the variable forward in time and the one in present.

$$\vec{V}^{t+\Delta t} \approx \mathbb{M}\vec{V}^t$$

Identification of these modes is based on their single frequency content, unlike POD where modes are selected based on their energy content.

The initial step is to construct two snapshot matrices, one of which is  $A$  as defined in Equation 4.6 and other constructed with a time shift  $t'_i = t_i + \Delta t$  ( $i = 1, 2, 3, \dots, n \rightarrow 62$ ) as

$$A' = \begin{bmatrix} V_1^{t'_1} & V_1^{t'_2} & \dots & V_1^{t'_n} \\ V_2^{t'_1} & V_2^{t'_2} & \dots & V_2^{t'_n} \\ \vdots & \vdots & \dots & \vdots \\ V_m^{t'_1} & V_m^{t'_2} & \dots & V_m^{t'_n} \end{bmatrix} \quad (4.9)$$

In practice instead of obtaining  $\mathbb{M}$ , a more computationally efficient  $\tilde{\mathbb{M}}$  is evaluated, which is a low rank projection of full matrix  $\mathbb{M}$  based on the POD modes. Therefore, once the

SVD of  $A$  is carried out the low dimensional linear operator  $\tilde{M}$  is evaluated as

$$\tilde{M} = U^* M U = U^* A' V \Sigma^{-1} \quad (4.10)$$

Finally, we can obtain the DMD modes  $\Phi$  (eigenvectors of  $M$ ) through Equation 4.11 by carrying-out eigen-decomposition of  $\tilde{M}$  having its eigenvector as  $\mathbb{W}$ .

$$\Phi = A' V \Sigma^{-1} \mathbb{W} \quad (4.11)$$

Therefore, the objective of DMD method is to estimate matrix  $\tilde{M}$  such that a linear relationship between two offset matrices  $A = [V_0 \dots V_{n-1}]$  and  $A' = [V_1 \dots V_n]$  can be established. The eigenvalues of  $\tilde{M}$  then can be used to estimate the DMD modes  $\Phi$ . The pseudocode for estimating the DMD modes is provided in Appendix A as Algorithm 0.

The spectra of Ritz values (eigenvalues) are shown for  $Re = 4500$  and  $Re = 500$  in Fig. 4.23. Modes inside the unit circle are dissipative and decay over the time while, the modes outside are explosive, showing higher growth rates. Thus, modes close to unit circle are selected that represent the attracting set. These modes ( $|\lambda| \sim 1$ ) are most energetic and have resemblance to mean of the data set<sup>128</sup>.

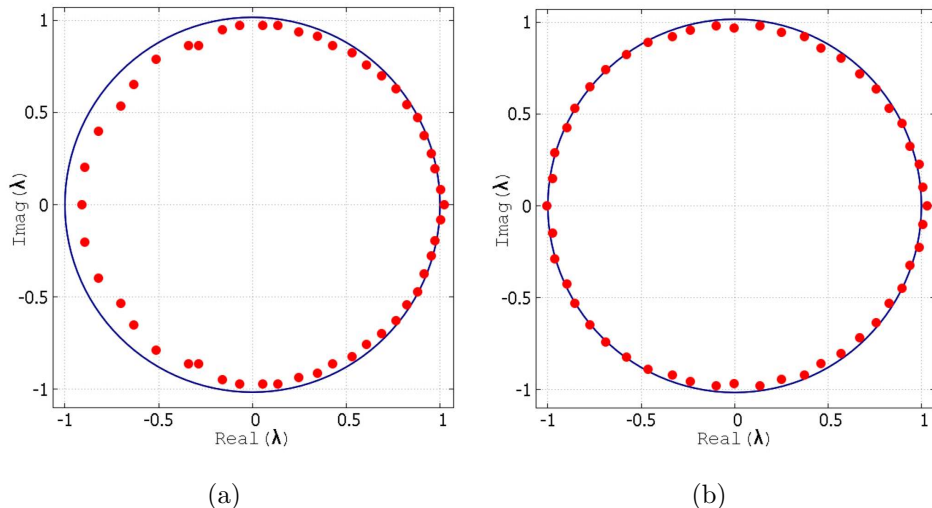


Figure 4.23: Ritz values ( $\lambda_i$ ) in complex plane for a)  $Re = 4500$  and b)  $Re = 500$ .

Fig. 4.24 demonstrate the first five eigenvectors (DMD modes) for  $Re = 4500$  and  $Re = 500$  over  $xy$ -plane with their Strouhal number ( $St = f_i h_0 / U_\infty$ ). Here,  $f_i = 2\pi \text{Im}(\log(\lambda_i)) / \Delta t$  with  $\lambda_i$  being the complex eigenvalue of  $i^{th}$  DMD mode. Similar to POD modes, DMD modes also predict the decaying of flow structures in jet at  $Re = 500$ . An additional feature DMD modes demonstrate is the existence of symmetric vortex structures in the near field that arise due to periodic jet oscillations. It is observed that the vortex structure grow at the downstream. THV and BHV demonstrate the maximum energy dissipation at the downstream suggesting increase in the entrainment characteristics for  $Re = 4500$ .

The DMD modes over  $yz$ -plane are demonstrated in Fig. 4.25 for both the  $Re = 4500$  and  $Re = 500$ . Similar to the POD modes the DMD modes demonstrate the existence of vortices at the jet peaks/ deflection. The additional flow feature that the DMD modes predict is the hairpin vortices present at the jet front as well as the sides, which is evident from second and fourth mode for  $Re = 4500$ . Moreover, the third mode displays that the trailing vortices at the jet edges also have an effect on the flow field.

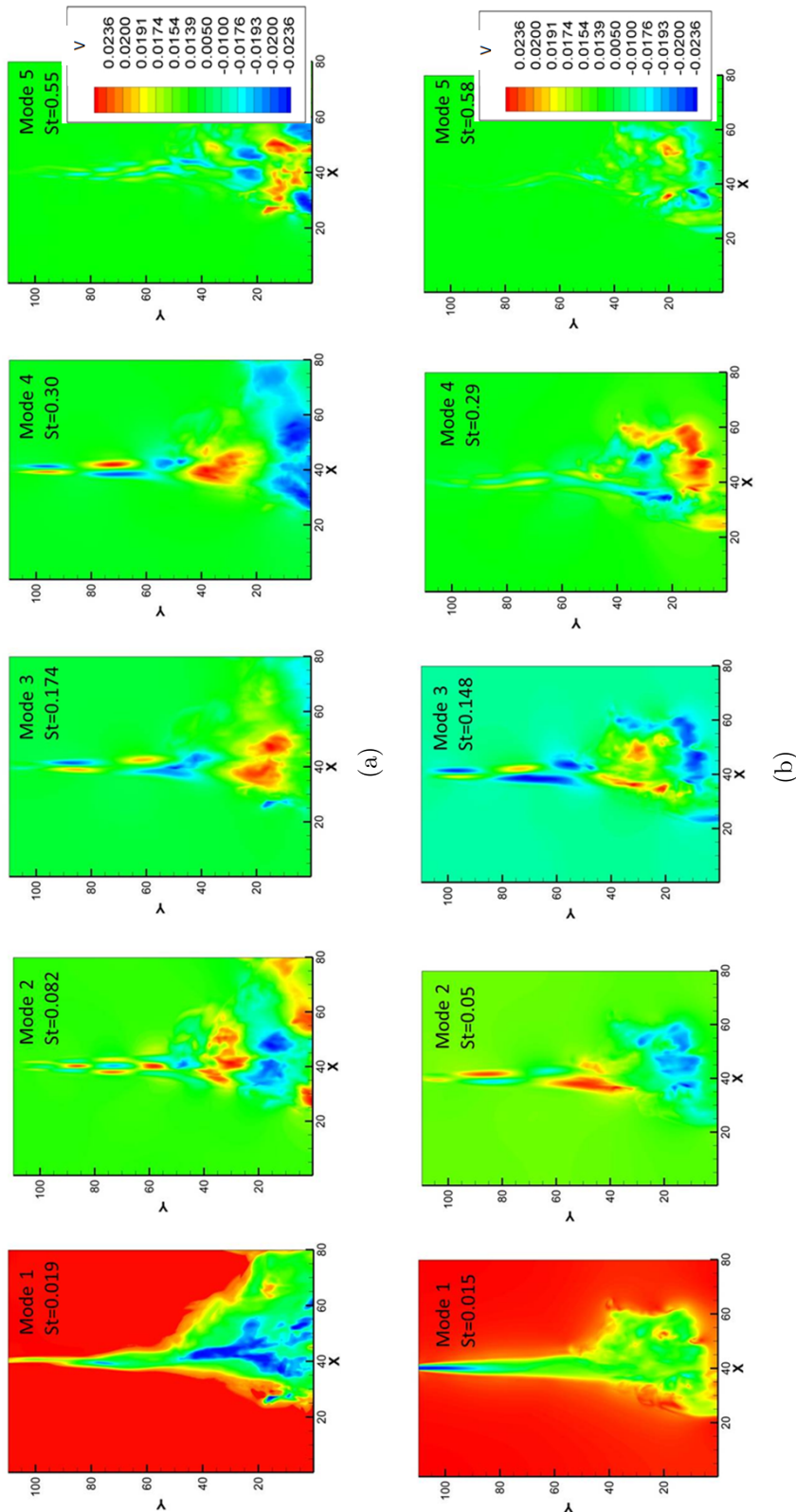


Figure 4.24: Velocity vector contours for eigenfunctions of first five dominant DMD modes for a)  $Re = 4500$  and b)  $Re = 500$  in  $xy$ -plane.

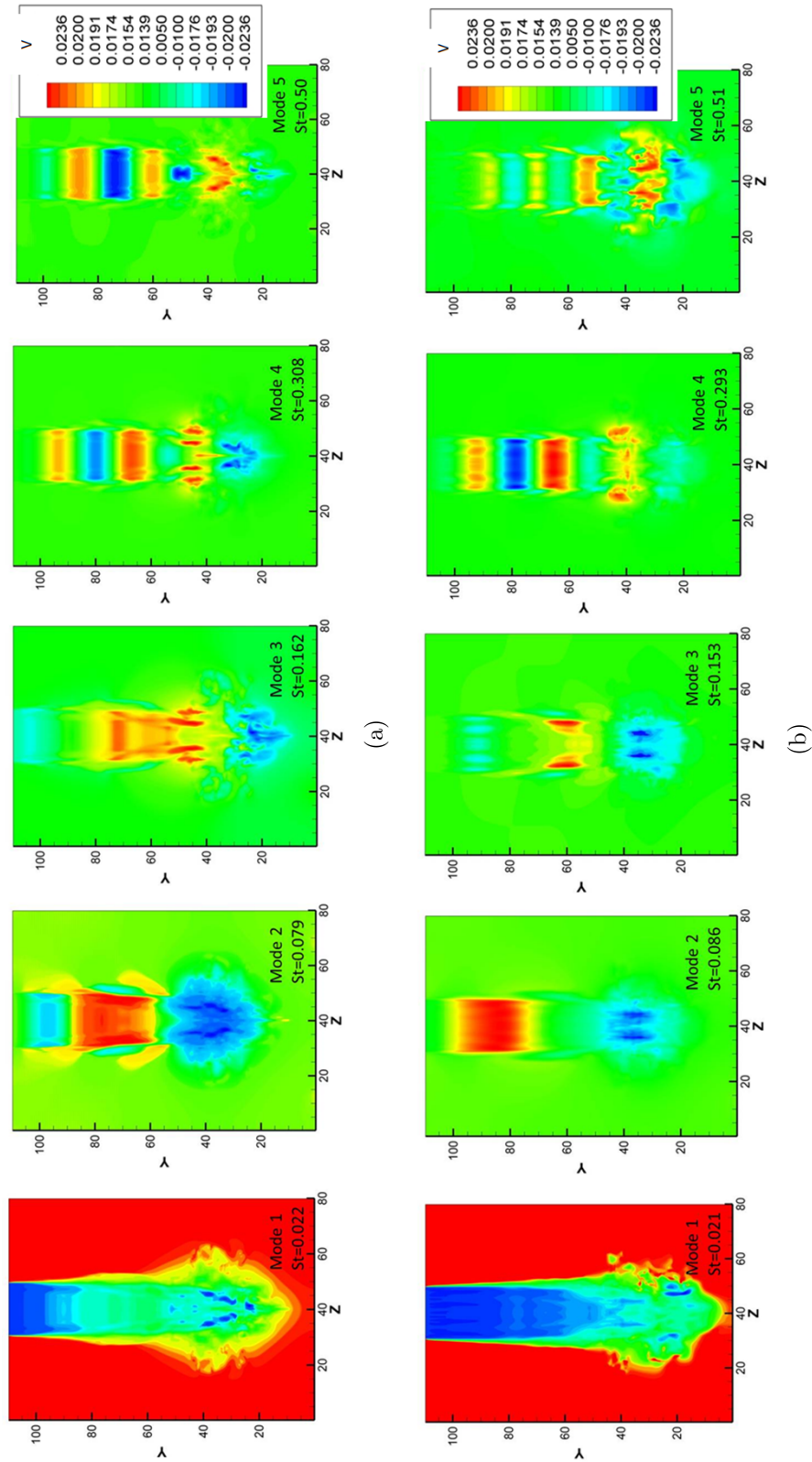


Figure 4.25: Velocity vector contours for eigenfunctions of first five dominant DMD modes for a)  $Re = 4500$  and b)  $Re = 500$  in  $yz$ -plane.

## 4.6 Closure

The formation, evolution, and interaction of coherent structures associated with the oscillating planar jet at  $Re = 4500$  and  $Re = 500$  are numerically investigated. The dominant structures in the flow field are identified and analyzed using proper orthogonal decomposition (POD) and dynamic mode decomposition (DMD). The present study demonstrates that the jet front contributes significantly to the momentum transport and results in entrainment of fluid. This vortex dynamics at the front is dominated by head vortices, which later transform into large hairpin vortices (THV and BHV) that annihilate as a result of leapfrogging. This dynamics and jet spread at the front are damped significantly by the viscous forces as is evident from the results for the  $Re = 500$  case. The contribution of span-wise structures to momentum transport is also noticeable. The eddies shed behind the head vortices disturb the jet surface, resulting in the formation of KH rollers. The KH rollers as well as the vortices formed due to jet oscillations experience span-wise stretching, which enhances their angular momentum. The viscous forces significantly affect these KH rollers and their merging with deflection vortices at jet peaks. This results in the formation of a series of hairpin vortices aligned in the stream-wise direction that affect the flow field around them. Entrainment of fluid is also affected by the sideways hairpin vortices formed over the trailing vortices. These hairpin vortex structures form a passage that expels the fluid out of it and also accelerates the fluid in this process. For  $Re = 500$ , the results demonstrate significant energy dissipation of these vortices causing their early breakdown.

The reconstructed flow field for the most dominant POD and DMD modes successfully identifies the important structures in the flow. POD modes demonstrate the decay of flow structures at the downstream in the case of viscous flows ( $Re = 500$ ), whereas, for the  $Re = 4500$  case, it is observed that the most dominant structures are present at the downstream. On the other hand, DMD reconstruction agrees well with the POD results and suggests the existence of symmetric flow structures at the jet deflections due to periodic oscillations of the jet. It is also revealed through the modal analysis that the hairpin vortices both at the jet front and sides tend to dominate the flow field. Moreover, the spread of kinetic energy in the plane of oscillation proves to be greater than over the plane normal to it.

*This page intentionally left blank.*

---

## CHAPTER 5

---

### OSCILLATING LIQUID JETS IN TANDEM

The previous studies provide an information on the internal flow field of dual *fluidic oscillators* and impingement characteristics of oscillating jets. But, the flow features governing the development of dual oscillating jets are not investigated in the previous literature. Therefore, fundamental flow field of the dual oscillating jets needs further investigations to understand their development, stability of oscillations and interactions. This understanding of tandem oscillating jets can significantly improve the efficacy of industrial applications involving flow control, mixing and heat transfer processes. Therefore, the present study reports the numerical results for synchronous and asynchronous spatially oscillating planar liquid jets. The effect of nozzle spacing on the instability, jet development and interaction of the vortical structures of these jets is investigated. Moreover, the interactions between coherent structures of individual oscillating jets is also reported here. The present study is based on an in-house *NavierStokes* based two-phase flow solver that uses algebraic VOF method as discussed in Chapter 2.

In the present study computational domain size is based on the nozzle spacing ( $N$ ). Thus, for nozzle spacing ( $N$ )  $N_1 = 19h_0$ ,  $N_2 = 14h_0$  and  $N_3 = 9h_0$  the domain size  $80h_0 \times 110h_0 \times 80h_0$ ,  $60h_0 \times 110h_0 \times 80h_0$  and  $40h_0 \times 110h_0 \times 80h_0$  is selected respectively. The boundary conditions and domain setup considered for the synchronous and asynchronous oscillating jets is demonstrated in Fig. 5.1. The tandem oscillating water jets of thickness  $2h_0$  and width  $w_0$  emanate through the inlets provided at the top face of the domain into a quiescent air. These jets are subjected to an inlet velocity  $V_{in}$  as they fall in the  $-y$  direction under the influence of gravity.

The left vertical faces of the domain are treated with the periodic boundary condition whereas the front and back vertical faces are provided with a free slip condition. The bottom face acts as a pressure outlet for the fluids whereas, the top face contains two equidistant liquid inlets with rest of the face being treated as a wall. The inlet velocity condition for the jet has two components in  $x$  and  $y$  directions as  $u^*$  and  $v^*$  respectively. The  $y$ -component velocity has parabolic profile with mean velocity being  $V_{in}$  to emulate the fully developed velocity profile. The  $x$  – component of the velocity acts as the sinuous perturbations for the jets which at the downstream end develops into instability. Thus, at the inlet, transverse and axial velocity components for the synchronized oscillating jets are given by Equation 5.1 whereas, for the asynchronous jets ( $180^\circ$  out of phase) they are given by Equation 5.2

$$\begin{aligned} u^*_{\text{both jets}} &= A_0 \sin(2\pi St \times t^*) \\ v^* &= V_{in} \end{aligned} \tag{5.1}$$

$$\begin{aligned} u_{jet1}^* &= A_0 \sin(2\pi St \times t^*) \\ u_{jet2}^* &= A_0 \sin(\pi + 2\pi St \times t^*) \\ v^* &= V_{in} \end{aligned} \quad (5.2)$$

where,  $St$  is the *Strouhal number* that represents perturbation frequency ( $f$ ) of jet that is subjected to an initial oscillation amplitude of  $A_0$  and  $St$  is defined as  $St = fU/h_0$ . The present study considers the physical properties of air and water at normal temperature and pressure, and the definition for key non-dimensional numbers similar to Chapter 3 are used.

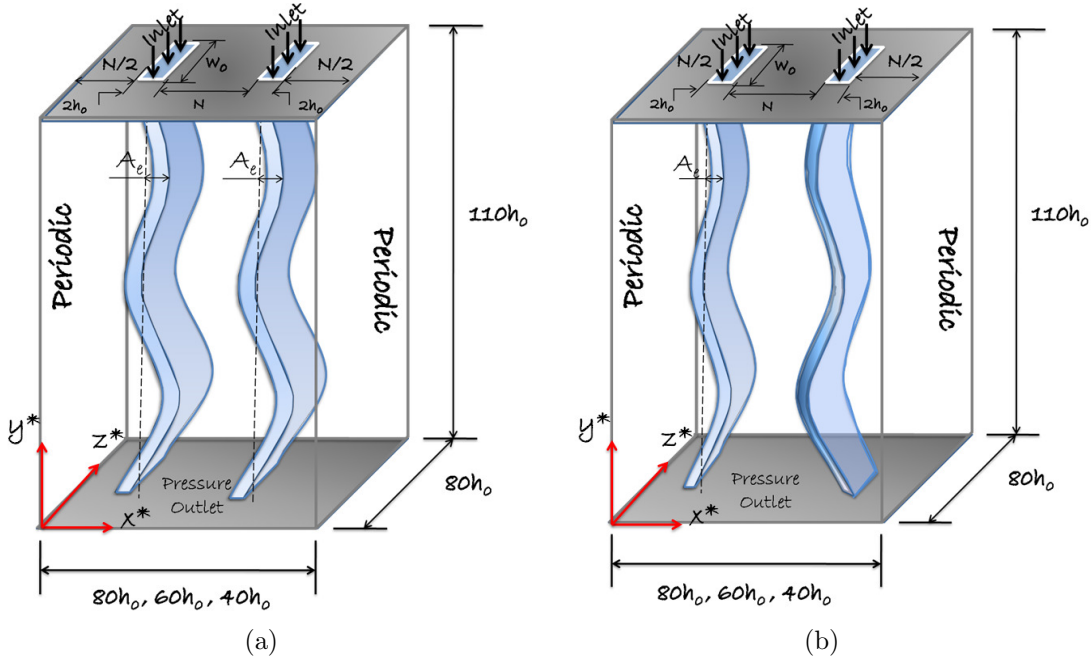


Figure 5.1: Computational domain and boundary conditions for a) synchronous and b) asynchronous oscillating jets.

The grid refinement studies based on *Richardson's extrapolation*<sup>106</sup> were previously carried out in Chapter 4. It is demonstrated that when the spatial refinement in all three directions is performed using three grid levels, the *Grid Convergence Index* (GCI) between medium and the finest grid was within the convergence limits. Therefore, for the present study, grid resolution of  $360 \times 470 \times 360$ ,  $270 \times 470 \times 360$  and  $180 \times 470 \times 360$  are selected for nozzle spacing configuration of  $N_1$ ,  $N_2$  and  $N_3$  respectively. Moreover, the simulations are carried out for  $t^* = 64$  similar to Chapter 4.

Validations for the present numerical model with the experimental results of<sup>12</sup> Asare et al. were previously discussed in Chapter 3 and 4. These validations are carried for the growth envelope ( $A_e/A_0$ ) that evolve due to the instability associated with the oscillations of these jets and were found to be in agreement with the experimental results.

In the present chapter, the development, instability and vortical structures of oscillating jets in tandem configuration is analysed. The present analysis is aimed at understanding the effect of nozzle spacing ( $N$ ) on these jets.

## 5.1 Synchronous Tandem Jets

### 5.1.1 Development of Synchronous Jets

Fig. 5.2 demonstrates the development of the oscillating jets in tandem for three different nozzle spacing configurations. It is observed that the mechanism for the formation of flow features such as, two jet front lobes ( $t^* = 15.24$ ), their transformation into upward plumes due to *Rayleigh Taylor* (RT) instability ( $t^* = 18.75$ ) and their breakup ( $t^* = 27.26$ ) are similar to a single oscillating jet as discussed in Chapter 4. Moreover, the upward plumes are affected by the nozzle spacing as depicted in Fig. 5.2. These plume are stretched in the upward direction more due to the aerodynamic forcing as is evident from Fig. 5.3. The Fig. 5.3 demonstrates the upward stream-wise velocity ( $v^*$ ) acting in the region (segment A-B in Fig. 5.2) between the two jets. It is observed that as the nozzle spacing reduces the upward velocity in this region increases, resulting in a stretching of the upward plumes that eventually breakup.

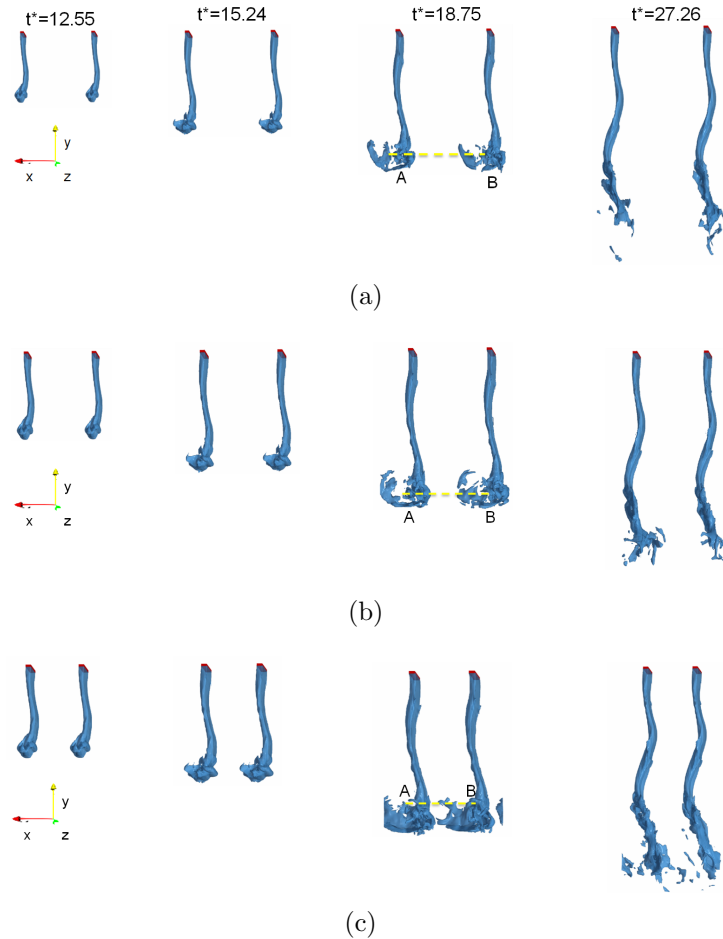


Figure 5.2: Development of tandem oscillating jets for nozzle spacing a)  $N_1 = 19h_0$ , b)  $N_2 = 14h_0$  and c)  $N_3 = 9h_0$ .

As the two oscillating jets develop, the analysis of their velocity profiles can provide vital information regarding their behaviour. Fig. 5.4 demonstrates the phase averaged stream-wise velocity profiles at different  $y^*$  locations of the domain. The phase averaging as in <sup>129</sup> is performed by dividing the oscillation period into four phase angles which

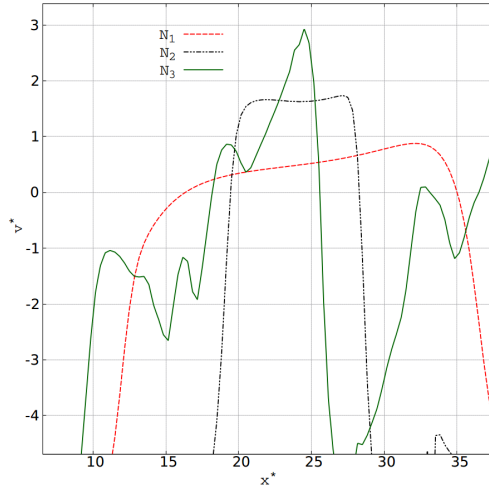


Figure 5.3: Velocity profiles along a segment  $A-B$  (Fig. 5.2) placed between the upward plumes of the two jets.

resulted into 18 simulation files per phase angle. Moreover, the procedure for phase averaging is provided in Appendix B. It is observed that in the near-field the velocity profile for all the nozzle spacing configuration are identical. Moreover, an individual jet velocity profile is similar to that of the single oscillating jet. In the near-field, each velocity profile is associated with the reverse flow at one end representing vortex structure at the oscillation peak (refer Chapter 3), whereas, broader profile on the other end representing the stretching of shear layer. At the downstream, region between the two jets do not demonstrate any reversed flow ( $v^* < 0$ ) apart from individual oscillation peak vortices. This region can be termed as a merging flow region where both velocity profiles have merged. On the other hand, the flow region before this merging can be termed as converging flow region. It is observed that, as the nozzle spacing increases, the merging point of the velocity profiles shifts towards the downstream end of the domain. Merging point for nozzle spacing  $N_1$ ,  $N_2$  and  $N_3$  occur at  $y^*$  locations 50, 55 and 58 respectively. Moreover, it is observed that, the nozzle spacing and merging point distance share a linear relationship for oscillating tandem jets; which is similar to steady tandem jets<sup>54</sup>. Further downstream of the domain, velocity profiles become more complicated and distinction between individual jet profiles cannot be performed. Therefore, the fluid attains maximum velocity suggesting existence of combined flow region. This flow region is observed to appear earlier when nozzle spacing is the least ( $N_3$ ). Hence, as these merging and combined flow regions shift towards the upstream for smaller nozzle spacing, it is inferred that such configurations will increase the fluid mixing.

### 5.1.2 Stability of Synchronous Jets

The sinusoidal perturbations of an initial amplitude  $A_0$ , that are provided at the inlet of these jets grow downstream owing to an instability associated with them. This instability occurs due to the low pressure region created by the vortical structures formed at each oscillation peak (refer Chapter 3). The growth of oscillation amplitude ( $A_e/A_0$ ) is measured along the stream-wise direction and its comparison at different nozzle spacing configurations is demonstrated in Fig. 5.5. The growth rate demonstrated by both jets in tandem configuration are identical and thus, amplitudes associated with only one jet

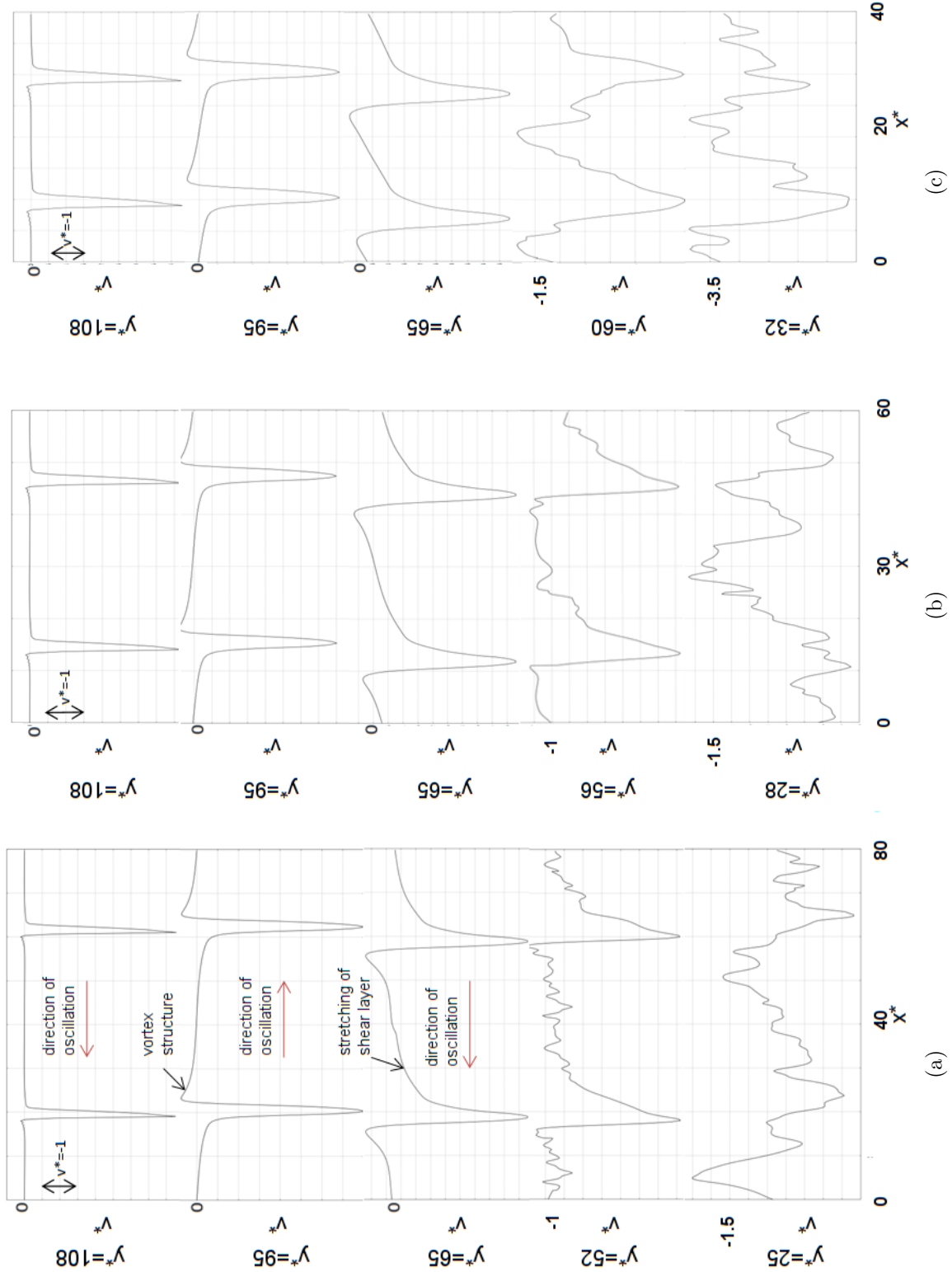


Figure 5.4: Phase averaged  $\text{V}^*$  velocity profiles of tandem oscillating jets in the stream-wise direction for nozzle spacing a)  $N_1 = 19h_0$ , b)  $N_2 = 14h_0$  and c)  $N_3 = 9h_0$  at  $z^* = 40$ .

is considered in Fig. 5.5. It is observed that, the growth rate for nozzle spacing  $19h_0$  is identical to a single oscillating jet. Hence, effect of the nozzle spacing on the jet instability is only noticeable when  $N < 19h_0$ . Moreover, it is also observed that as the nozzle spacing decreases the jet is destabilized and its oscillation amplitude increases. This influence of nozzle spacing on the jet stability can be understood through the analysis of enstrophy values  $\omega_z^2$  associated with the vortex structures at each oscillation peak, where,  $\omega_z$  is the vorticity over  $z^*-plane$ . Fig. 5.6 depicts the enstrophy values for different nozzle spacings at a typical oscillation peak of the jet. It is observed that, the enstrophy values increase at decreasing nozzle spacing. Thus, this signifies that, the intensity of vortex rotation at an oscillation peak grows as the nozzle spacing reduces. This results in a formation of low pressure region at these peaks which promote the instability at smaller nozzle spacings.

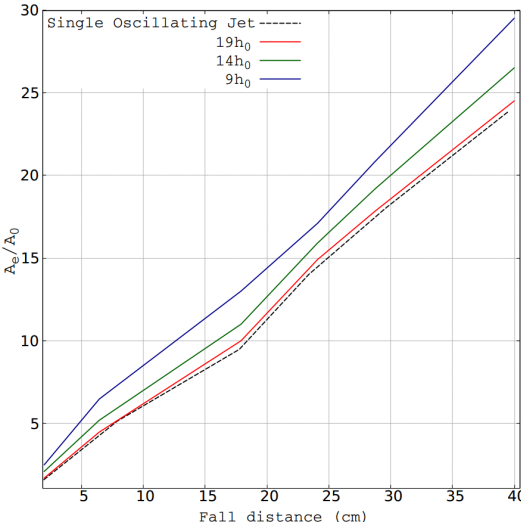


Figure 5.5: Comparison between growth of oscillation amplitudes ( $A_e/A_0$ ) associated with tandem oscillating jets at different nozzle spacing.

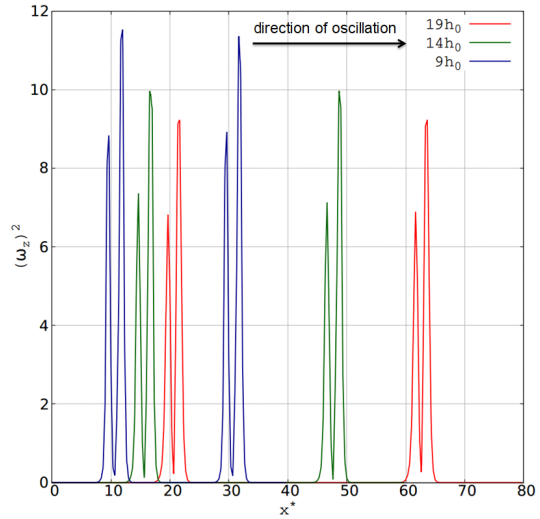


Figure 5.6: Comparison of the enstrophy values ( $\omega_z^2$ ) at a typical oscillation peak ( $y^* = 93.5$ ) at different nozzle spacings.

### 5.1.3 Interaction of Coherent Structures in Synchronous Jets

The coherent structures in the present study are identified using *Q-criterion*<sup>130</sup>. The fundamental coherent structures such as (top) (THV) and bottom (BHV) head vortices, *kelvin-Helmholtz* (KH) rollers, trailing vortices and oscillation peak vortices in a single oscillating jet are even preserved within the tandem configuration. An interaction of these structures for twin oscillating jets is significantly affected by the nozzle spacing. Thus, most dominant form of interaction, which is between THV and BHV of the two jets occur for the nozzle spacing of  $9h_0$ . Fig. 5.7 demonstrates the vortical structures (sliced section at  $z^* = 42$ ) and their interaction zone for nozzle spacing  $9h_0$ . Both THV and BHV form a counter-rotating two vortex system as depicted in Fig. 5.7(b). Thus, these vortices undergo short-wavelength instability<sup>131</sup> promoting the formation of secondary vortices over the THV. This results in the deformation of jet interface in the form of stream-wise ridges which affect the air flow over them and alter the formation of KH rollers.

Another aspect of this interaction is the transfer of energy from THV to BHV. Fig. 5.8 demonstrates the enstrophy values between the two vortices along segment  $A - B$  (Fig. 5.7(b)). It is observed that, THV has higher intensity of rotation as compared to BHV.

Thus, when these two vortices interact, THV loses its kinetic energy to BHV and decays downstream. It is also observed from Fig. 5.7(b) that, these counter-rotating vortices entrain fluid from the downstream end and accelerate it towards the region between the two jets. As a consequence of this entrained fluid a pair of stream-wise hairpin vortices are formed as demonstrated in Fig. 5.9.

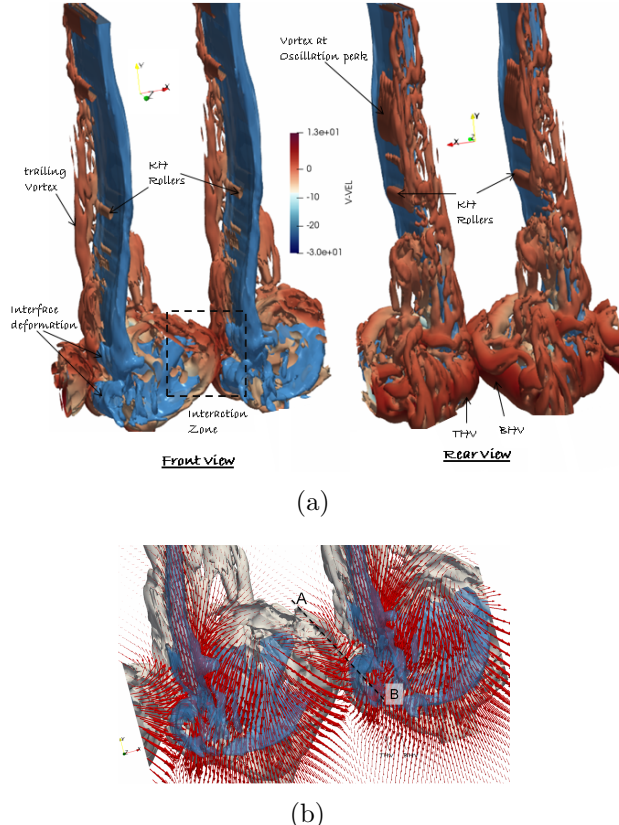


Figure 5.7: Oscillating tandem jets (blue) having nozzle spacing  $9h_0$  with their a) fundamental vortical structures ( $Q = 0.05$ ) and b) enlarged view of the interaction zone (vortical structures in white) depicting the velocity vectors (red) at  $t^* = 18.25$ .

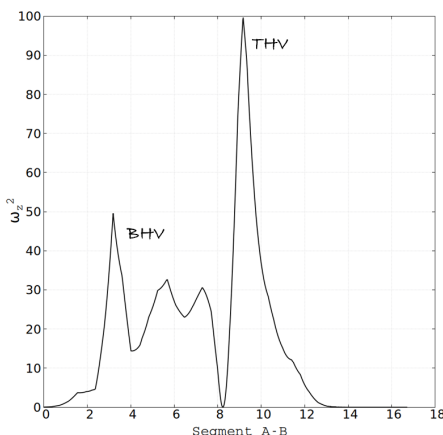


Figure 5.8: Enstrophy values along a segment  $A-B$  (Fig. 5.7(b)) placed between the interacting vortices.

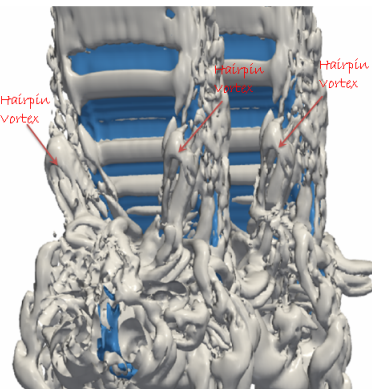


Figure 5.9: Formation of hairpin vortices due to the interaction of THV and BHV in  $9h_0$  nozzle spacing configuration at  $t^* = 20.25$ .

Fig. 5.10(a) demonstrates change in the point of interaction for different nozzle spacings and it is observed that this interaction is delayed as the spacing increases. Thus, for greater nozzle spacing, each jet loses most of its kinetic energy to the surrounding fluid before interacting with each other. Thus, vortex interaction are weak as compared to the smaller nozzle spacing configuration as discussed earlier. The time-averaged normalized stream-wise mass entrainment ( $\langle M/M_0 \rangle_T$ ) for the different nozzle spacings is demonstrated in Fig. 5.10(b) using Equation 5.3, such that,  $\langle M_0 \rangle_T$  is the time-averaged inlet mass flux.

$$\langle M \rangle_T = \int_x \int_z \langle \rho^* v^* \rangle_T dx dz \quad (5.3)$$

Thus, as the oscillation amplitude for small nozzle spacing increases the interaction between the phases increase and results in the increased entrainment of the surrounding fluid.

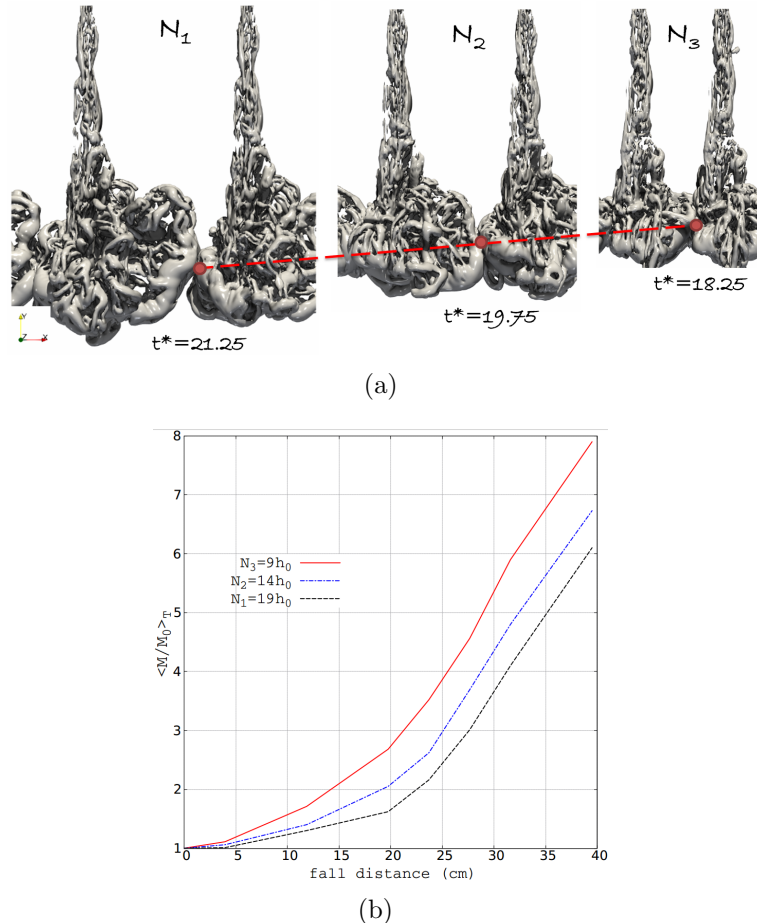


Figure 5.10: Comparison of a) vortex interaction point and b) normalized time averaged mass entrainment for different nozzle spacing.

## 5.2 Asynchronous Tandem Jets

### 5.2.1 Development of Asynchronous Jets

Fig. 5.11 demonstrates the comparison between development of asynchronous oscillating jets for varying nozzle spacings. It is observed that, similar to synchronous jets the asynchronous jets also interact during the formation of upward plume at the jet front caused by RT instability (refer  $t^* = 18.75$ ) at the least nozzle spacing configuration. Unlike synchronous jets, where the interaction occurs between bottom and top lobe; an interaction of asynchronous jets occur between the bottom lobes that are forming an upward liquid plume. The second site of interaction in the  $N_3$  spacing is at the downstream end of the domain (refer  $t^* = 27.25$ ) which occurs due to the growth in oscillation amplitude of these jets. Moreover, these interactions are not observed to occur for nozzle spacing  $N_1$  and  $N_2$ .

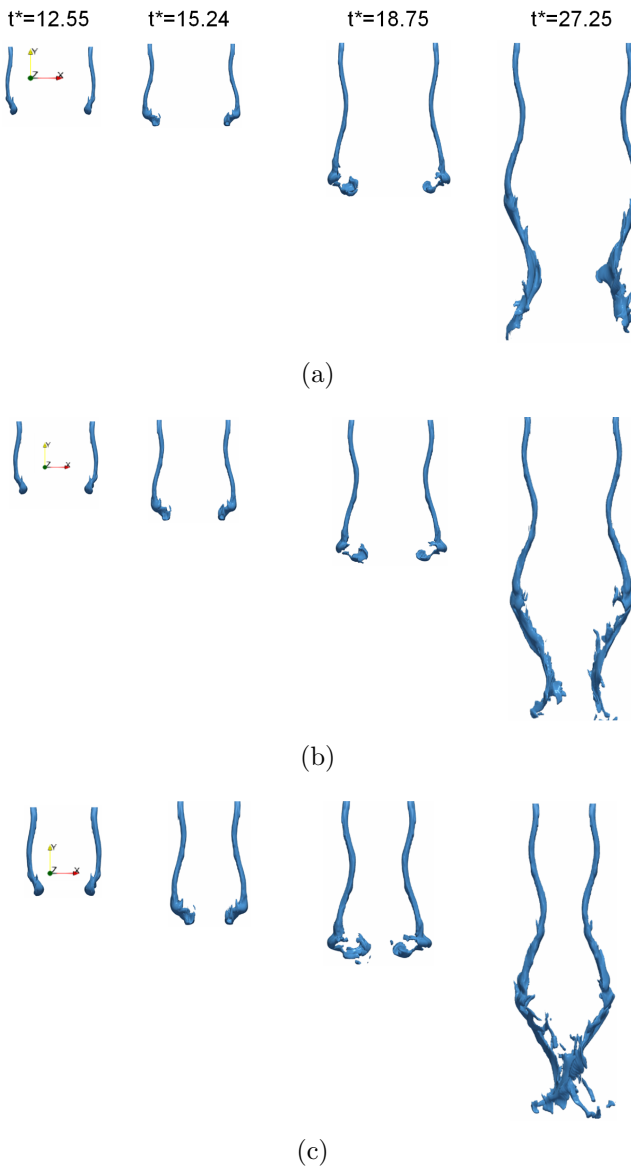


Figure 5.11: Development of *asynchronous* tandem oscillating jets for nozzle spacing a)  $N_1 = 19h_0$ , b)  $N_2 = 14h_0$  and c)  $N_3 = 9h_0$ .

Fig. 5.12 demonstrates the development of phase average velocity profiles in the asynchronous oscillating jets for varying nozzle spacing. The phase averaging as in <sup>129</sup> is performed by dividing the oscillation period into four phase angles which resulted into 18 simulation files per phase angle. Moreover, the procedure for phase averaging is provided in Appendix B. In the near field ( $y^* > 95$ ), the development of jets velocity profiles is not affected significantly. As the two jets move away from each other ( $y^* = 95$ ), the shear layer in the space between the two jets is stretched which causes the merger of the two velocity profiles. Moreover, the fluid between these jets is observed to be accelerated more as the nozzle spacing decreases. Hence, as compared to the synchronous configuration the merging of velocity profiles occurs much earlier in asynchronous jets. Therefore, the converging region in these jets is shifted more towards the upstream. On the other hand, as these jets approach each other, the velocity profile between the two jets become flatter denoting that the accelerated fluid from the previous cycle is decelerated. Furthermore, at the downstream end, both the velocity profiles interact and form a combined flow. Similar to the synchronous jets, asynchronous jets also demonstrate increased interaction with decrease in nozzle spacing.

### 5.2.2 Stability of Asynchronous Jets

Oscillation amplitude of increases as the asynchronous jets travel downstream. Fig. 5.13 demonstrates the comparison of non-dimensional growth rate ( $A_e/A_0$ ) for synchronous and asynchronous tandem jets at varying nozzle spacings. It is observed that as the nozzle spacing decreases the growth rate increases for the asynchronous jets. This increase in growth rate is owing to an increased intensity of vortex rotation at jet peaks. Moreover, it is also observed that for the nozzle spacing  $9h_0$  the growth rate saturates at downstream ( $y^* \sim 39$ ) due to interaction of both jets. Fig. 5.13 also demonstrates that the growth rate for asynchronous jets is greater than synchronous jets due to the decrease in spacing between both jets at the downstream causing increased intensity of vortex rotation.

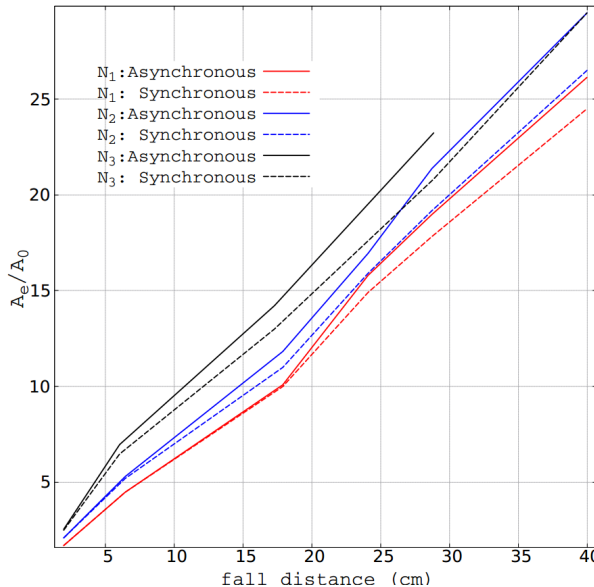


Figure 5.13: Comparison between growth of oscillation amplitudes ( $A_e/A_0$ ) associated with *synchronous* tandem oscillating jets at different nozzle spacing.

Fig. 5.14 demonstrates the variation of enstrophy ( $\omega_z^2$ ) values at  $y^*$  locations of 95,

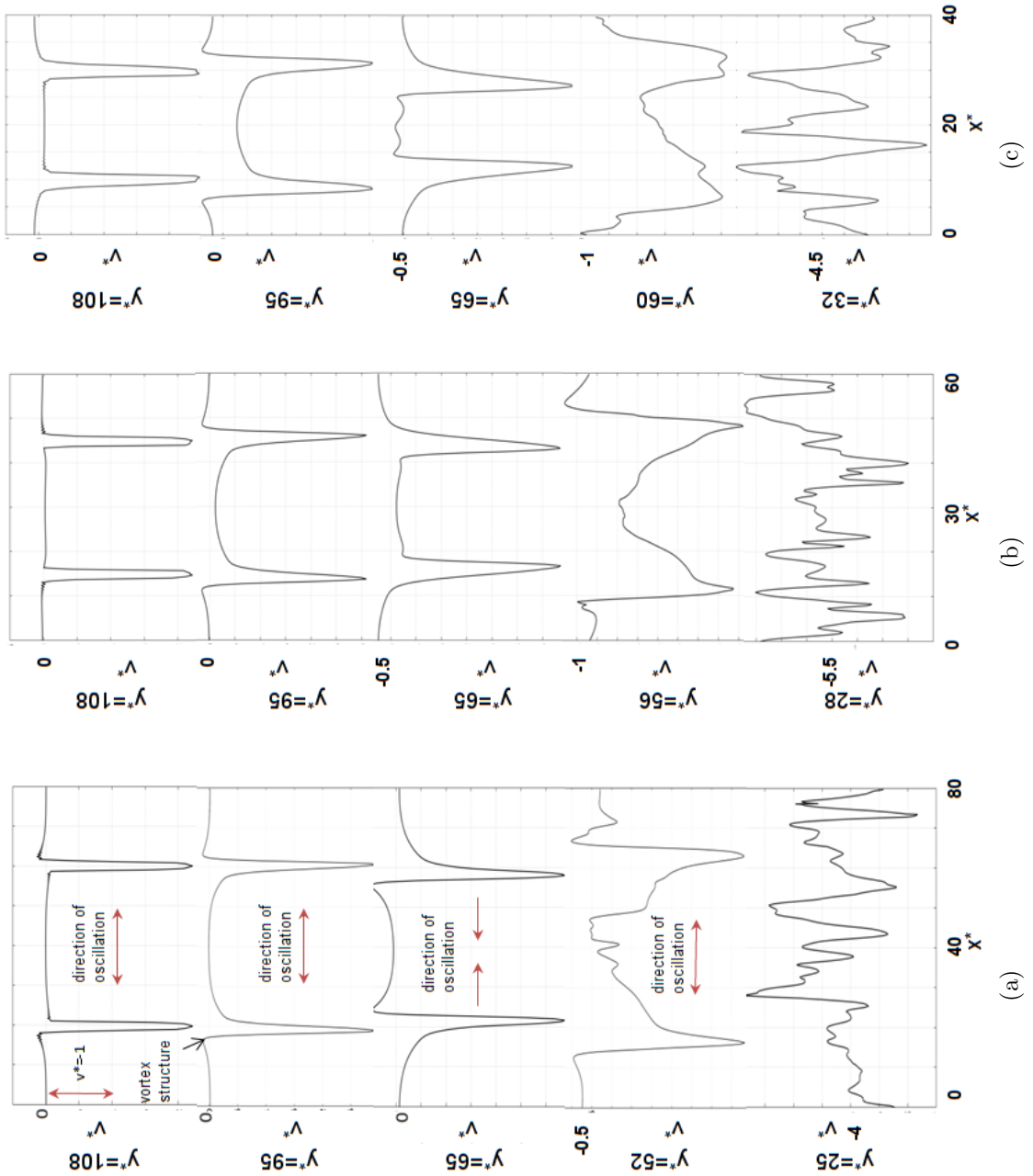


Figure 5.12: Phase averaged<sup>129</sup> velocity profiles of *asynchronous* tandem oscillating jets in the stream-wise direction for nozzle spacing a)  $N_1 = 19h_0$ , b)  $N_2 = 14h_0$  and c)  $N_3 = 9h_0$  at  $z^* = 40$ .

45 and 25 for different nozzle spacings. It is observed that intensity of vortex rotation at the jet peaks increases as the jet descends into the domain and also with decrease in the nozzle spacing. This increased enstrophy justifies the growth in oscillation amplitude in asynchronous jets when nozzle spacing decreases. Moreover, an increased growth rate observed for the asynchronous jets over synchronous jets as discussed earlier is also observed to be due to increased enstrophy values as compared to synchronous jets.

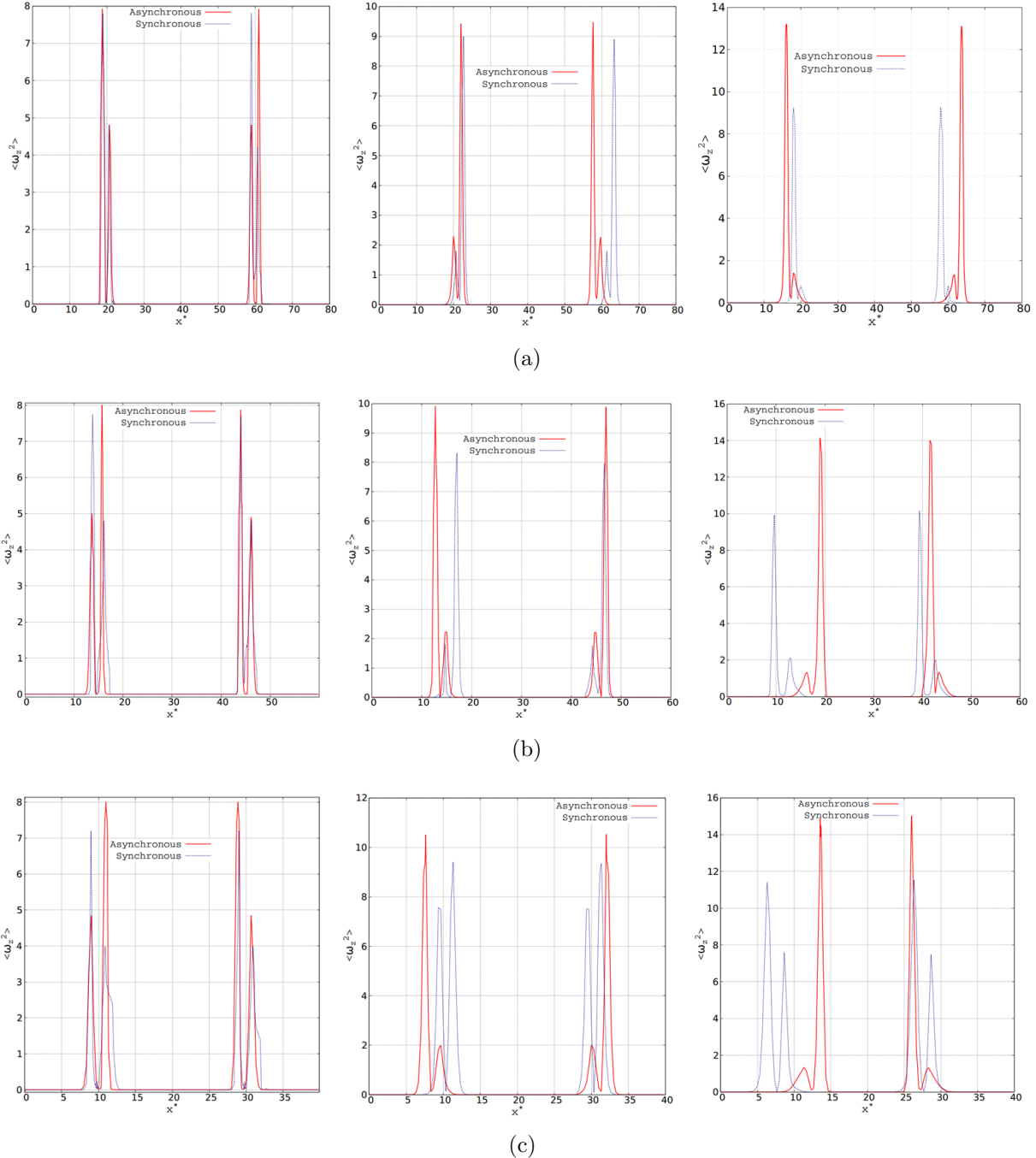


Figure 5.14: Enstrophy values for *asynchronous* tandem oscillating jets along  $x$  – axis with  $z^* = 40$  at  $y^* = 95$ ,  $y^* = 45$  and  $y^* = 25$  (from left) for nozzle spacing a)  $N_1 = 19h_0$ , b)  $N_2 = 14h_0$  and c)  $N_3 = 9h_0$ .

### 5.2.3 Interaction of Coherent Structures in Asynchronous Jets

The development of coherent structures for each jet in asynchronous tandem configuration is similar to that of single oscillating jet structures as discussed in Chapter 4 until these coherent structures interact at downstream end of the domain. This interaction as observed for synchronous jets occurs during the upward plume formation (RT instability) at the jet front. Therefore, an interaction between the two BHVs of asynchronous jets occurs; unlike synchronous jets where a THV and BHV of each jet interacts. Fig. 5.15 demonstrates the nature of vortex interaction at the jet front and the fundamental coherent structures of asynchronous tandem jets. It is observed that the two counter-rotating BHVs draw the surrounding fluid in the space between two jets, which is evident from the velocity vectors (red) demonstrated in Fig. 5.15. This drawn fluid deforms the bottom rollers in the middle causing a merger of the BHVs at their ends and leads to the formation of vortex ring (dashed red line in Fig. 5.15) at the jet front. This vortex ring formation is similar to the *crow's instability*<sup>132</sup>. As discussed earlier this interaction of BHVs is not observed in the asynchronous jets with nozzle spacing configuration of  $14h_0$  and  $19h_0$ .

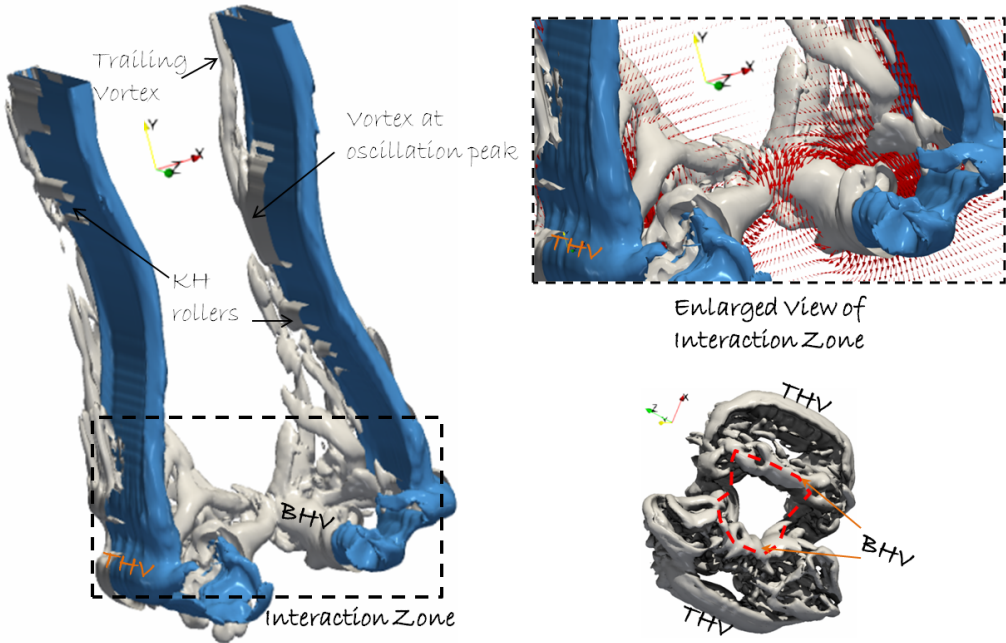


Figure 5.15: Asynchronous oscillating tandem jets (blue) having nozzle spacing  $9h_0$  with their vortical structures ( $Q = 0.05$ ) (white) sliced at  $z^* = 40$  and an enlarged view of the interaction zone depicting the velocity vectors (red) scaled by factor of 0.5.

Fig. 5.16 demonstrates the vortex staggering mechanism occurring at the jet front when the vortex structures interact. It is observed that, initially symmetric bottom lobes start interacting due to the RT instability causing them form an upward plume. As the counter-rotating vortical structures associated with these bottom lobes interact the surrounding fluid is drawn upwards into space between them. Furthermore, the right bottom vortex is staggered and pushed downwards by the left vortex due to an increased interaction between them at the downstream<sup>133</sup>. This staggering process also causes the drawn surrounding fluid to be directed towards right jet. This results in the bottom lobe to curl-up and interact with the inner surface of the right jet. Hence, the typical leapfrogging

process observed at the jet front in the single jet (refer Chapter 4) is accelerated in tandem configuration. On the other hand, at the left jet front this process becomes subdued as the left bottom lobe is pulled towards the right jet as observed from Fig. 5.16. Therefore, asymmetric vortex structures are developed in this configuration as observed in Fig. 5.17. The coherent structures for the right jet lead the structures of left jet as the front of the right jet is pushed downstream. Further downstream the THVs of both jets also interact at the extremes of  $x - axis$ .

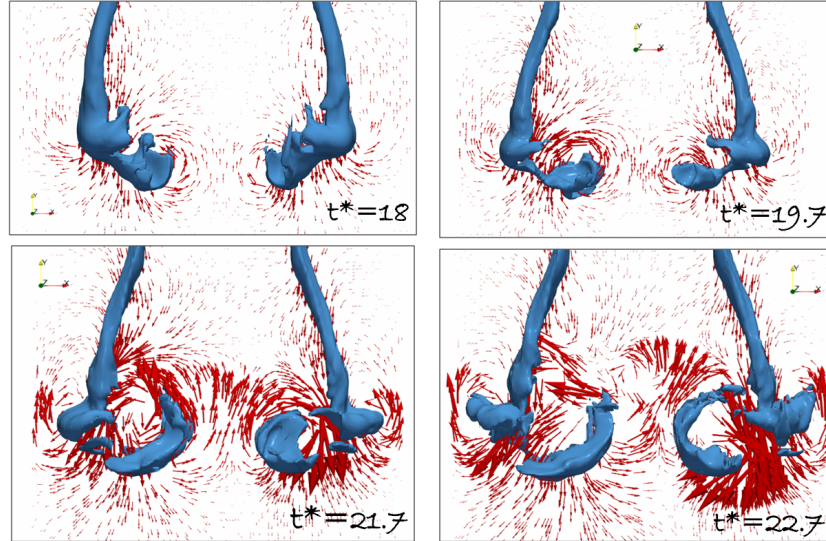


Figure 5.16: Asynchronous oscillating tandem jets (blue) for nozzle spacing  $9h_0$  with the velocity vectors (red) scaled by factor of 0.5 depicting the staggering of jet fronts.

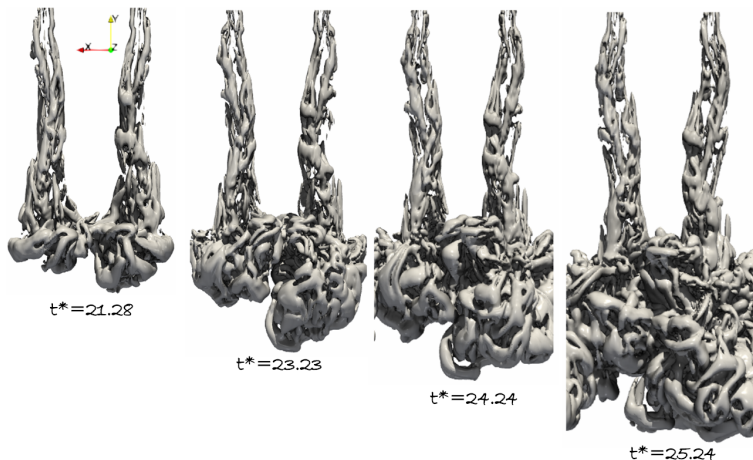


Figure 5.17: Development of vortical structures ( $Q = 0.05$ ) in asynchronous jets with nozzle spacing of  $9h_0$ .

Similar to synchronous tandem jets, an interaction between coherent structures of the asynchronous jets occurs earlier when the nozzle spacing decreases. Fig. 5.18 demonstrates the normalized time averaged stream-wise fluid entrainment for asynchronous jets at varying nozzle spacing. Therefore, it is observed that as the nozzle spacing decreases the entrainment of the surrounding fluid increases. This is owing to the increased growth rate oscillation amplitude and early interaction between the two jets when the nozzle

spacing is decreased. Moreover, the entrainment observed for the asynchronous configuration is greater than that of the synchronous jet configuration. This is due to greater amplitude of oscillation and early upstream interactions between the two jets.

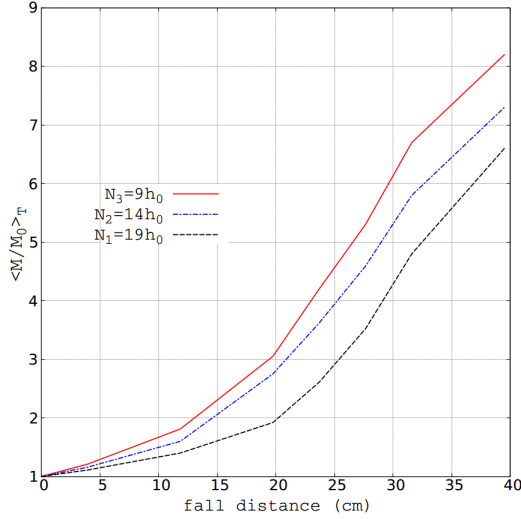


Figure 5.18: Comparison of normalized time averaged stream-wise mass entrainment in asynchronous jets for different nozzle spacing.

### 5.3 Closure

The behaviour of synchronous and asynchronous tandem oscillating jets and an effect of nozzle spacing on them is numerically investigated. The development of these jets, instability associated with them and interaction between the vortical structures is analysed.

It is demonstrated that the fundamental flow features of the jets remain similar to that of the single oscillating jet. The study of velocity profiles suggests that, in the near field (convergent region), development of both synchronous and asynchronous jets is independent of the nozzle spacing and the interaction of these jets is more prominent for nozzle spacing  $9h_0$  at the downstream end. It is also observed that, there exist a linear relationship between the nozzle spacing and merging point where, the merging point shifts towards the upstream end when nozzle spacing decreases. Moreover, the growth rate of oscillation amplitude is found to increase with decrease in the nozzle spacing. This behaviour is observed owing to an increased intensity of vortex rotation at the jet peaks which promotes the instability. Furthermore, stream-wise entrainment in tandem jets increases with decrease in the nozzle spacing and the interaction between coherent structures is more dominant for nozzle spacing  $9h_0$ .

Synchronous oscillating tandem jets are found to be more stable than asynchronous jets as spacing between the two jets for asynchronous jets decreases at the downstream which increase the relative velocity at the interface that promotes instability. Moreover, for asynchronous jets the merging of velocity profiles occurs much earlier than that of synchronous jets due to the nature of their oscillation. Therefore, the stream-wise entrainment of asynchronous jets is observed to be greater than that of the synchronous jets. It is also demonstrated that, interactions of coherent structures in synchronous jets occurs between THV and BHV of each jet whereas, in asynchronous jets the BHV of each jet interacts, which results in a staggered vortex front when nozzle spacing decreases.

This page intentionally left blank.

---

## CHAPTER 6

---

# CONTRIBUTIONS AND RECOMMENDATIONS

Present study numerically investigates the fundamental behaviour of the oscillating liquid jets in a quiescent atmosphere. Analysis involves the instability associated with these jets and the effect of flow properties on it. Moreover, the coherent structures of oscillating jet and effect of viscosity on them is also investigated. Furthermore, the behaviour of oscillating jets in tandem configuration and the effect of nozzle spacing on them is also reported here.

### 6.1 Contribution to the Existing Literature

1. The algebraic VOF methods are prone to diffusive errors<sup>77</sup> which may lead to inaccurate definition of fluid interface. Thus, present study introduces an accurate, sharp and computationally efficient algebraic VOF method *SAISH*.
2. The exact reason behind an increase in oscillation amplitude of the sweeping jets was not identified in the previous literature. The present numerical analysis established that, the instability associated with the amplitude of oscillation is owing to the formation of low pressure region at their oscillation peaks. This low pressure region is a result of vortical structure present at this location. The intensity of rotation (enstrophy) of these vortices increases downstream due to an increased jet velocity.
3. The literature consist of the analytical results that investigate the effect of flow properties such as viscosity and surface tension on the sinuous instability. The present numerical results support these findings that surface tension and viscosity stabilize the oscillations in these jets and also provides the primary breakup mechanism for these oscillating jets under the influence of these properties which was not reported previously.
4. The present study also contributes to the existing literature by comparing the effect of parabolic and uniform inlet velocity profiles on the stability of these jets. The parabolic inlet velocity profile provides more stable oscillations as compared to the uniform velocity profile. Moreover, an increase in the gravitational force is found to amplify the oscillation amplitude, whereas, further increase in its value dampens these oscillation as surface tension forces become dominant at the jet peaks.

5. To the best of authors' knowledge there is no study that investigates the coherent structures in an oscillating jet. Therefore, coherent structures in the form of *head vortices*, *oscillation peak vortices* and *side hairpin vortices* are identified here and are found to be the dominant structures responsible for fluid entrainment and this dominance is confirmed by the POD and DMD analysis. Moreover, BHV and THV are found to substantially contribute towards the jet spreading and energy dissipation as they undergo leapfrogging process at the jet front. Furthermore, the effect of fluid viscosity on these structures is studied and found to dampen the formation and evolution of these coherent structures. As a result, highly viscous oscillating jets demonstrate lower entrainment.
6. Present study also provides an analysis of the synchronous and asynchronous oscillating jets in tandem. Development of the jets in both configurations, instability associated with their oscillations and an interaction between the jets is numerically analysed. Moreover, the effect of nozzle spacing on these characteristics of dual jets is also reported. A dominant form of interaction between these jets occur at the jet front formed as a result of RT instability. Moreover it is demonstrated that, oscillation amplitude of these jets is augmented if the nozzle spacing is reduced.

## 6.2 Recommendations

1. The present study considers the jet to be planar. In future, circular and elliptic nozzle cross-sections can be used and compared for oscillating jets. These, nozzle configurations are of great importance to understand the entrainment in supersonic jets.
2. Initially, the gas phase in the domain for the present study is considered to be quiescent. Therefore, this study can be extended by having an active gas phase such that an annular gas and liquid flow occurs. Such flow configuration is important for air-blast atomizers and metal powder formation. Thus, study of gas phase on these jets can provide more insights into the capabilities of oscillating jets.
3. The literature for oscillating jet including the present study has considered the oscillations to be linear where crest and troughs have similar amplitudes. The non-linear inlet perturbations can be provided to enhance the atomization and an interesting flow field can be obtained which can aid to mixing processes in several applications.
4. A single axis perturbation is considered generally for oscillating jets which account for an existence of single fluidic oscillator. If two or three axis perturbations at the inlet are provided, then, that will require the unification of two to three *fluidic oscillators*. Such flow field can be of interest for fundamental fluid dynamics studies to being with.

# ASSOCIATED PUBLICATIONS

---

## Journal Publications:

1. Arote, Ashish, Mukund Bade, and Jyotirmay Banerjee. 2021. "Behavior of Synchronous and Asynchronous Spatially Oscillating Planar Liquid Jets in Tandem." *Physics of Fluids* 33(5): 052102. <https://doi.org/10.1063/5.0046990>
2. Arote, Ashish, Mukund Bade, and Jyotirmay Banerjee. 2021. "Properties of Blended Advection Schemes for Hyperbolic Conservation Laws." *Sādhanā* 46(70). <https://doi.org/10.1007/s12046-021-01609-0>
3. Arote, Ashish, Mukund Bade, and Jyotirmay Banerjee. 2020. "On Coherent Structures of Spatially Oscillating Planar Liquid Jet Developing in a Quiescent Atmosphere." *Physics of Fluids* 32(8): 082111. <https://doi.org/10.1063/5.0016480> (Editor's Pick)
4. Arote, Ashish, Mukund Bade, and Jyotirmay Banerjee. 2020. "An Improved Compressive Volume of Fluid Scheme for Capturing Sharp Interfaces Using Hybridization." *Numerical Heat Transfer, Part B: Fundamentals* 79(1): 2953. <https://www.tandfonline.com/doi/full/10.1080/10407790.2020.1793543>
5. Arote, Ashish, Mukund Bade, and Jyotirmay Banerjee. 2019. "Numerical Investigations on Stability of the Spatially Oscillating Planar Two-Phase Liquid Jet in a Quiescent Atmosphere." *Physics of Fluids* 31(11): 112103. <http://aip.scitation.org/doi/10.1063/1.5123762>

## Conference Proceedings:

1. Arote, Ashish, Mukund Bade, and Jyotirmay Banerjee. 2020. "Numerical Investigations into Effect of Confinement on Oscillating Planar Liquid Jet." In *International Conference on Applications in Computational Engineering & Sciences 2020*, VIT, Vellore, 23-32. <https://iopscience.iop.org/article/10.1088/1757-899X/1128/1/012032>
2. Arote, Ashish, Mukund Bade, and Jyotirmay Banerjee. 2020. "Comparative Study of the Fluid Interface Capturing High Resolution Algebraic Schemes." In *2<sup>nd</sup> International Conference on Future Learning Aspects of Mechanical Engineering 2020*, Amity Uni. Noida, UP, 1-8. [https://link.springer.com/10.1007/978-981-16-0159-0\\_3](https://link.springer.com/10.1007/978-981-16-0159-0_3)
3. Jha, Rahul, Ashish Arote, and Jyotirmay Banerjee. 2019. "Advection Stabilization Using Lower Order Scheme Blending: A Case Study of Rayleigh Taylor Instability." In *Fluid Mechanics and Fluid Power 2019*, PSG Coimbatore: FMFP 2019. <https://www.springer.com/gp/book/9789811606977>

*This page intentionally left blank.*

---

---

## APPENDIX A

---

# ALGORITHM FOR ESTIMATING DOMINANT COHERENT MODES

---

**Algorithm 0:** Summary of the standard DMD algorithm

---

- 1: **procedure** (1) FORMATION DATA MARTICES
  - 2:      $A = [V_0 \dots V_{n-1}]$  and  $A_1 = [V_1 \dots V_n]$ , where  $n$  is no. of time intervals and  $m$  is no. of spatial cells
  - 3: **procedure** (2) COMPUTE SVD OF  $A$
  - 4:      $A = U\Sigma V^*$
  - 5:     where,  $U$  is  $m \times r$ ,  $\Sigma$  is  $r \times r$ ,  $V$  is  $n \times r$  and  $r$  is rank of  $A$
  - 6: **procedure** (3) DEFINE  $\hat{A}$  MATRIX
  - 7:      $\hat{A} = U^* A_1 V \Sigma^{-1}$ , we are finding a relation  $A = \hat{A} A_1$
  - 8: **procedure** (4) COMPUTE EIGENVALUES AND EIGENVECTORS OF  $\hat{A}$
  - 9:      $\hat{A}w = \lambda w$ , where  $\lambda$  and  $w$  serve as *eigenvalue* and *eigenvector* of  $\hat{A}$
  - 10: **procedure** (5) COMPUTE DMD MODES
  - 11:      $\Phi = Uw$
- 

**Algorithm 1:** Summary of the standard POD algorithm

---

- 1: **procedure** (1) FORMATION DATA MARTIX
  - 2:      $A = [V_0 \dots V_n]$ , where  $n$  is no. of time intervals and  $m$  is no. of spatial cells
  - 3: **procedure** (2) COMPUTE SVD OF  $A$
  - 4:      $A = U\Sigma V^*$
  - 5:     where,  $U$  is  $m \times r$ ,  $\Sigma$  is  $r \times r$ ,  $V$  is  $n \times r$  and  $r$  is rank of  $A$
  - 6: **procedure** (5) COMPUTE POD MODES
  - 7:      $\Phi = U$
-

*This page intentionally left blank.*

---

---

## APPENDIX B

---

# PHASE AVERAGING OF VELOCITY FIELD

The algorithm used for carrying out the phase averaging for velocity is as follows,

---

**Algorithm 1:** Summary of the standard phase averaging

---

- 1: **procedure** (1) IDENTIFY THE PERIOD OF OSCILLATION ( $T$ )
  - 2:      $T = \frac{1}{St}$ , where  $St$  is the Strouhal number used for the study
  - 3: **procedure** (2) DEFINE THE NUMBER OF PHASE ANGLES ( $n$ ) TO OBTAIN PHASE ANGLE ( $T/n$ )
  - 4: **procedure** (3) READ THE SIMULATION FILES FOR THE PARTICULAR PHASE ANGLE FOR VELOCITY DATA
  - 5: **procedure** (4) SELECT THE VERTICAL LOCATION  $y^*$
  - 6: **procedure** (5) PERFORM THE VELOCITY AVERAGING
-

*This page intentionally left blank.*

---

## BIBLIOGRAPHY

- [1] F. Ostermann, R. Woszidlo, C. N. Nayeri, and C. O. Paschereit, “Properties of a sweeping jet emitted from a fluidic oscillator,” *Journal of Fluid Mechanics*, vol. 857, pp. 216–238, 2018.
- [2] B. C. Bobusch, P. Berndt, C. O. Paschereit, and R. Klein, “Investigation of fluidic devices for mixing enhancement for the shockless explosion combustion process,” in *Active Flow and Combustion Control 2014* (R. King, ed.), (Cham), pp. 281–297, Springer International Publishing, 2015.
- [3] G. Mon, “Pulsatile impinging cooling system for electronic ic modules and systems using fluidic oscillators,” Mar. 2 1993. US Patent 5,190,099.
- [4] T. G. Sutton, “Fluidic feedback-controlled liquid cooling module,” Sept. 29 1998. US Patent 5,815,370.
- [5] S. Raghu, “Fluidic oscillators for flow control,” *Experiments in Fluids*, vol. 54, p. 1455, Jan 2013.
- [6] L. Shigang, X. Dailiang, and T. Shan, “Design and simulation of fluidic flowmeter for the measurement of liquid flow in microchannel,” in *2012 Third International Conference on Digital Manufacturing Automation*, pp. 310–313, July 2012.
- [7] F. Cascetta and P. Vigo, “The future domestic gas meter: Review of current developments,” *Measurement*, vol. 13, no. 2, pp. 129 – 145, 1994.
- [8] V. Tesa, “Oscillator micromixer,” *Chemical Engineering Journal*, vol. 155, no. 3, pp. 789 – 799, 2009.
- [9] H. B. Squire, “Investigation of the instability of a moving liquid film,” *British Journal of Applied Physics*, vol. 4, no. 6, pp. 167–169, 1953.
- [10] J. F. Shea and W. Hagerty, “A study of the stability of plane fluid sheets,” *J. Appl. Mech*, vol. 22, p. 509, 1955.
- [11] C. J. Clark and N. Dombrowski, “Aerodynamic Instability and Disintegration of Inviscid Liquid Sheets,” *Proceedings of the Royal Society A: Mathematical, Physical and Engineering Sciences*, vol. 329, no. 1579, pp. 467–478, 1972.
- [12] H. R. Asare, R. K. Takahashi, and M. A. Hoffman, “Liquid Sheet Jet Experiments: Comparison With Linear Theory,” *Journal of Fluids Engineering*, vol. 103, no. 4, p. 595, 1981.
- [13] X. Li, “On the instability of plane liquid sheets in two gas streams of unequal velocities,” *Acta Mechanica*, vol. 106, no. 3-4, pp. 137–156, 1994.
- [14] P. J. Schmid and D. S. Henningson, “On the stability of a falling liquid curtain,” *Journal of Fluid Mechanics*, vol. 463, pp. 163–171, 2002.
- [15] O. Tammisola, A. Sasaki, F. Lundell, M. Matsubara, and L. D. Söderberg, “Stabilizing effect of surrounding gas flow on a plane liquid sheet,” *Journal of Fluid Mechanics*, vol. 672, pp. 5–32, 2011.
- [16] S. J. Rees and M. P. Juniper, “The effect of surface tension on the stability of unconfined and confined planar jets and wakes,” *Journal of Fluid Mechanics*, vol. 633, pp. 71–97, 2009.

- [17] V. N. Rao and K. Ramamurthi, "Internal instability of thin liquid sheets," *Physics of Fluids*, vol. 21, no. 9, 2009.
- [18] L. Soderberg and P. Alfredsson, "Experimental and theoretical stability investigations of plane liquid jets," *European Journal of Mechanics - B/Fluids*, vol. 17, no. 5, pp. 689 – 737, 1998.
- [19] E. López-Pagés, C. Dopazo, and N. Fueyo, "Very-near-field dynamics in the injection of two-dimensional gas jets and thin liquid sheets between two parallel high-speed gas streams," *Journal of Fluid Mechanics*, vol. 515, pp. 1–31, 2004.
- [20] A. Lozano, A. García-Olivares, and C. Dopazo, "The instability growth leading to a liquid sheet breakup," *Physics of Fluids*, vol. 10, no. 9, pp. 2188–2197, 1998.
- [21] H. Desjardins, Olivier, Pitsch, "Detailed Numerical Investigation of Turbulent Atomization of Liquid Jets," *Atomization and Sprays*, vol. 20, no. 4, pp. 311–336, 2010.
- [22] M. Klein, "Direct numerical simulation of a spatially developing water sheet at moderate Reynolds number," *International Journal of Heat and Fluid Flow*, vol. 26, no. 5, pp. 722–731, 2005.
- [23] R. Scardovelli and S. Zaleski, "Direct Numerical Simulation of Free-Surface and Interfacial Flow," *Annual Review of Fluid Mechanics*, vol. 31, no. 1, pp. 567–603, 1999.
- [24] S. Schmidt, O. Krüger, K. Göckeler, and C. O. Paschereit, "Numerical investigation of the breakup behavior of an oscillating two-phase jet," *Physics of Fluids*, vol. 30, no. 7, 2018.
- [25] A. K. Hussain, "Coherent structures - Reality and myth," *Physics of Fluids*, vol. 26, no. 10, pp. 2816–2850, 1983.
- [26] F. F. Grinstein, "Entrainment, axis switching, and aspect-ratio effects in rectangular free jets," *4th Shear Flow Control Conference*, 1997.
- [27] F. F. Grinstein, "Vortex dynamics and entrainment in rectangular free jets," *Journal of Fluid Mechanics*, vol. 437, pp. 69–101, 2001.
- [28] L. Wang, L. H. Feng, and Y. Xu, "Laminar-to-transitional evolution of three-dimensional vortical structures in a low-aspect-ratio rectangular synthetic jet," *Experimental Thermal and Fluid Science*, vol. 104, no. February, pp. 129–140, 2019.
- [29] F. F. Grinstein and C. R. DeVore, "Dynamics of coherent structures and transition to turbulence in free square jets," *Physics of Fluids*, vol. 8, no. 5, pp. 1237–1251, 1996.
- [30] J. Hart, J. Naser, and P. J. Witt, "Coherent structure dynamics in jets from irregular shaped nozzles," *Fifteenth Australasian Fluid Mechanics Conference, AFMC15*, no. December, 2004.
- [31] Y. Tsuchiya and C. Horikoshi, "On the spread of rectangular jets," *Experiments in Fluids*, vol. 4, no. 4, pp. 197–204, 1986.
- [32] Y. TSUCHIYA, C. HORIKOSHI, T. SATO, and M. TAKAHASHI, "A study on the spread of rectangular jets (the mixing layer near the jet exit and visualization by the dye method)," *JSME international journal. Ser. 2, Fluids engineering, heat transfer, power, combustion, thermophysical properties*, vol. 32, no. 1, pp. 11–18, 1989.
- [33] W. Quinn, "Turbulent free jet flows issuing from sharp-edged rectangular slots: The influence of slot aspect ratio," *Experimental Thermal and Fluid Science*, vol. 5, no. 2, pp. 203 – 215, 1992.
- [34] P. R. Suresh, K. Srinivasan, T. Sundararajan, and S. K. Das, "Reynolds number dependence of plane jet development in the transitional regime," *Physics of Fluids*, vol. 20, no. 4, 2008.
- [35] O. Desjardins and H. Pitsch, "Detailed numerical investigation of turbulent atomization of liquid jets," *Atomization and Sprays*, vol. 20, no. 4, pp. 311–336, 2010.

- [36] K. Bremhorst and P. G. Hollis, "Velocity field of an axisymmetric pulsed, subsonic air jet," *AIAA Journal*, vol. 28, no. 12, pp. 2043–2049, 1990.
- [37] J. M. Simmons, M. F. Platzer, and T. C. Smith, "Velocity measurements in an oscillating plane jet issuing into a moving air stream," *Journal of Fluid Mechanics*, vol. 84, no. 1, p. 3353, 1978.
- [38] S. C. Galea and J. M. Simmons, "Excitation of a plane jet by periodic perturbation of the nozzle area," *8th Australasian Fluid Mechanics Conference*, 1983.
- [39] R. B. Farrington and S. D. Claunch, "Infrared imaging of large-amplitude, low-frequency disturbances on a planar jet," *AIAA Journal*, vol. 32, no. 2, pp. 317–323, 1994.
- [40] S. Iio, K. Takahashi, Y. Haneda, and T. Ikeda, "Flow visualization of vortex structure in a pulsed rectangular jet," *Journal of Visualization*, vol. 11, no. 2, pp. 125–132, 2008.
- [41] F. B. Hsiao and J. M. Huang, "On the dynamics of flow structure development in an excited plane jet," *Journal of Fluids Engineering, Transactions of the ASME*, vol. 116, no. 4, pp. 714–720, 1994.
- [42] F. Ostermann, R. Woszidlo, C. N. Nayeri, and C. O. Paschereit, "Properties of a sweeping jet emitted from a fluidic oscillator," *Journal of Fluid Mechanics*, vol. 857, pp. 216–238, 2018.
- [43] O. Tammisola, A. Sasaki, F. Lundell, M. Matsubara, and L. D. Söderberg, "Stabilizing effect of surrounding gas flow on a plane liquid sheet," *Journal of Fluid Mechanics*, vol. 672, pp. 5–32, 2011.
- [44] J. Mi, G. J. Nathan, and R. E. Luxton, "Dynamic oscillation of quasi-planar jet," *12th Australasian Fluid Mechanics Conference*, no. December, 1995.
- [45] M. Riese, G. J. Nathan, and R. M. Kelso, "Preliminary Identification of Flow Regimes in a Mechanically Oscillated Planar Jet," in *15th Australasian Fluid Mechanics Conference*, no. December, pp. 17–20, 2004.
- [46] B. D. R. Miller and E. W. Comings, "Force-momentum fields in a dual-jet flow," *Journal of Fluid Mechanics*, vol. 7, no. 02, pp. 237 – 256, 1959.
- [47] E. Tanaka, "The Interference of Two-Dimensional Parallel Jets: 1st Report, Experiments on Dual Jet," *Bulletin of the JSME*, vol. 13, no. 56, pp. 364–370, 1970.
- [48] E. Tanaka, "The Interference of Two-Dimensional Parallel Jets: 2nd Report, Experiments on the Combined Flow of Dual Jet," *Bulletin of the JSME*, vol. 17, no. 109, 1972.
- [49] Y. E. Lin and M. J. Sheu, "Investigation of two parallel unventilated jets," *Experiments in Fluids*, vol. 10, pp. 17–22, 1990.
- [50] Y. F. Lin and M. J. Sheu, "Interaction of parallel turbulent plane jets," *AIAA Journal*, vol. 29, no. 9, pp. 1372–1373, 1991.
- [51] G. F. Marsters, "Interaction of Two Plane Parallel Jets.,," *Queen's univ Therm Fluid Sci Group Rep*, vol. 15, no. 1, pp. 1756–1763, 1977.
- [52] A. Nasr and J. C. Lai, "Two parallel plane jets: Mean flow and effects of acoustic excitation," *Experiments in Fluids*, vol. 22, no. 3, pp. 251–260, 1997.
- [53] A. Durve, A. W. Patwardhan, I. Banarjee, G. Padmakumar, and G. Vaidyanathan, "Numerical investigation of mixing in parallel jets," *Nuclear Engineering and Design*, vol. 242, pp. 78–90, 2012.
- [54] E. A. Anderson and R. E. Spall, "Experimental and numerical investigation of two-dimensional parallel jets," *Journal of Fluids Engineering, Transactions of the ASME*, vol. 123, no. 2, pp. 401–406, 2001.
- [55] N. Fujisawa, K. Nakamura, and K. Srinivas, "Interaction of two parallel plane jets of different velocities," *Journal of Visualization*, vol. 7, no. 2, pp. 135–142, 2004.

- [56] B. Zang and T. H. New, “Near-field dynamics of parallel twin jets in cross-flow,” *Physics of Fluids*, vol. 29, no. 3, 2017.
- [57] J. C. Lai and A. Nasr, “Two parallel plane jets: Comparison of the performance of three turbulence models,” *Proceedings of the Institution of Mechanical Engineers, Part G: Journal of Aerospace Engineering*, vol. 212, no. 6, pp. 379–391, 1998.
- [58] H. Wang, S. Lee, Y. A. Hassan, and A. E. Ruggles, “Laser-Doppler measurements of the turbulent mixing of two rectangular water jets impinging on a stationary pool,” *International Journal of Heat and Mass Transfer*, vol. 92, pp. 206–227, 2016.
- [59] H. Wang, S. Lee, and Y. A. Hassan, “Particle image velocimetry measurements of the flow in the converging region of two parallel jets,” *Nuclear Engineering and Design*, vol. 306, pp. 89–97, 2016.
- [60] D. Yu, M. S. Ali, and J. H. W. Lee, “Multiple Tandem Jets in Cross-Flow,” *Journal of Hydraulic Engineering*, vol. 132, no. 9, pp. 971–982, 2006.
- [61] K. Zhao, P. N. Okolo, J. Kennedy, and G. J. Bennett, “2D PIV measurement on the interaction zone between two parallel planar jets in a crossflow,” *AIP Advances*, vol. 7, no. 10, 2017.
- [62] K. Zhao, P. N. Okolo, Y. Wang, J. Kennedy, and G. J. Bennett, “An experimental characterization of the interaction between two tandem planar jets in a crossflow,” *Journal of Fluids Engineering, Transactions of the ASME*, vol. 140, no. 11, pp. 1–12, 2018.
- [63] I. G. Y. Kamotani, “Experiments on confined turbulent jets in cross flow,” tech. rep., Case Western Reserve University Cleveland, Ohio, 1973.
- [64] X. Wen, Z. Li, W. Zhou, and Y. Liu, “Interaction of dual sweeping impinging jets at different Reynolds numbers,” *Physics of Fluids*, vol. 30, no. 10, 2018.
- [65] M. N. Tomac and J. W. Gregory, “Phase-synchronized fluidic oscillator pair,” *AIAA Journal*, vol. 57, no. 2, pp. 670–681, 2019.
- [66] M. N. Tomac, “Novel jet impingement atomization by synchronizing the sweeping motion of the fluidic oscillators,” *Journal of Visualization*, vol. 23, no. 3, pp. 373–375, 2020.
- [67] G. Tryggvason, R. Scardovelli, and S. Zaleski, *Direct Numerical Simulations of GasLiquid Multi-phase Flows*. Cambridge University Press, 2011.
- [68] B. Mirjalili, S. S. Jain, and M. Dodd, “Interface-capturing methods for two-phase flows : An overview and recent developments,” *Center for Turbulence Research Annual Research Briefs 2017*, pp. 117–135, 2017.
- [69] C. Hirt and B. Nichols, “Volume of fluid (vof) method for the dynamics of free boundaries,” *Journal of Computational Physics*, vol. 39, no. 1, pp. 201 – 225, 1981.
- [70] M. Rudman, “Volume-tracking methods for interfacial flow calculations,” *International Journal for Numerical Methods in Fluids*, vol. 24, no. 7, pp. 671–691, 1997.
- [71] D. L. Youngs, “Time-dependent multi-material flow with large fluid distortion,” *Numerical Methods for Fluid Dynamics*, pp. 273–285, 1982.
- [72] S. Saincher and J. Banerjee, “A redistribution-based volume-preserving PLIC-VOF technique,” *Numerical Heat Transfer, Part B: Fundamentals*, vol. 67, no. 4, pp. 338–362, 2015.
- [73] J. E. Pilliod and E. G. Puckett, “Second-order accurate volume-of-fluid algorithms for tracking material interfaces,” *Journal of Computational Physics*, vol. 199, no. 2, pp. 465 – 502, 2004.
- [74] W. J. Rider and D. B. Kothe, “Reconstructing volume tracking,” *Journal of Computational Physics*, vol. 141, no. 2, pp. 112 – 152, 1998.

- [75] H. T. Ahn and M. Shashkov, “Adaptive moment-of-fluid method,” *Journal of Computational Physics*, vol. 228, no. 8, pp. 2792 – 2821, 2009.
- [76] M. Raessi and H. Pitsch, “Consistent mass and momentum transport for simulating incompressible interfacial flows with large density ratios using the level set method,” *Computers & Fluids*, vol. 63, pp. 70 – 81, 2012.
- [77] O. Ubbink and R. I. Issa, “A Method for Capturing Sharp Fluid Interfaces on Arbitrary Meshes,” *Journal of Computational Physics*, vol. 153, no. 1, pp. 26–50, 1999.
- [78] P. H. Gaskell and A. K. C. Lau, “Curvaturecompensated convective transport: SMART, A new boundedness preserving transport algorithm,” *International Journal for Numerical Methods in Fluids*, vol. 8, no. 6, pp. 617–641, 1988.
- [79] Y.-y. Tsui, S.-w. Lin, T.-t. Cheng, and T.-c. Wu, “Flux-blending schemes for interface capture in two-fluid flow,” *International Journal of Heat and Mass Transfer*, vol. 52, no. 23-24, pp. 5547–5556, 2009.
- [80] J. K. Patel and G. Natarajan, “A generic framework for design of interface capturing schemes for multi-fluid flows,” *Computers and Fluids*, vol. 106, pp. 108 – 118, 2015.
- [81] D. Zhang, C. Jiang, D. Liang, Z. Chen, and Y. Yang, “A refined volume-of-fluid algorithm for capturing sharp fluid interfaces on arbitrary meshes,” *Journal of Computational Physics*, vol. 274, pp. 709–736, 2014.
- [82] J. E. Fromm, “A method for reducing dispersion in convective difference schemes,” *Journal of Computational Physics*, vol. 3, no. 2, pp. 176 – 189, 1968.
- [83] J. Zhu, “A low-diffusive and oscillation-free convection scheme,” *Communications in Applied Numerical Methods*, vol. 7, no. 3, pp. 225–232, 1991.
- [84] B. Leonard and H. Niknafs, “Sharp monotonic resolution of discontinuities without clipping of narrow extrema,” *Computers and Fluids*, vol. 19, no. 1, pp. 141 – 154, 1991. Special Issue CTAC-89.
- [85] H. Jasak, H. Weller, and A. Gosman, “High resolution nvd differencing scheme for arbitrarily unstructured meshes,” *International Journal for Numerical Methods in Fluids*, vol. 31, no. 2, pp. 431–449, 1999.
- [86] D. Zhang, C. Jiang, D. Liang, and L. Cheng, “A review on tvd schemes and a refined flux-limiter for steady-state calculations,” *Journal of Computational Physics*, vol. 302, pp. 114 – 154, 2015.
- [87] J. A. Heyns, A. G. Malan, T. M. Harms, and O. F. Oxtoby, “Development of a compressive surface capturing formulation for modelling free-surface flow by using the volume-of-fluid approach,” *International Journal for Numerical Methods in Fluids*, vol. 71, no. 6, pp. 788–804, 2013.
- [88] D. J. Harvie and D. F. Fletcher, “A new volume of fluid advection algorithm: The stream scheme,” *Journal of Computational Physics*, vol. 162, no. 1, pp. 1 – 32, 2000.
- [89] S. Saincher and J. Banerjee, “A redistribution-based volume-preservingPLIC-VOF technique,” *Numerical Heat Transfer, Part B: Fundamentals*, vol. 67, no. 4, pp. 338–362, 2015.
- [90] J. C. Martin, W. J. Moyce, W. G. Penney, A. T. Price, and C. K. Thornhill, “Part iv. an experimental study of the collapse of liquid columns on a rigid horizontal plane,” *Philosophical Transactions of the Royal Society of London. Series A, Mathematical and Physical Sciences*, vol. 244, no. 882, pp. 312–324, 1952.
- [91] T. Araki and S. Koshimura, “Numerical modeling of free surface flow by the lattice boltzmann method,” *Journal of Japan Society of Civil Engineers, Ser. B2 (Coastal Engineering)*, vol. 65, no. 1, pp. 56–60, 2009.

- [92] J. Brackbill, D. Kothe, and C. Zemach, “A continuum method for modeling surface tension,” *Journal of Computational Physics*, vol. 100, no. 2, pp. 335 – 354, 1992.
- [93] M. M. Francois, S. J. Cummins, E. D. Dendy, D. B. Kothe, J. M. Sicilian, and M. W. Williams, “A balanced-force algorithm for continuous and sharp interfacial surface tension models within a volume tracking framework,” *Journal of Computational Physics*, vol. 213, no. 1, pp. 141 – 173, 2006.
- [94] J. Brackbill, D. Kothe, and C. Zemach, “A continuum method for modeling surface tension,” *Journal of Computational Physics*, vol. 100, no. 2, pp. 335 – 354, 1992.
- [95] S. Popinet, “Numerical Models of Surface Tension,” *Annual Review of Fluid Mechanics*, vol. 50, no. 1, pp. 49–75, 2017.
- [96] M. M. Francois, S. J. Cummins, E. D. Dendy, D. B. Kothe, J. M. Sicilian, and M. W. Williams, “A balanced-force algorithm for continuous and sharp interfacial surface tension models within a volume tracking framework,” *Journal of Computational Physics*, vol. 213, no. 1, pp. 141 – 173, 2006.
- [97] S. Gottlieb, D. Ketcheson, and C.-W. Shu, *Strong Stability Preserving Runge-Kutta and Multistep Time Discretizations*. WORLD SCIENTIFIC, 2011.
- [98] A. Harten, “High resolution schemes for hyperbolic conservation laws,” *Journal of Computational Physics*, vol. 49, no. 3, pp. 357 – 393, 1983.
- [99] P. L. Roe, “Characteristic-based schemes for the euler equations,” *Annual Review of Fluid Mechanics*, vol. 18, no. 1, pp. 337–365, 1986.
- [100] H. A. van der Vorst, “Bi-cgstab: A fast and smoothly converging variant of bi-cg for the solution of nonsymmetric linear systems,” *SIAM Journal on Scientific and Statistical Computing*, vol. 13, no. 2, pp. 631–644, 1992.
- [101] P. L. Roe, “Characteristic-based schemes for the euler equations,” *Annual Review of Fluid Mechanics*, vol. 18, no. 1, pp. 337–365, 1986.
- [102] F. peng Bai, Z. hua Yang, and W. gang Zhou, “Study of total variation diminishing (tvd) slope limiters in dam-breakflow simulation,” *Water Science and Engineering*, vol. 11, no. 1, pp. 68–74, 2018.
- [103] V. J. \* and A. M. , “Comparative study of flux-limiters based on must differencing scheme,” *International Journal of Computational Fluid Dynamics*, vol. 18, no. 7, pp. 569–576, 2004.
- [104] F. Moukalled, L. Mangani, and M. Darwish, *The Finite Volume Method in Computational Fluid Dynamics: An Advanced Introduction with OpenFOAM and Matlab*. Springer Publishing Company, Incorporated, 1st ed., 2015.
- [105] I. B. Celik, U. Ghia, P. J. Roache, C. J. Freitas, H. Coleman, and P. E. Raad, “Procedure for estimation and reporting of uncertainty due to discretization in cfd applications,” *Journal of Fluids Engineering*, vol. 130, 07 2008. 078001.
- [106] P. J. Roache, “Perspective: A method for uniform reporting of grid refinement studies,” *Journal of Fluid Engineering*, vol. 116, pp. 405–413, 1994.
- [107] I. Celik and O. Karatekin, “Numerical Experiments on Application of Richardson Extrapolation With Nonuniform Grids,” *Journal of Fluids Engineering*, vol. 119, no. 3, p. 584, 1997.
- [108] F. M. Sakri, M. S. Ali, and S. A. Salim, “Computational investigations and grid refinement study of 3D transient flow in a cylindrical tank using OpenFOAM,” *IOP Conference Series: Materials Science and Engineering*, vol. 152, no. 1, 2016.
- [109] L. Joly, J. Fontane, and P. Chassaing, “The Rayleigh-Taylor instability of two-dimensional high-density vortices,” *Journal of Fluid Mechanics*, vol. 537, pp. 415–431, 2005.

- [110] G. C. Burton, "Study of ultrahigh Atwood-number Rayleigh-Taylor mixing dynamics using the nonlinear large-eddy simulation method," *Physics of Fluids*, vol. 23, no. 4, p. 045106, 2011.
- [111] T. K. Sengupta, H. Singh, S. Bhaumik, and R. R. Chowdhury, "Diffusion in inhomogeneous flows : Unique equilibrium state in an internal flow," vol. 88, pp. 440–451, 2013.
- [112] C. W. Hamman, J. C. Klewicki, and R. M. Kirby, "On the lamb vector divergence in navierstokes flows," *Journal of Fluid Mechanics*, vol. 610, p. 261284, 2008.
- [113] S. Wang, G. He, and X. Zhang, "Lift enhancement on spanwise oscillating flat-plates in low-reynolds-number flows," *Physics of Fluids*, vol. 27, no. 6, p. 061901, 2015.
- [114] W. Sirignano and C. Mehring, "Review of theory of distortion and disintegration of liquid streams," *Progress in Energy and Combustion Science*, vol. 26, no. 4, pp. 609 – 655, 2000.
- [115] S. G. Chuech, "Spatial instability of a viscous liquid sheet," *International Journal for Numerical Methods in Fluids*, vol. 50, no. 12, pp. 1461–1474, 2006.
- [116] A. Khosronejad, L. Mendelson, A. H. Techet, S. . Kang, D. Angelidis, and F. Sotiropoulos, "Water exit dynamics of jumping archer fish: Integrating two-phase flow large-eddy simulation with experimental measurements," *Physics of Fluids*, vol. 32, no. 1, p. 011904, 2020.
- [117] J. Shinjo and A. Umemura, "Surface instability and primary atomization characteristics of straight liquid jet sprays," *International Journal of Multiphase Flow*, vol. 37, no. 10, pp. 1294–1304, 2011.
- [118] A. Zandian, W. A. Sirignano, and F. Hussain, "Understanding liquid-jet atomization cascades via vortex dynamics," *Journal of Fluid Mechanics*, vol. 843, pp. 293–354, 2018.
- [119] A. Zandian, W. A. Sirignano, and F. Hussain, "Planar liquid jet: Early deformation and atomization cascades," *Physics of Fluids*, vol. 29, no. 6, 2017.
- [120] C. Lee and X. Jiang, "Flow structures in transitional and turbulent boundary layers," *Physics of Fluids*, vol. 31, no. 11, p. 111301, 2019.
- [121] L. C. Lambourne and D. W. Bryer, "The bursting of leading-edge vortices-some observations and discussion of the phenomenon," *Aero. Res. Council R M no. 3282*, 1961.
- [122] H. Chen, D. L. Reuss, and V. Sick, "On the use and interpretation of proper orthogonal decomposition of in-cylinder engine flows," *Measurement Science and Technology*, vol. 23, no. 8, 2012.
- [123] L. Sirovich and M. Kirby, "Low-dimensional procedure for the characterization of human faces," *J. Opt. Soc. Am. A*, vol. 4, pp. 519–524, Mar 1987.
- [124] S. L. Brunton and J. N. Kutz, *Data-Driven Science and Engineering: Machine Learning, Dynamical Systems, and Control*. USA: Cambridge University Press, 1st ed., 2019.
- [125] D. Cavar and K. E. Meyer, "Les of turbulent jet in cross flow: Part 2 pod analysis and identification of coherent structures," *International Journal of Heat and Fluid Flow*, vol. 36, pp. 35 – 46, 2012.
- [126] G. Riches, R. Martinuzzi, and C. Morton, "Proper orthogonal decomposition analysis of a circular cylinder undergoing vortex-induced vibrations," *Physics of Fluids*, vol. 30, no. 10, p. 105103, 2018.
- [127] P. J. Schmid, "Dynamic mode decomposition of numerical and experimental data," *Journal of Fluid Mechanics*, vol. 656, p. 528, 2010.
- [128] K. K. Chen, J. H. Tu, and C. W. Rowley, "Variants of dynamic mode decomposition : connections between Koopman and Fourier analyses," *Journal of Nonlinear Science*, vol. 44, pp. 0–1, 2011.
- [129] F. Ostermann, R. Woszidlo, S. Gaertlein, C. Nayeri, and C. O. Paschereit, *Phase-Averaging Methods for a Naturally Oscillating Flow Field*.

- [130] J. C. R. Hunt, A. A. Wray, and P. Moin, “Eddies, streams, and convergence zones in turbulent flows,” *Center for Turbulence Research Report, CTR-S88*, pp. 193–208, Dec. 1988.
- [131] K. K. Nomura, H. Tsutsui, D. Mahoney, and J. W. Rottman, “Short-wavelength instability and decay of a vortex pair in a stratified fluid,” *Journal of Fluid Mechanics*, vol. 553, p. 283322, 2006.
- [132] S. C. CROW, “Stability theory for a pair of trailing vortices,” *AIAA Journal*, vol. 8, no. 12, pp. 2172–2179, 1970.
- [133] X. Wang and S. Alben, “The dynamics of vortex streets in channels,” *Physics of Fluids*, vol. 27, no. 7, p. 073603, 2015.